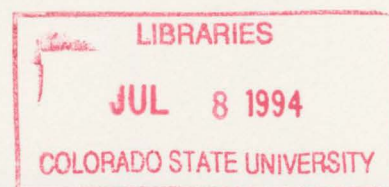


**WATER VAPOR AND TEMPERATURE
INVERSIONS NEAR THE 0°C LEVEL
OVER THE TROPICAL WESTERN PACIFIC**

by

Kenneth A. Hart



**Colorado
State
University**

**DEPARTMENT OF
ATMOSPHERIC SCIENCE**

PAPER NO. 555

**WATER VAPOR AND TEMPERATURE
INVERSIONS NEAR THE 0°C LEVEL
OVER THE TROPICAL WESTERN PACIFIC**

by

Kenneth A. Hart

Department of Atmospheric Science
Colorado State University
Fort Collins, CO 80523

Summer 1994

Atmospheric Science Paper No. 555



U18401 0275055

QC
852
Cl
no. 555
ATMOS

ABSTRACT

WATER VAPOR AND TEMPERATURE INVERSIONS NEAR THE 0°C LEVEL OVER THE TROPICAL WESTERN PACIFIC

During the Intensive Observation Period (IOP) [1 November 1992 - 28 February 1993] of the Tropical Ocean-Global Atmosphere Coupled-Ocean Atmosphere Response Experiment (TOGA COARE), several periods of water vapor and temperature inversions near the 0°C level were observed. Satellite and radiosonde data from TOGA COARE are used to document the large-scale conditions and thermodynamic and kinematic structures present during three extended periods in which moisture and temperature inversions near the freezing level were very pronounced. Observations from each case are synthesized into schematics which represent typical structures of the inversion phenomena. Frequency distributions of the inversion phenomena along with climatological humidity and temperature profiles are calculated for the four-month IOP.

Specific humidity or q inflections were observed simultaneously over large domains for extended periods of time (in excess of two days) in the midtroposphere. Local maxima in humidity were found to commonly occur near the freezing level or about 560 mb in the tropical region under study. The humidity inversions often occur in conjunction with temperature inversions (or stable layers), also at the 0°C level. The stable layer is usually positioned slightly above the moisture inversion. Two of the cases examined were observed during the active phase of the Madden-Julian Oscillation or MJO in which strong, low-level westerlies and upper-level easterlies were observed. IR satellite images of the TOGA COARE region reveal that the soundings which reflected moisture and temperature inversions at the freezing level ascended in generally clear and undisturbed conditions. During

the three cases under examination, deep convection was observed in latitudinally oriented bands which formed a "double-ITCZ" structure about the equator.

Frequency distributions of specific humidity inversions observed during the IOP reflect a maximum number of occurrences at altitudes just below the melting level. Distributions of stable temperature layers show a double-peak distribution - a low-level peak associated with tradewind-like or shallow cumulus clouds and a secondary peak corresponding to pressures near the 0°C level. The recurring moisture and temperature inversions near the freezing level were common enough to be evidenced in IOP averages. Climatological profiles of relative humidity averaged for the entire IOP reveal a nearly constant humidity average between 750 and 500 mb which contradicts the linear relation between relative humidity and pressure prescribed by Manabe and Wetherald (1967). The average relative humidity profiles resembled others reported in recent studies using data from the tropical western Pacific.

Several mechanisms for the formation of the inversions near the 0°C level are proposed. Temperature inversions may be the remnants of stratiform rain regions which are known to produce isothermal layers just below the melting level (Findeisen 1940). Another possibility is that the temperature inversions may be the result of melting-induced, positive potential vorticity (PV) anomalies. A third explanation involves the effects of gravity waves produced by tropical cloud systems. Moisture inversions may be caused by the preferential detrainment of water vapor from cumulus clouds near stable layers. Heavily-raining congestus clouds were frequently observed by COARE ship-based radars to top out near the freezing level which may have left higher concentrations of water vapor there.

ACKNOWLEDGEMENTS

I would like to express my deepest appreciation to my advisor, Professor Richard Johnson, for his guidance and unselfish dedication of time to this research effort. I would also like to thank my other committee members, Professor Roger Pielke and Professor Jack Cermak.

Many thanks go to Paul Ciesielski for his enduring patience and programming instruction. He was always willing to lend a helping hand. Thanks are also extended to Jim Bresch for his many helpful comments and programming expertise that provided the framework for several of the figures. Special thanks to Rick Taft for the tremendous job he did with the satellite images. The computer system assistance provided by Bill Gallus and Xin Lin is greatly appreciated. I would like to thank Jason Knievel for his tireless efforts in cleaning the Indonesian sounding data. Thanks go to Gail Cordova for her help in the completion of this manuscript.

Finally, I would like to thank my wife, Traci, for her support and numerous sacrifices over the past two years.

This research was supported by the National Oceanic and Atmospheric Administration under Grants NA90RAH00077 and NA37RJ0202. Salary and tuition were paid by the United States Air Force under the Air Force Institute of Technology Graduate Program.

TABLE OF CONTENTS

1	INTRODUCTION	1
2	BACKGROUND RESEARCH	3
2.1	Temperature Distributions	3
2.2	Humidity Distributions	4
2.3	Distributions of the "Apparent Moisture Sink" Q_2	11
3	DATA AND ANALYSIS PROCEDURES	13
3.1	Observational Network	13
3.2	Data	13
3.2.1	Sounding Systems	13
3.2.2	Satellite Data	16
3.3	Analysis Procedures	17
3.3.1	Corrections to Data	17
3.3.2	Derived Quantities	18
3.3.3	Objective Analysis Procedures	19
4	CASE STUDIES	20
4.1	Case I - 1800 UTC 16 December 1992 to 0600 UTC 20 December 1992	20
4.1.1	Satellite Overview	20
4.1.2	Thermodynamic and Kinematic Structure	23
4.2	Case II - 1200 UTC 29 December 1992 to 1200 UTC 1 January 1993	36
4.2.1	Satellite Overview	36
4.2.2	Thermodynamic and Kinematic Structure	39
4.3	Case III - 0000 UTC 2 February 1993 to 0000 UTC 5 February 1993	49
4.3.1	Satellite Overview	49
4.3.2	Thermodynamic and Kinematic Structure	49
4.4	Synthesis of Results and Interpretation	60
4.4.1	Typical Skew-T Profiles	60
4.4.2	Typical Specific Humidity Profiles	62
4.4.3	Synoptic Pattern Illustrations	62
5	SUMMARY STATISTICS	66
5.1	IOP Averages	66
5.2	Inversion Location Frequencies	68
5.3	Microphysical Processes	77

6 POSSIBLE CAUSES OF MOISTURE AND TEMPERATURE INVERSIONS NEAR THE 0°C LEVEL	82
6.1 Temperature Inversions	82
6.2 Moisture Inversions	89
7 SUMMARY AND CONCLUSIONS	92
REFERENCES	96

LIST OF FIGURES

2.1	Temperature inversions measured at Darwin research station during January and February of 1964 (from Haraguchi 1968)	5
2.2	Sounding taken at the Darwin research station at 1100 UTC 17 February 1964 (from Haraguchi 1968)	6
2.3	Schematic air parcel paths through two cloud populations (from Betts and Albrecht 1987)	7
2.4	Climatological humidity profiles measured at five stations using nine years of radiosonde measurements (from Liu et al. 1991)	9
2.5	Climatological humidity profiles for (a) Koror and (b) WP, a four station average, using 16 years of radiosonde data (from Gutzler 1993)	10
2.6	Normalized apparent moisture sink \hat{Q}_2 for West Pacific, East Atlantic, and Florida regions (from Johnson 1984)	12
3.1	Entire TOGA COARE domain (from TOGA COARE IOP Operations Summary 1993)	14
3.2	TOGA COARE outer sounding array (OSA) and intensive flux array (IFA) (from TOGA COARE IOP Operations Summary 1993)	15
4.1	GMS-IR satellite images of the TOGA COARE region at (a) 1745 UTC 16 December, (b) 0545 UTC 17 December, (c) 0645 UTC 18 December, and (d) 1745 UTC 18 December 1992	21
4.1	Continued.	22
4.2	Specific humidity time series for Nauru from 1200 UTC 16 December to 0600 UTC 20 December 1992	24
4.3	Equivalent potential temperature and saturation equivalent potential temperature profiles for Nauru at 0600 UTC 18 December	26
4.4	Same as in Fig. 4.2, except for Kapingamarangi	27
4.5	Same as in Fig. 4.2, except for Kavieng	28
4.6	Skew-T diagrams for Nauru at (a) 1200 UTC 16 December, (b) 1800 UTC 16 December, (c) 0000 UTC 18 December, and (d) 1200 UTC 18 December	29
4.7	Skew-T diagrams for Kwajalein at (a) 0000 UTC 16 December and (b) 1200 UTC 16 December and Majuro at (c) 0000 UTC 16 December and (d) 1200 UTC 16 December	31
4.8	East-west relative humidity cross-sections of LSA from 140°E to 180°E averaged from 10°S to 10°N at (a) 0000 UTC 16 December, (b) 0000 UTC 17 December, (c) 0000 UTC 18 December, and (d) 0000 UTC 19 December	33
4.9	Potential temperature time series for Nauru from 1200 UTC 16 December to 0600 UTC 20 December	34

4.10	North-south relative humidity cross-sections of LSA from 10°S to 10°N averaged from 150°E to 160°E at (a) 0000 UTC 17 December, (b) 0000 UTC 18 December, and (c) 0000 UTC 19 December.	35
4.11	GMS-IR satellite images of the TOGA COARE region at (a) 0645 UTC 29 December, (b) 1745 UTC 29 December, (c) 0545 UTC 30 December, and (d) 1745 UTC 30 December	37
4.11	Continued.	38
4.12	Specific humidity time series for Manus from 0000 UTC 29 December to 1800 UTC 1 January 1993	40
4.13	Same as in Fig. 4.12, except for Kavieng	41
4.14	Equivalent potential temperature and saturation equivalent potential temperature profiles for Kavieng at 1200 UTC 30 December	42
4.15	Skew-T diagrams for Kavieng at (a) 0600 UTC 29 December, (b) 1200 UTC 29 December, (c) 0600 UTC 30 December, (d) 1200 UTC 30 December, (e) 1800 UTC 30 December, (f) 0000 UTC 31 December, (g) 1200 UTC 31 December, and (h) 0600 UTC 1 January.	44
4.15	Continued.	45
4.16	East-west relative humidity cross-sections of LSA from 140°E to 180°E averaged from 10°S to 10°N at (a) 0000 UTC 28 December, (b) 0000 UTC 29 December, (c) 0000 UTC 30 December, and (d) 0000 UTC 31 December	47
4.17	North-south relative humidity cross-sections of LSA from 10°S to 10°N averaged from 140°E to 160°E at (a) 0000 UTC 29 December, (b) 0000 UTC 30 December, (c) 0000 UTC 31 December, and (d) 0000 UTC 1 January	48
4.18	GMS-IR satellite images of the TOGA COARE region at (a) 1745 UTC 1 February, (b) 1745 UTC 2 February, (c) 1745 UTC 3 February, and (d) 1745 UTC 4 February 1993	50
4.18	Continued.	51
4.19	Specific humidity time series for Nauru from 1200 UTC 1 February to 0600 UTC 5 February 1993	52
4.20	Same as in Fig. 4.19, except for Kapingamarangi	54
4.21	East-west zonal wind cross-sections of LSA from 140°E to 180°E averaged from 10°S to 10°N at (a) 0000 UTC 2 February, (b) 0000 UTC 3 February, (c) 0000 UTC 4 February, and (d) 0000 UTC 5 February	55
4.22	East-west relative humidity cross-sections of LSA from 140°E to 180°E averaged from 10°S to 10°N at (a) 0000 UTC 1 February, (b) 0000 UTC 2 February, (c) 0000 UTC 3 February, and (d) 0000 UTC 4 February	56
4.23	Skew-T diagrams for Nauru at (a) 1200 UTC 1 February, (b) 0000 UTC 2 February, (c) 0000 UTC 3 February, and (d) 0000 UTC 4 February.	57
4.24	North-south relative humidity cross-sections of LSA from 10°S to 10°N averaged from 150°E to 170°E at (a) 0000 UTC 2 February, (b) 0000 UTC 3 February, (c) 0000 UTC 4 February, and (d) 0000 UTC 5 February	59
4.25	Typical Skew-T profiles for Case I, Case II, and Case III	61
4.26	Typical specific humidity profiles for Case I, Case II, and Case III	63
4.27	Synoptic pattern illustrations for (a) Case I, (b) Case II, and (c) Case III	64
5.1	Mean relative humidity profiles for four-month IOP at (a) Manus, (b) Kavieng, (c) Kapingamarangi, and (d) Nauru	67

5.2	Mean $d\theta/dp$ profiles for four-month IOP at (a) Manus, (b) Kavieng, (c) Kapingamarangi, and (d) Nauru	69
5.3	Stable layer locations during IOP at (a) Manus, (b) Kavieng, (c) Kapingamarangi, and (d) Nauru	71
5.4	Stable layer locations ($\leq 4^\circ\text{K km}^{-1}$) at Nauru as a function of layer depth . . .	72
5.5	Stable layer locations at Nauru as a function of lapse rate	74
5.6	Specific humidity inversion locations during IOP at (a) Manus, (b) Kavieng, (c) Kapingamarangi, and (d) Nauru	75
5.7	Specific humidity inversion locations at Nauru as a function of inversion depth	76
5.8	Schematic showing modification of a mixing line by microphysical processes (modified from Betts and Albrecht 1987)	77
5.9	θ vs. q for Nauru at 1800 UTC 18 December	78
5.10	θ vs. q at Kavieng for month of December	80
5.11	Illustration of the Hadley Cell using microphysical processes (R. Boers, personal communication)	81
6.1	PV-induced anomaly mechanism for temperature inversions	83
6.2	Buoyancy bore mechanism for temperature inversions (from Mapes 1993) . . .	85
6.3	Specific humidity deviations from the IOP mean at Kapingamarangi from 15 December to 26 December	86
6.4	Temperature deviations from the IOP mean at Kapingamarangi from 15 December to 26 December	87
6.5	Temperature inversion formed by melting in stratiform region	88
6.6	Numerical simulation of a cumulus cloud detraining near a stable layer (from Bretherton and Smolarkiewicz 1989)	90
6.7	Heavily raining congestus cloud detraining moisture near the freezing level . . .	91

Chapter 1

INTRODUCTION

As the most dominant greenhouse gas, water vapor and its distribution in the troposphere are crucial elements of the climate system. Infrared absorption in the atmosphere occurs primarily as a result of the presence of water vapor and cloud droplets. The radiative balance of the earth-atmosphere system relies on deep convection to cool the earth's surface. Since the distribution of water vapor is highly stratified in the earth's atmosphere, most of the water mass lies in the lower troposphere. Lindzen (1990) argues that the greenhouse effect is relatively ineffective due to the roles of deep convection and large-scale meridional transport which redistribute heat and moisture to higher altitudes and latitudes, respectively. For this reason, Lindzen et al. (1982) describes the greenhouse absorption role of water vapor and cloud droplets above 5 km as important for containing the heat carried away from the earth's surface.

An accurate description of specific and relative humidity profiles over the tropical regions suffers from a lack of adequate data, particularly in the mid- and upper-troposphere. The future performance of climate models hinges on our ability to accurately specify a climatological humidity profile. Manabe and Wetherald (1967) prescribed a linear relation between relative humidity and pressure given by

$$\frac{U}{U_o} = \frac{\left(\frac{p}{p_o} - .02\right)}{.98}, \quad (1.1)$$

where U refers to relative humidity, p to pressure, and subscript o to surface values. This profile yields a monotonic decrease in U with height. However, several recent studies (Liu et al. 1991, Gutzler 1993) have revealed a mid-tropospheric (near 600 mb) inflection point, or "kink" in humidity profiles. This feature is also present in the climatological data of

Oort (1983). These seemingly minor perturbations in the mean relative humidity profiles have not received much attention; however, their widespread occurrence and persistence suggest they are deserving of more detailed documentation and explanation.

Nearly a decade ago, the international community launched the Tropical Ocean-Global Atmosphere (TOGA) Program, a major component of the World Climate Research Programme. Under the direction of the TOGA Program, the TOGA Coupled Ocean-Atmosphere Response Experiment (TOGA COARE) was organized to better describe and understand atmospheric and oceanographic processes in the western Pacific warm-pool region. The primary objective of TOGA COARE is to improve air-sea exchange and boundary-layer parameterizations in oceanic and atmospheric models, and to validate coupled models (Webster and Lukas 1992). TOGA COARE was carried out in several field phases during 1992 and 1993, including the atmospheric Enhanced Monitoring Period (1 July 1992 - 30 June 1993) and the Intensive Observation Period or IOP (1 November 1992 - 28 February 1993).

High-resolution radiosonde data from the TOGA COARE IOP are examined in this study to document the vertical distribution of temperature and water vapor over the Pacific "warm pool". The analyses reveal further evidence of a recurring water vapor profile inflection point in the midtroposphere in regions outside convective systems. A temperature inversion or stable layer often occurs simultaneously with the humidity inflection. Three extended periods with prominent temperature and moisture inversions during the IOP are explored.

The objectives of this study are the following:

- Documentation of the structure, evolution, and large-scale conditions associated with the temperature and moisture inversions during each of the three IOP cases
- Synthesis of the results for the three cases into average or typical structures of the inversion phenomena
- Determination of frequency distributions of the inversion phenomena

Lastly, possible causes for both the temperature and moisture inversions will be discussed.

Chapter 2

BACKGROUND RESEARCH

While a number of studies have examined vertical distributions of temperature and moisture in the tropics, mid-tropospheric temperature and moisture inversions have only been discussed sparingly (Haraguchi 1968; Liu et al. 1991; Gutzler 1993). Most attention on inversions has focused on those present in the convective boundary layer (CBL). Specific humidity reversals have been observed in and just above the CBL over the tropical Pacific (Betts and Albrecht 1987; Kloesel and Albrecht 1989). However, as this study will show, there are also inversions above the CBL (near the melting level) that appear to be prevalent throughout the tropics.

2.1 Temperature Distributions

Recurring temperature inversions or stable layers have been revealed in several atmospheric studies over the tropical oceans. Almost all of these inversions were attributed to the tradewind regime. Riehl et al. (1951) and Neiburger et al. (1961) analyzed temperature inversions in the CBL over the northeastern Pacific. Dropwindsondes launched over the tropical Pacific Ocean during the First GARP Global Experiment (FGGE) were used to study boundary layer features over the equatorial Pacific (Firestone and Albrecht 1986; Betts and Albrecht 1987; Kloesel and Albrecht 1989). Experiments to study boundary layer structure over the Atlantic Ocean have included the Atlantic Tradewind Experiment (ATEX) (Augstein et al. 1973), the Barbados Oceanographic and Meteorological Experiment (BOMEX) (Holland and Rasmusson 1973), and GARP Atlantic Tropical Experiment (GATE) (Augstein 1978).

Haraguchi (1968) found two distinct regimes of temperature inversions over the tropical eastern Pacific Ocean during the winter of 1964. The inversions were found in two

basic layers as shown in Fig. 2.1 – the lower one between 900 and 725 mb and the upper between 600 and 400 mb. Figure 2.1 represents a 21-day period of radiosonde data taken at the Darwin research station at Academy Bay, Santa Cruz, Galapagos Islands (0.75°S , 90.3°W). The inversion tops and bottoms are indicated by dots. Similar inversions were observed at other locations during cruises of the same experiment. The lower inversion is associated with the tradewind cumulus layer (e.g. Riehl 1979) and has been studied extensively. The upper inversion has received much less attention and is the subject of this paper.

A plot of the sounding taken at the Darwin research station (Fig. 2.2) depicts the persistent lower and upper inversions located near 875 mb and the freezing level, respectively. Other minor stable layers were present, but they were not as persistent. Relative humidity values are placed along the sounding curve. A local maximum of relative humidity is found at the base of the inversion near 0°C .

The lower inversion had been noted previously in studies of tropical regions, but the upper inversion regime had not and, today, remains less understood. In his study of tropical eastern Pacific data, Haraguchi (1968) found the upper inversion, with a mean height of 550 mb, to be as continuous and persistent as the lower inversion. Haraguchi (1968) suggested the upper inversion may have been caused by anticyclonic circulation associated with a semi-permanent High in the vicinity of Central America during winter.

2.2 Humidity Distributions

Betts and Albrecht (1987) documented a reversal in specific humidity, termed “ q reversal”, in their study of the central Pacific tradewind regime. These features were found in and just above the CBL. They attributed the reversal in the CBL to the evaporation of falling precipitation. Figure 2.3, taken from Betts and Albrecht (1987), shows two populations of clouds in the CBL which may act to produce a local maximum in q within the tradewind cumulus layer. They hypothesized that the downward circulation is split into two separate branches if the cloud towers that penetrate the tradewind inversion precipitate. The precipitation fallout from the deeper clouds mixes, but cools less and sinks only

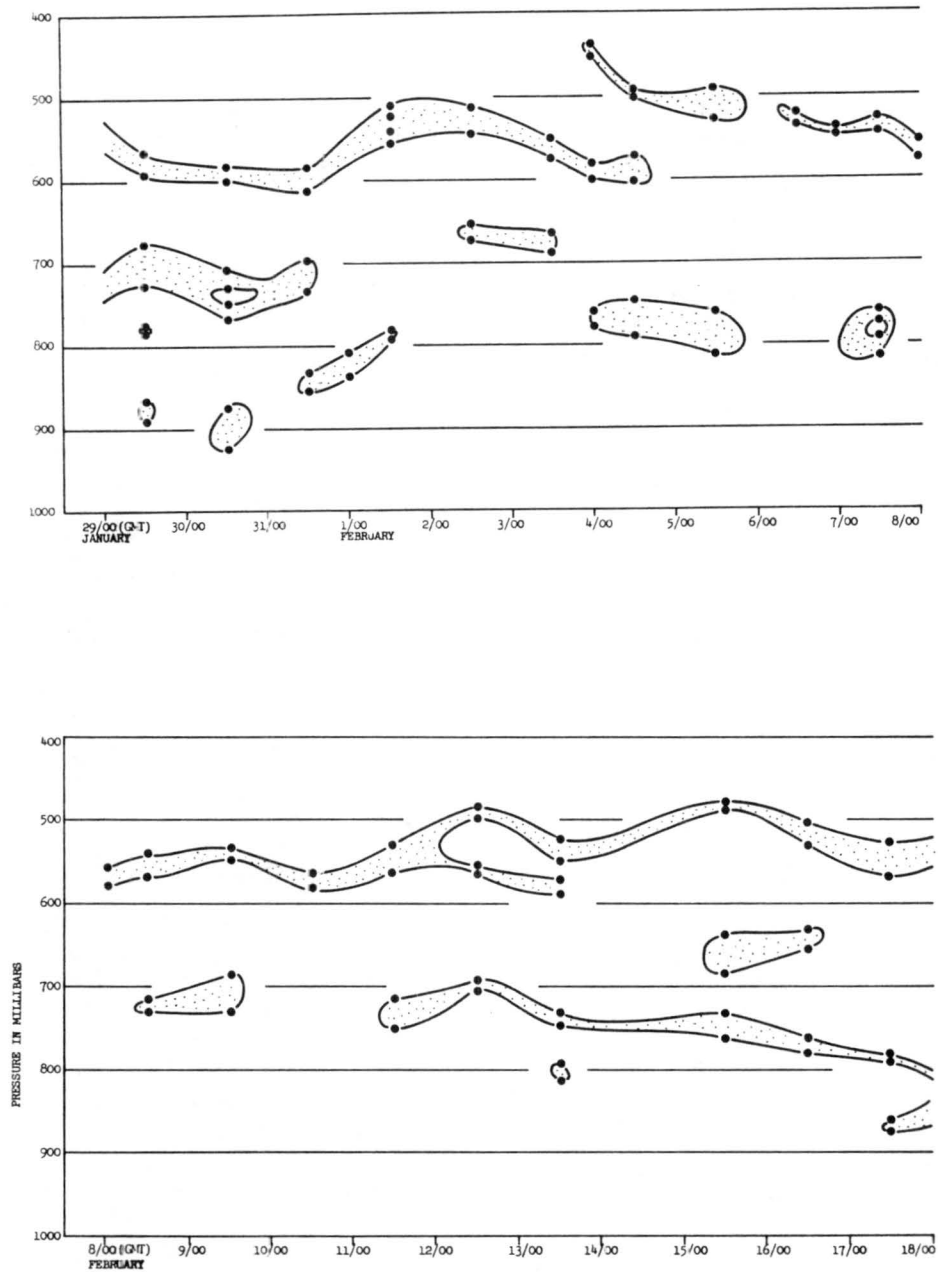


Figure 2.1: Temperature inversion locations measured at Darwin research station during 21-day period of January and February of 1964. Dots represent top and bottom of inversions (taken from Haraguchi 1968).

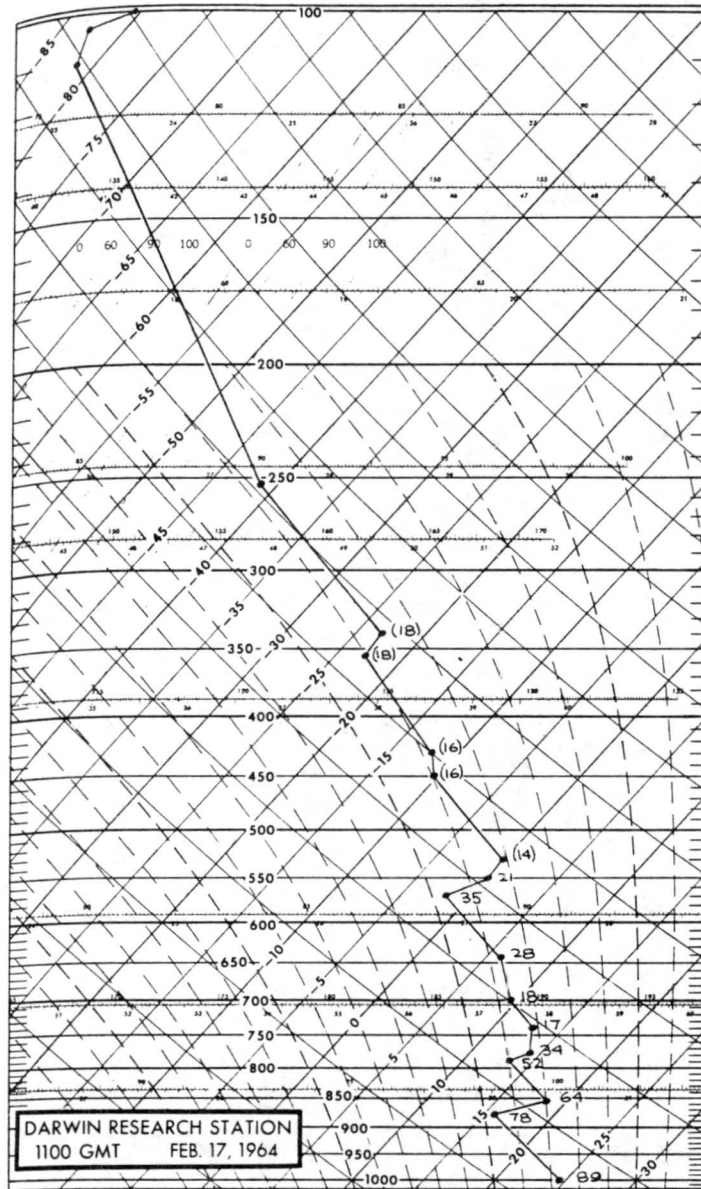


Figure 2.2: Sounding taken at the Darwin research station at 1100 UTC 17 February 1964 (taken from Haraguchi 1968). Relative humidity values are indicated along the temperature profile.

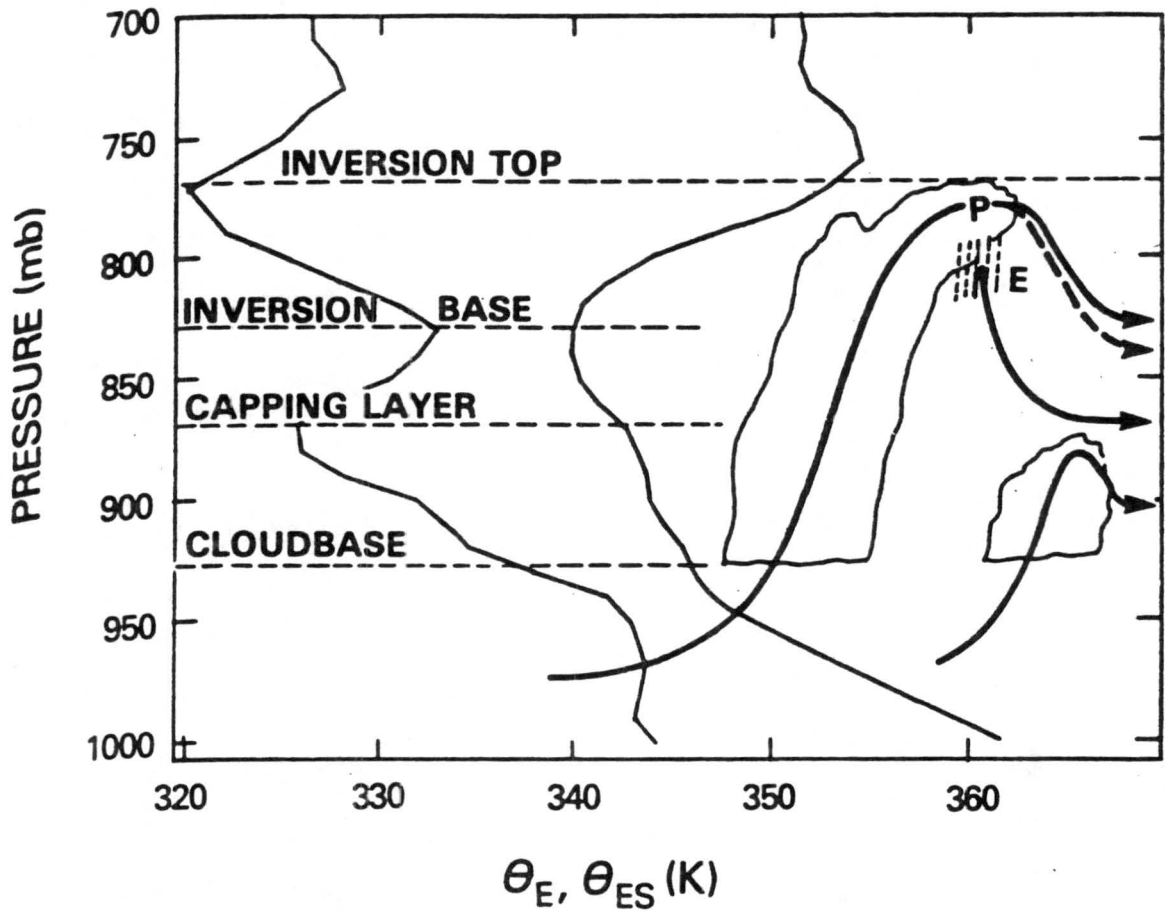


Figure 2.3: Schematic air parcel paths through two cloud populations showing origin of moist layer at the base of the inversion (830 mb) and dry layer (870 mb) capping a smaller cloud population (taken from Betts and Albrecht 1987). θ_e and θ_{es} average profiles are shown at left.

to near the inversion base, leaving cool, moist air (high θ_e and low θ_{es}) at this level. The evaporation of precipitation into the very dry inversion layer, however, cools and produces a dry penetrative downdraft capable of reaching levels well below the inversion base. The latter process may produce the dry capping layer near 870 mb. Betts and Albrecht (1987) suggested that the commonly observed feature above the CBL may be of similar origin as nearby convection penetrates to levels above the inversion, moistens the layer through detrainment, and forms downdrafts that spread out at the top of the inversion. The analyses of Kloesel and Albrecht (1989) support this hypothesis. Kloesel (1993) also describes q laminae above the CBL top during the First ISCCP Regional Experiment (FIRE). These moist layers are presumed to have a midlatitude source, however.

Liu et al. (1991) evaluated nine years of radiosonde observations from 1980 to 1988 at five Pacific island stations. The stations extended from the Arctic to the tropical South Pacific and included St. Paul (57.2°N, 189.8°E), Midway (28.2°N, 182.6°E), Wake (19.3°N, 166.7°E), Majuro (7.1°N, 171.4°E), and Pago Pago (14.3°S, 189.3°E). The climatological profiles of mean relative humidity and standard deviations for these five stations, taken from Liu et al. (1991), are shown in Fig 2.4. The 9-year means at all of the stations depict a maximum just below 900 mb which contradicts the linear relationship between relative humidity and pressure described by (1.1). This feature is a result of boundary layer mixing. At the two tropical stations, Majuro (7.1°N) and Pago Pago (14.3°S), inflections in the relative humidity profiles are visible in the midtroposphere (near 600 mb). The most pronounced mid-tropospheric inflection was apparent at Majuro. Liu et al. (1991) suggested that the higher relative humidity measured in the mid- and upper-troposphere at Majuro, located in the western tropical Pacific, was due to deep convection. Unlike the other higher latitude stations, the variance of relative humidity reached a maximum in the midtroposphere at both Majuro and Pago Pago.

Gutzler (1993) analyzed sounding data taken over a 16-year period (1973-1988) at Koror (7.3°N, 134.5°E), Truk (7.4°N, 151.8°E), Pohnpei (6.9°N, 158.3°E), and Majuro. He computed the climatological humidity profiles for Koror and a four-station average using the above stations, denoted WP (Fig. 2.5). The profiles for both reflected a maximum of

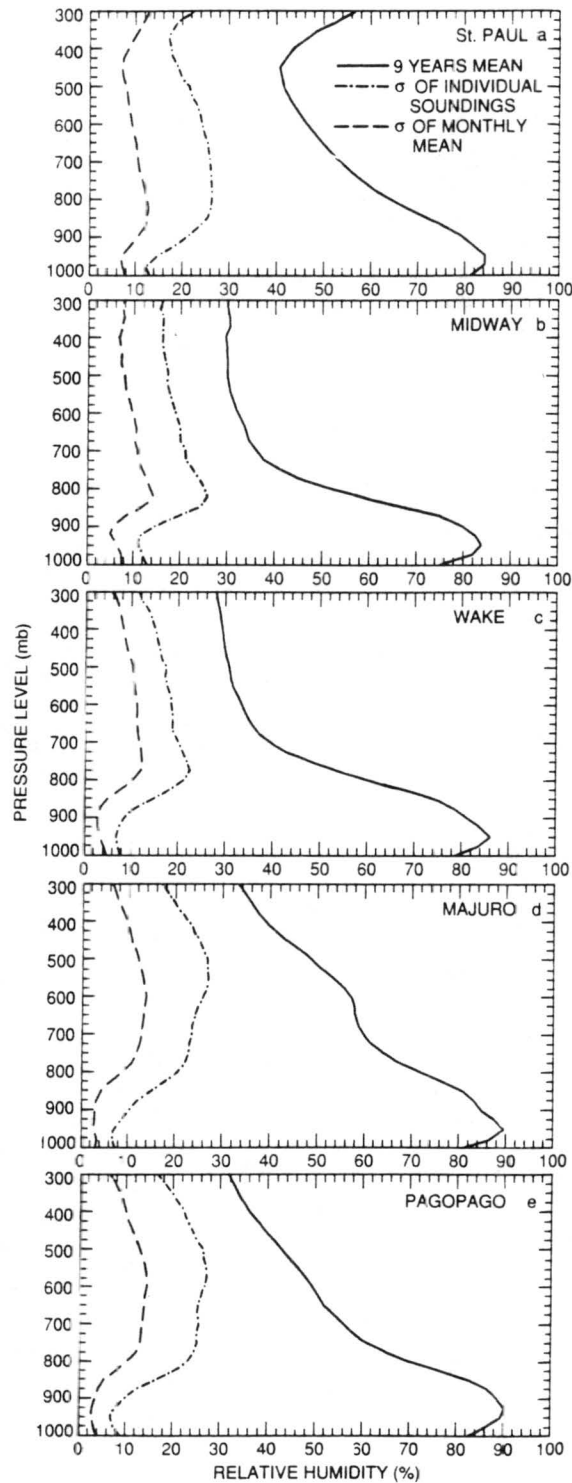


Figure 2.4: Profiles of mean relative humidity, standard deviation of individual measurements, and standard deviation of the monthly mean for nine years of radiosonde measurements at five stations (taken from Liu et al. 1991).

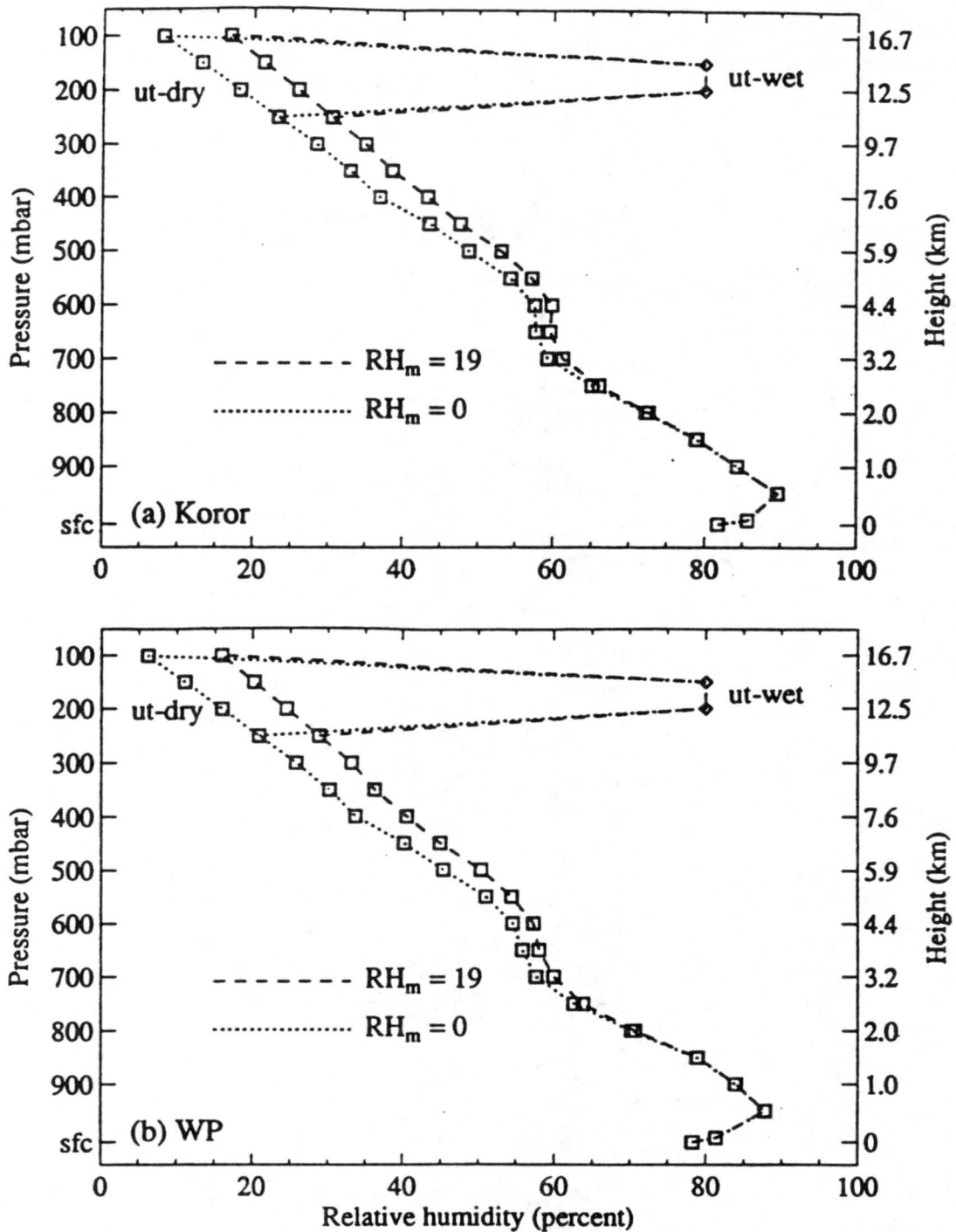


Figure 2.5: Climatological humidity profiles for (a) Koror and (b) WP, a four station average, using 16 years of radiosonde data (taken from Gutzler 1993). Missing relative humidity values have been replaced by either 0 or 19%. “Ut-wet” profiles prescribe 80% RH at the 200 and 150-mb levels to simulate water vapor associated with cirrus.

relative humidity near 950 mb, a linear decrease of relative humidity between 950 and 750 mb and above 600 mb, but a roughly constant layer of relative humidity between 700 and 600 mb. These results concur with those found by Liu et al. (1991) at Majuro.

2.3 Distributions of the “Apparent Moisture Sink” Q_2

This study will describe recurring perturbations found in the specific humidity fields near the melting level during the TOGA COARE IOP. Although not present at all times, these mid-tropospheric q perturbations are common enough to be evidenced in distributions of the “apparent moisture sink” Q_2 (Yanai et al. 1973). Here, Q_2 is defined by

$$Q_2 = -L \left(\frac{\partial \bar{q}}{\partial t} + \bar{\mathbf{v}} \cdot \nabla \bar{q} + \bar{\omega} \frac{\partial \bar{q}}{\partial p} \right), \quad (2.1)$$

where an overbar refers to a horizontal average and L is the latent heat of vaporization.

Results from moisture budget studies of convective systems over tropical and many summertime midlatitude locations show a double-peak structure to Q_2 . Johnson (1984) computed the “normalized apparent moisture sink” \hat{Q}_2 , defined as Q_2/P_0 (P_0 = surface precipitation), for four studies (Fig. 2.6). Except for the Thompson et al. (1979) study, each \hat{Q}_2 profile depicts a distinct double-peak structure with a minimum near the melting level. In the tropical western Pacific, ω typically has a single peak (Reed and Recker 1971; Yanai et al. 1973). Since the last term of 2.1 is typically the most dominant, the double peak in Q_2 can be explained by an inflection in the q profile.

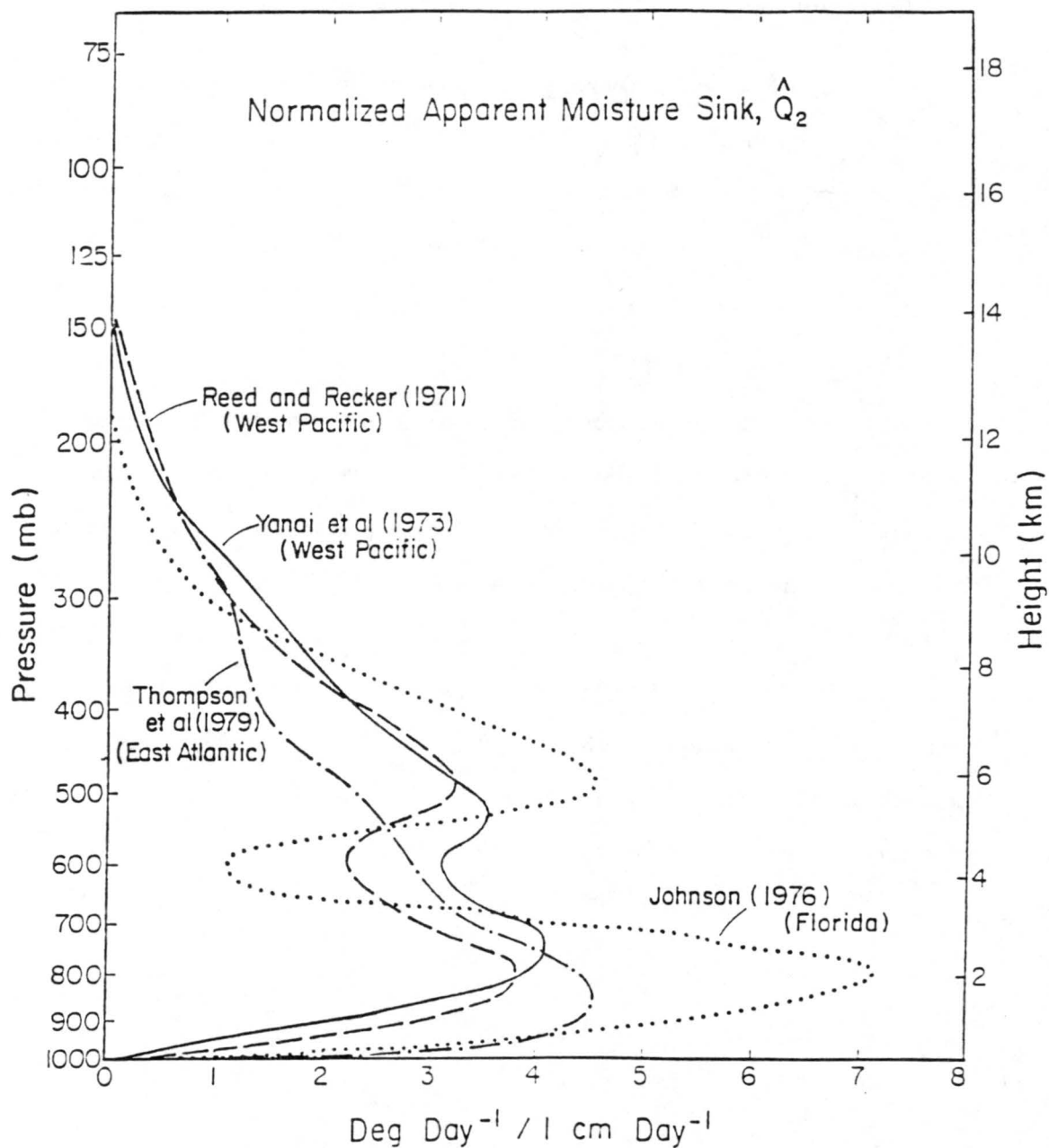


Figure 2.6: Normalized apparent moisture sink \hat{Q}_2 for West Pacific, East Atlantic, and Florida regions (taken from Johnson 1984).

Chapter 3

DATA AND ANALYSIS PROCEDURES

3.1 Observational Network

The TOGA COARE observational network (Fig. 3.1) was organized into three principal domains to study air-sea exchange processes in the western Pacific warm-pool region (Webster and Lukas 1992). The Large-scale Sounding Array (LSA) is defined by the region from 10°N to 10°S and 140°E to the date line. Inside the LSA, the Outer Sounding Array (OSA) is bounded by the meteorological sounding stations at Chuuk, Pohnpei (Ponape), Nauru, Honiara, Misima, and Manus Island. Embedded within the OSA is the Intensive Flux Array (IFA), centered at 2°S , 156°E . The IFA is bounded by the island stations at Kapingamarangi and Kavieng, and two People's Republic of China (PRC) research ships, the Kexue 1 and the Shiyan 3.

The TOGA COARE sounding array included rawinsonde locations from the World Weather Watch (WWW) network along with a network of NCAR/NOAA Integrated Sounding Systems (ISS) shown by the closed (land-based) and open (ship) circles in Fig. 3.2. ISS systems were deployed at six locations including the four stations forming the boundary of the IFA. ISS units were also deployed to Nauru and Manus on the OSA. The upper-air stations within the LSA launched two sondes per day while the stations inside or on the OSA boundary launched sondes four times per day.

3.2 Data

3.2.1 Sounding Systems

The ISS stations included a 915-MHz wind profiler; an Omega-sonde system; a radio acoustic sounding system (RASS), which is used to calculate boundary layer wind profiles

COARE Priority Sounding Stations

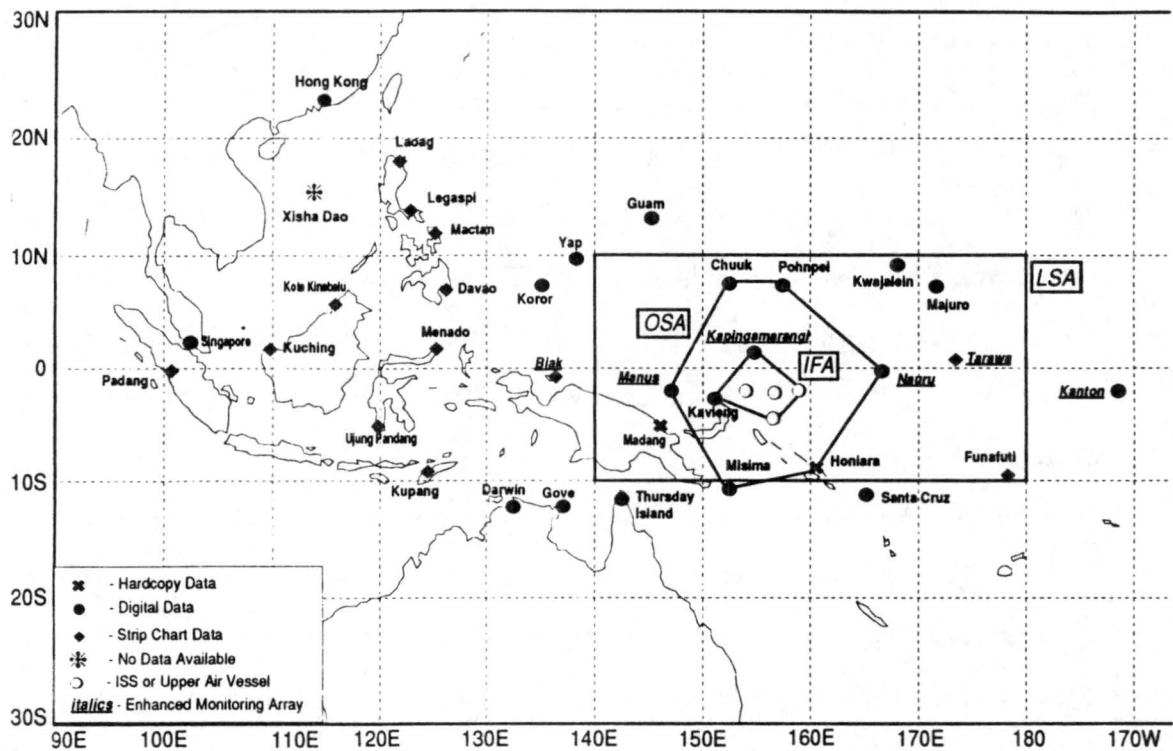


Figure 3.1: Western Pacific Ocean region showing the entire TOGA COARE domain. The large-scale array (LSA), outer-sounding array (OSA), and intensive flux array (IFA) are outlined (taken from TOGA COARE IOP Operations Summary 1993).

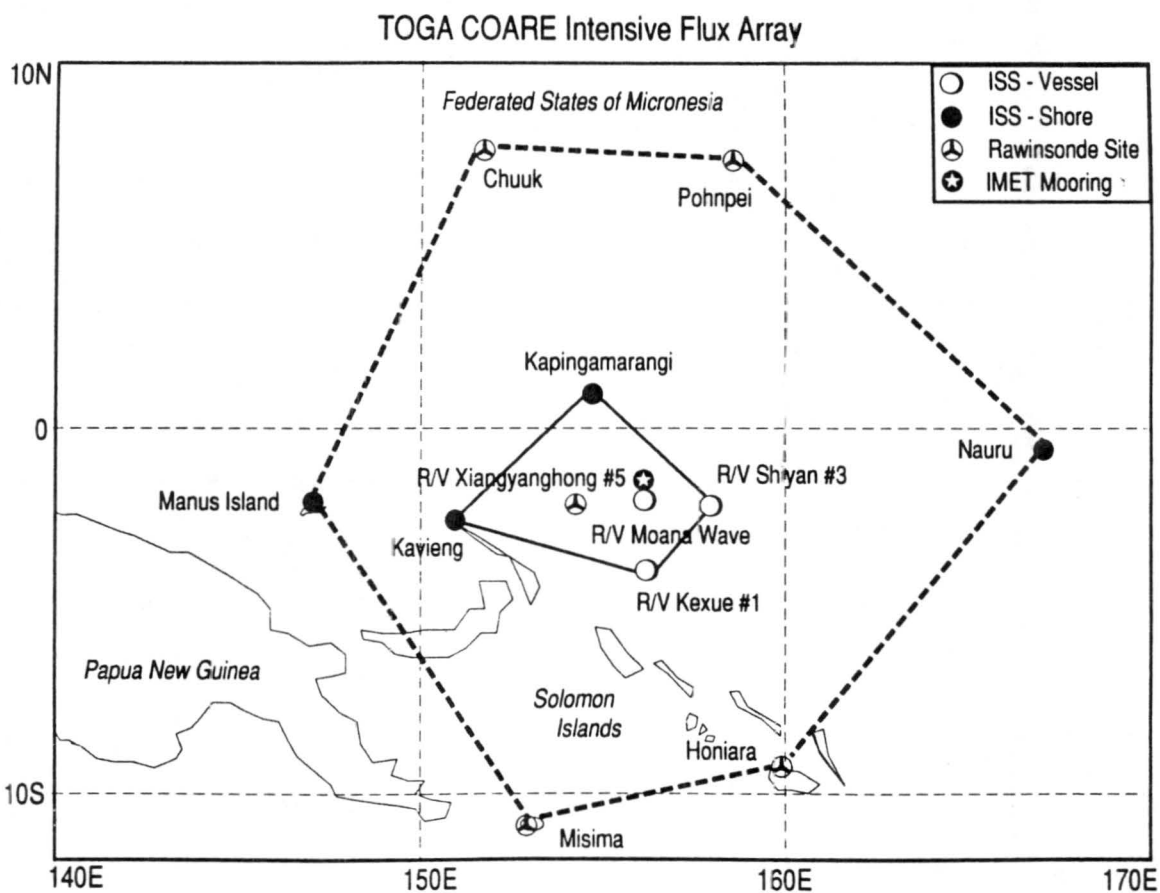


Figure 3.2: TOGA COARE outer sounding array (OSA) and intensive flux array (IFA) (taken from TOGA COARE IOP Operations Summary 1993).

through virtual temperature measurements; and an enhanced surface observing system. The surface observing system was a version of the Portable Automated Mesonet (PAM) concept (Brock et al. 1986) and included sensors for wind, temperature, pressure, humidity, precipitation, and several radiometers (Parsons et al. 1994). The Omega-sonde system for COARE included the Vaisala RS80 Radiosonde.

A new, improved humidity sensor, the Vaisala HUMICAP sensor, was used on the RS80 Radiosonde and many other sounding systems in the COARE LSA. It was hoped that this new sensor would provide much needed information about upper-tropospheric water vapor distributions since manufacturer's specifications indicated a sensor accuracy of $\pm 2\%$ down to -70°C . However, when used in the field, it was quickly discovered that the sensor often "iced up" at temperatures $\leq -40^{\circ}\text{C}$. Therefore, reliable humidity measurements in the upper troposphere could unfortunately not be obtained. Nevertheless, reliable measurements *were* obtained in the mid- to lower-troposphere, the region of interest for this study. Since the moisture inversions investigated here are in the vicinity of the 0°C level, there was some initial concern that they might be an artifact of the sensor calibration around 0°C . However, it was determined that the sensor was calibrated with respect to liquid water at all temperatures, as assumed in all humidity algorithms, so that observed moisture inversions near the 0°C level, when they exist, are real.

3.2.2 Satellite Data

Infrared (IR) satellite data used were collected by the Japanese Geostationary Meteorological Satellite - 4 (GMS-4), positioned over 140°E . The satellite provided 5-km footprints in the IR window every hour. The satellite data were digitized and distributed on laser disk by the School of Ocean and Earth Science and Technology at the University of Hawaii. Each satellite image shown in the study covers an area from 135°E to 175°E and from 10°S to 10°N , closely resembling the area bounded by the LSA. The IFA and OSA are shown on each satellite image as the inner and outer polygons, respectively.

3.3 Analysis Procedures

At the ISS stations, pressure, temperature, and relative humidity measurements were transmitted from the sonde roughly every 1.5 seconds during ascent. Mandatory and significant level data (WMO 1987) were transmitted near real time over the global telecommunications system (GTS). The GTS data at 0000 UTC have been edited by the CSU staff to remove erroneous points. The NCAR Surface and Sounding Systems Facility (SSSF) has distributed the raw sounding data, the 10-s data and the 5-mb interpolated data for the NCAR/NOAA ISS stations at Manus, Kavieng, Kapingamarangi, and Nauru. The raw data file contains roughly one sample every 1.5 seconds (Miller 1993). The 10-s data points were generated by the SSSF by smoothing the raw thermodynamic data over a pre-defined smoothing interval using a least squares technique (Miller 1993). An interpolation was then applied between the 10-s data points which resulted in constant pressure increments of 5 mb. The interpolated data were subjected to an automated quality control. GTS data are used in the gridded analyses, but processed ISS 5 mb data are used elsewhere.

3.3.1 Corrections to Data

Corrections, proposed and developed by Cole (1993) were made to the low-level data points of the 5-mb interpolated data to account for two errors connected with measurements in COARE - solar heating of the radiosonde sensors and response time of the humidity sensor. The error due to heating of the sensor arm prior to launch affected all of the ISS sites during sunny, daytime launches. The temperature sensor was mounted on a small, isolated piece of the sensor arm which quickly attained thermal equilibrium, yielding temperature errors for the first 10 s of flight (Miller 1993). The piece on which the humidity sensor was mounted was much larger, producing a larger thermal time constant. Since the humidity sensor measured relative humidity with respect to the sensor surface and temperature of the sensor in these cases was higher than the ambient temperature, the relative humidity was erroneously lower. Consequently, humidity measurements were affected for roughly the first 40 s of flight (Miller 1993).

At Kapingamarangi and Nauru, launches were made from air-conditioned environments which left initial humidity measurements too dry. Comparisons with the surface sensor concluded that the air-conditioning did not significantly affect the initial temperature measurements due to poor insulation in the launcher walls. Also, the humidity response time has been found to be slower than the 1-s specified by the manufacturer. Laboratory tests done at NCAR have determined the humidity sensor time constant to be closer to 7 s. The difference has been attributed to the protective cap that covers the RH sensor. The lower humidity caused by the air-conditioners could be seen for up to 30 s or more after launch (Miller 1993). At this time, corrections have only been applied to the 5 mb data at Nauru and Kavieng. Corrections to the remaining ISS sites should be complete by Summer 1994.

3.3.2 Derived Quantities

Derived quantities of altitude, dewpoint temperature T_d , specific humidity q , potential temperature θ , equivalent potential temperature θ_e , and saturation equivalent potential temperature θ_{es} were computed from the observed pressure, temperature, relative humidity, and time in seconds. The altitude and dewpoint temperatures were computed at NCAR/SSSF before the data were released.

The specific humidity q , defined as the mass of water vapor per mass of moist air, was derived by first computing the vapor pressure e from

$$e(T_d) = 6.112 \times \exp\left(\frac{17.67(T_d - 273.15)}{T_d - 29.65}\right), \quad (3.1)$$

where $e = Ue_s(T)/100$. The vapor pressure function is the Bolton (1980) approximation of the formula given by Wexler (1976). The relative humidity U is given as a percentage and T_d is in Kelvin. Using (3.1), the specific humidity was then computed from

$$q = \frac{\epsilon e}{p - .378e}, \quad (3.2)$$

where $\epsilon = 0.622$ is the ratio of the molecular weight of water vapor to the molecular weight of dry air.

The potential temperature, equivalent potential temperature and saturation equivalent potential temperature were then computed from

$$\theta = T \left(\frac{p_0}{p} \right)^\kappa, \quad (3.3)$$

$$\theta_e = \theta \exp \left(\frac{2.67w}{T_s} \right), \quad (3.4)$$

and

$$\theta_{es} = \theta \exp \left(\frac{2.67w_s}{T} \right), \quad (3.5)$$

where the water vapor mixing ratio w , saturation water vapor mixing ratio w_s , and saturation level temperature T_s are given by

$$w = \frac{\epsilon e}{p - e}, \quad (3.6)$$

$$w_s = \frac{\epsilon e_s}{p - e_s}, \quad (3.7)$$

and

$$T_s = \frac{1}{\frac{1}{T-55} - \frac{\ln(U/100)}{2840}} + 55. \quad (3.8)$$

The constants in equations (3.4) and (3.5) were suggested by Betts (1982). The constants used to compute T_s in (3.8) are found in Bolton (1980).

3.3.3 Objective Analysis Procedures

North-south and east-west cross-sections of the LSA were constructed from interpolated GTS message sounding data. The sounding data were interpolated onto a 78 km by 78 km grid for the LSA using a Barnes objective analysis scheme (Barnes 1973). The vertical grid increment was 25 mb. The scheme employed a variable radius of influence that depended on the average station separation using the five nearest stations. A two-pass filter was used and analyses were completed from 1000 mb to 400 mb for relative humidity and zonal wind speed.

Chapter 4

CASE STUDIES

During the TOGA COARE IOP, moisture and temperature inversions (or stable layers) were observed near the melting level for periods of several days. The moisture inversions were sufficiently common that they were evident in IOP averages (to be shown in Chapter 5), consistent with the findings of Liu et al. (1991) and Gutzler (1993). However, in this chapter several cases will be studied. The most prominent examples occurred on 16 - 20 December 1992, 29 December 1992 - 1 January 1993, and 2 - 5 February 1993. Each of these cases shared several common characteristics ranging from the synoptic-scale cloud features to thermodynamic and kinematic structure.

The purpose of this chapter is to provide a detailed analysis of each of the three cases. All three cases contained prominent and sustained reversals in the specific humidity field and stable temperature layers near the freezing level. The chapter will conclude with a synthesis of the observations in each case.

4.1 Case I - 1800 UTC 16 December 1992 to 0600 UTC 20 December 1992

4.1.1 Satellite Overview

The satellite sequence (Figs. 4.1a-d) shows the evolution of the convective features over the LSA from 16 to 18 December 1992. During this period, the convection evolved from a rather disorganized state to two bands near 5°N and 5°S, although the bands were never steady. Most of the ISS sites were in relatively undisturbed conditions between the two bands.

At 1745 UTC 16 December (Fig. 4.1a), an organized area of convection was associated with the Southern Hemisphere convergence zone, between 2°S and 8°S east of the

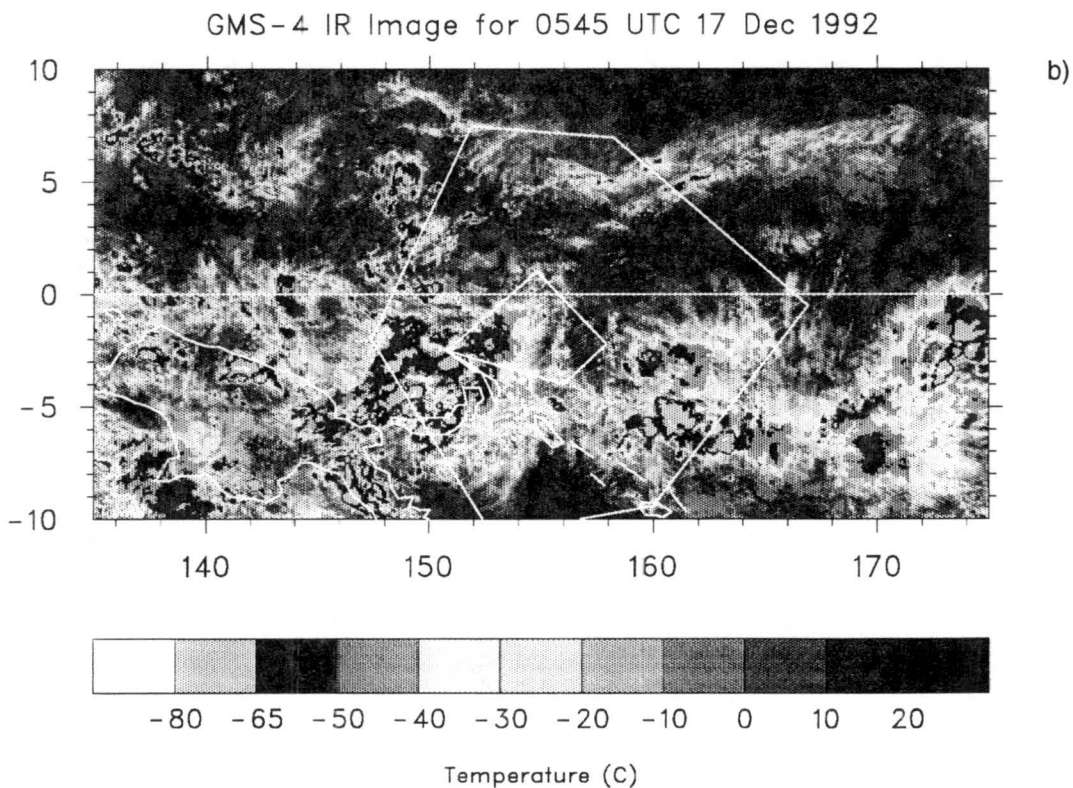
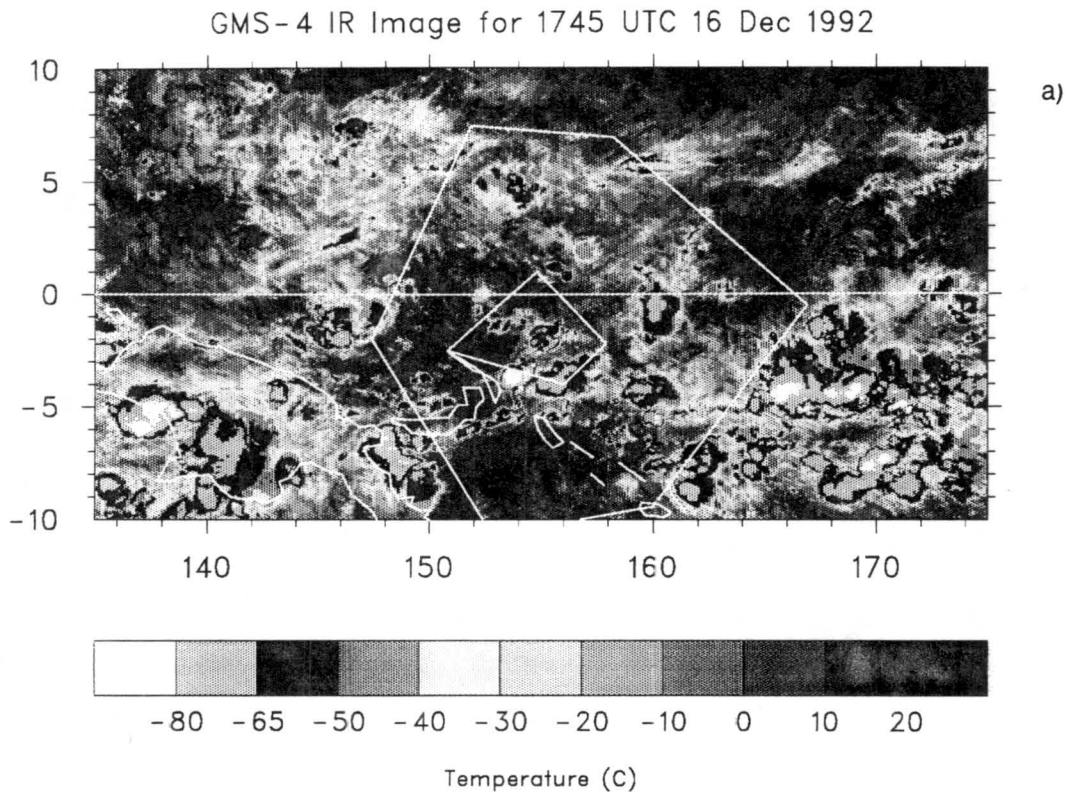
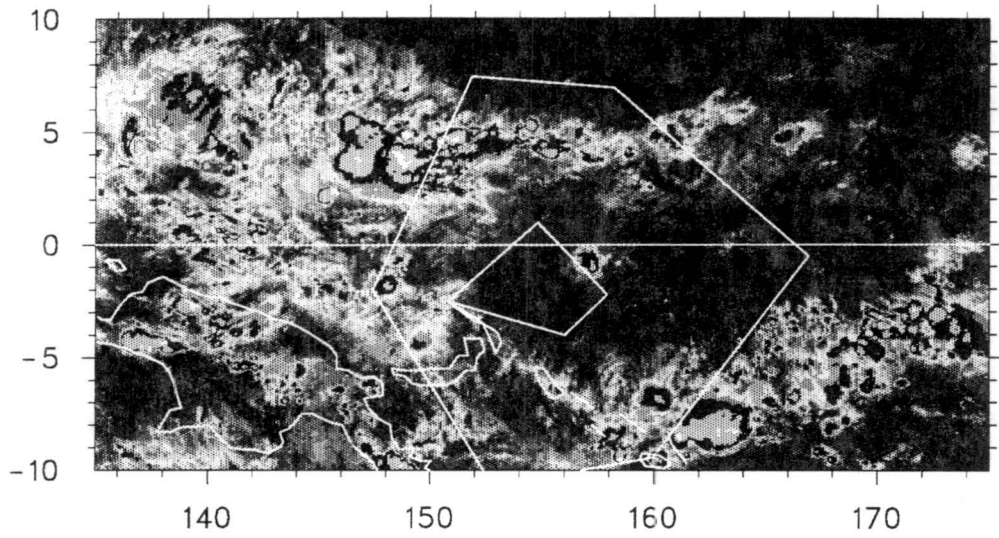
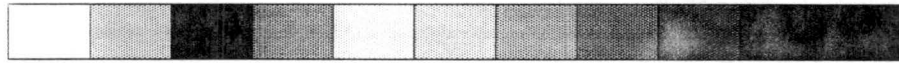


Figure 4.1: GMS-IR satellite images of the TOGA COARE region at (a) 1745 UTC 16 December, (b) 0545 UTC 17 December, (c) 0645 UTC 18 December, and (d) 1745 UTC 18 December.

GMS-4 IR Image for 0645 UTC 18 Dec 1992



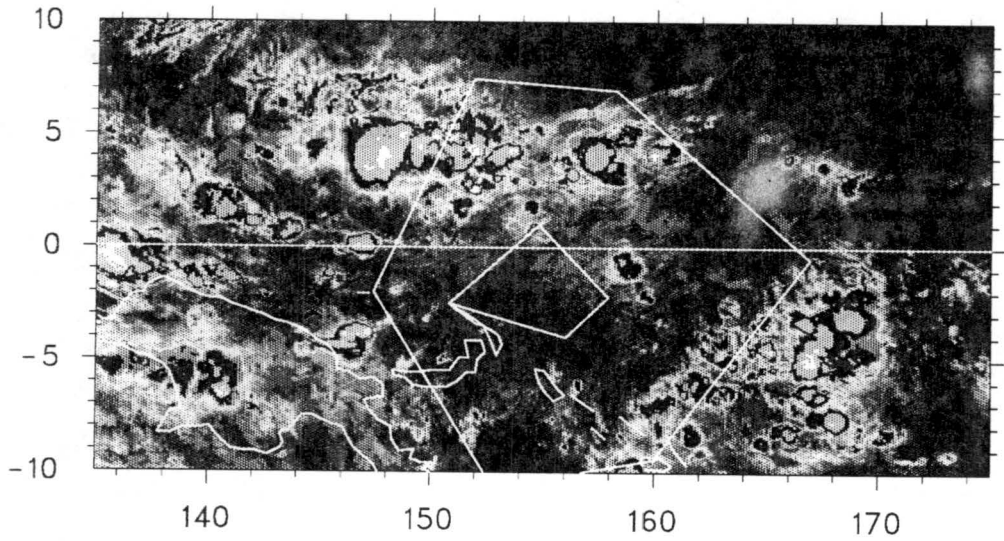
c)



-80 -65 -50 -40 -30 -20 -10 0 10 20

Temperature (C)

GMS-4 IR Image for 1745 UTC 18 Dec 1992



d)



-80 -65 -50 -40 -30 -20 -10 0 10 20

Temperature (C)

Figure 4.1: Continued.

OSA boundary. Cloud tops in this area were colder than -80°C . There were other, less organized areas of convection scattered across the OSA and IFA. The Northern Hemisphere convergence zone was present across the northern portions of the OSA, but was less pronounced than the Southern Hemisphere zone.

Twelve hours later, at 0545 UTC 17 December (Fig. 4.1b), the Southern Hemisphere band had become more prominent, likely a reflection of the Intertropical Convergence Zone (ITCZ) or equatorial trough. The positions of equatorial troughs over the western Pacific vary according to season, moving toward the summer hemisphere. The southern ITCZ was most active east of 145°E . Cloud tops in this area were colder than -65°C which corresponded to an altitude of 14 km. At this time, high clouds or deep convection remained near Kavieng on the western border of the IFA. The amount of deep convection was less at this time in the vicinity of both Kapingamarangi, which marked the northern border of the IFA, and Nauru, on the eastern border of the OSA just south of the equator. The northern band, generally between 3 and 8°N , remained less defined at this time.

By 0645 UTC 18 December (Fig. 4.1c), the area of generally clear and undisturbed conditions which had previously included Nauru, had expanded to cover all of the IFA and a large portion of the OSA near the equator. The two latitudinal bands of convergence, or equatorial troughs, were now well defined in the form of a "double-ITCZ" structure. The southern zone was most pronounced east of 160°E and between 3 and 10°S . The northern zone was located between 2 and 6°N with the deepest convection near 150°E .

The double-ITCZ structure persisted for the next several hours. By 1745 UTC 18 December (Fig. 4.1d), the northern zone of convergence had become the more active as the southern zone began to wane. During the twelve hours that followed, the northern band progressed southward toward the equator. By 0545 UTC 19 December (not shown), the northern band was in close proximity to Kapingamarangi, covering the northernmost section of the IFA.

4.1.2 Thermodynamic and Kinematic Structure

Figure 4.2 shows a four-day time series of specific humidity profiles taken every six hours at Nauru from 1200 UTC 16 December to 0600 UTC 20 December. At 1800 UTC

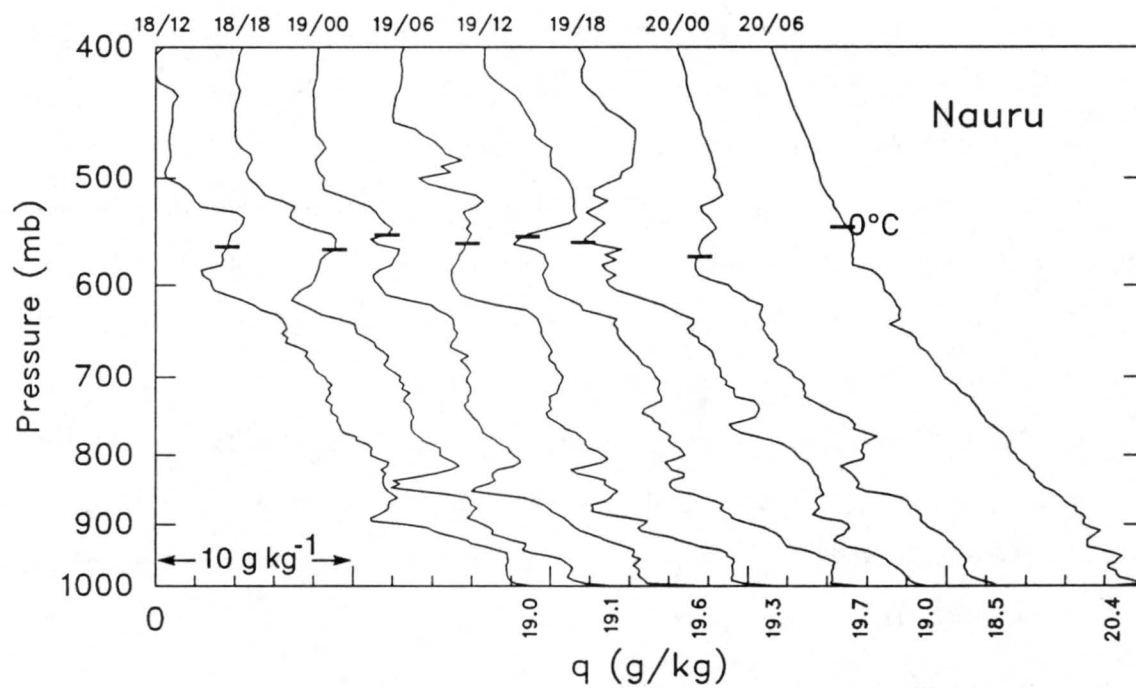
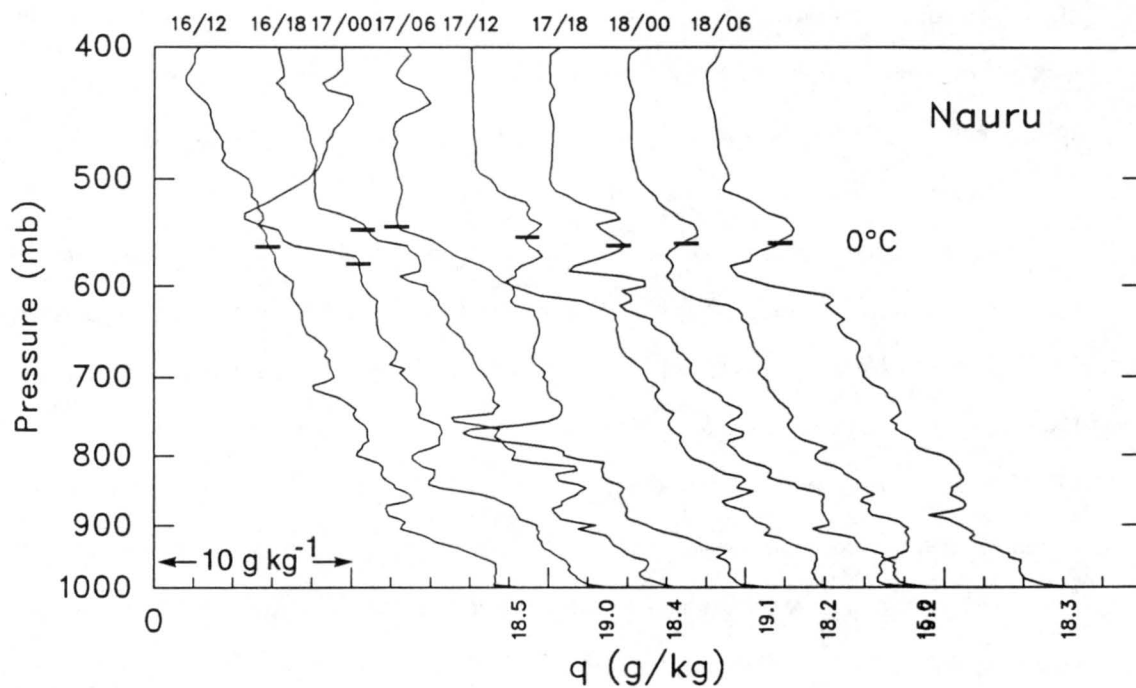


Figure 4.2: Specific humidity time series for Nauru from 1200 UTC 16 December to 0600 UTC 20 December. The scale for each curve is shifted to the right by 4 g kg^{-1} to avoid overlap. Day/GMT hour is indicated along the top.

16 December, a layer which had dried rapidly (on the order of 6 g kg^{-1}) was found in the midtroposphere between 560 and 500 mb. The base of this layer was near the melting level. This dry layer did not exist for a several-day period prior to this time.

By 0600 UTC 17 December, the mid-tropospheric dry layer descended and deepened to more than 150 mb, extending from 600 mb to 440 mb. During the six hours that followed, the profile changed significantly and exhibited a reversal in specific humidity near the freezing level by 1200 UTC 17 December. The shallow, moist layer near the freezing level was surrounded by very dry conditions aloft and below. The mid-tropospheric q reversal persisted for the next 60 hours, lasting through 0000 UTC 20 December.

At lower levels, a significant inflection in the q profiles can be seen near 800 mb, particularly from 0600 UTC 18 December to 0600 UTC 19 December. Similar reversals in q over the tropical oceans have been reported by Betts and Albrecht (1987) near the top of the tradewind cumulus layer. They hypothesized that the normal q gradient was reversed by penetrative downdrafts driven by the evaporation of falling precipitation. Figure 4.3 shows the θ_e and θ_{es} profiles computed for Nauru at 0600 UTC 18 December. The structure in the lower troposphere (below 770 mb) resembles that found by Betts and Albrecht (1987). However, in this situation a similar feature is found in the midtroposphere characterized by a θ_e maximum and θ_{es} minimum near 550 mb.

For the same four-day period, the specific humidity profiles at Kapingamarangi are shown in Fig. 4.4. The onset of a dry layer in the midtroposphere, similar to that found at Nauru, was observed at 1800 UTC 16 December. Once again, after six to twelve hours of deepening, the dry regime was split by a shallow, moist layer near the 0°C level. The result was a pronounced inflection in q , consistent with that observed at Nauru, lasting in excess of two days. The lower extent of dry air at Kapingamarangi was observed to descend 100 mb during the period. A recurring, low-level inflection in specific humidity, as was observed at Nauru, was not found at Kapingamarangi during this period.

Figure 4.5 shows the specific humidity time series for Kavieng during the same period. The onset of the rapid, mid-tropospheric drying occurred here at 0000 UTC 18 December, more than 24 hours after it began at both Kapingamarangi and Nauru. By 0600 UTC 18

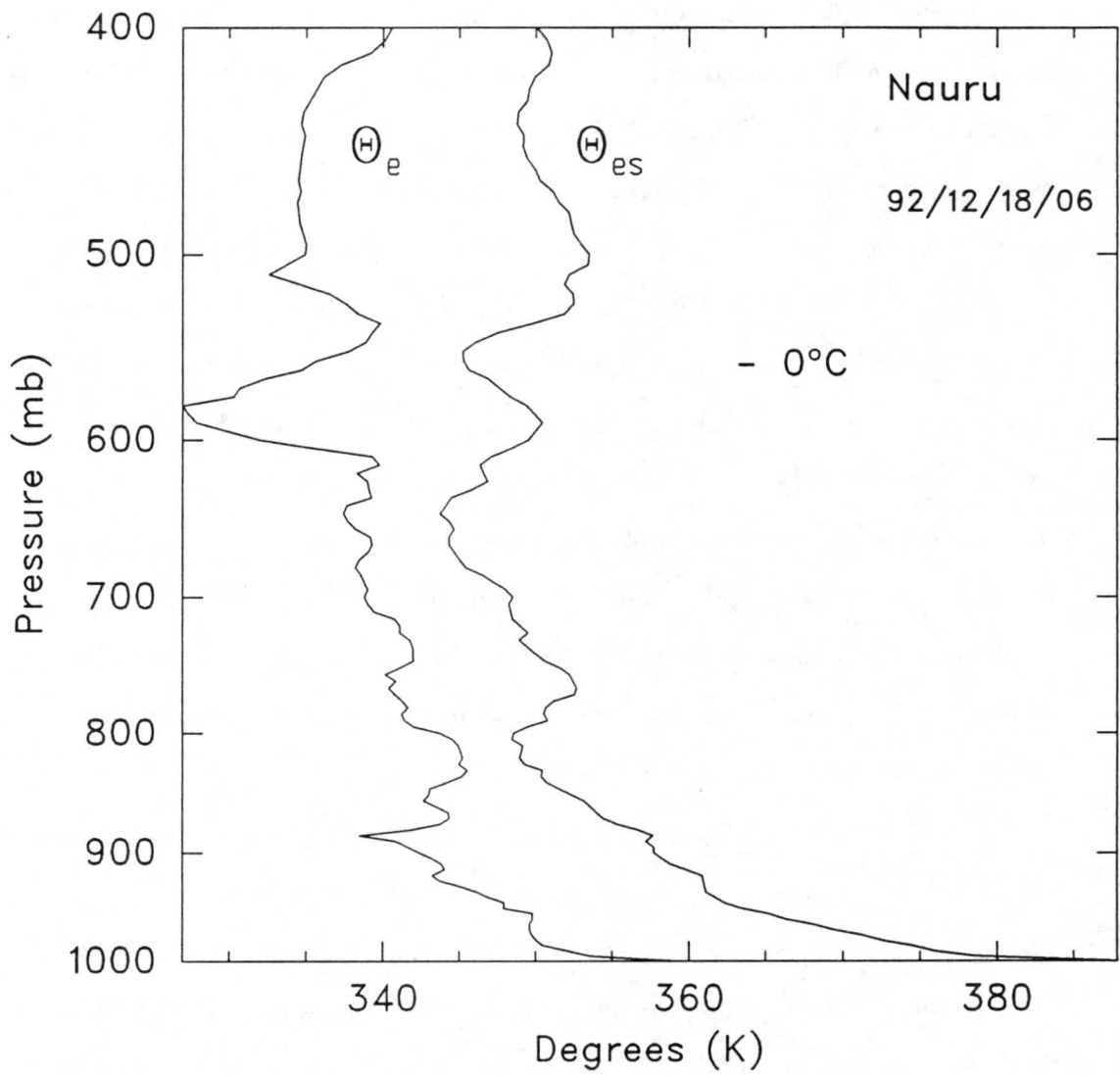


Figure 4.3: Equivalent potential temperature and saturation equivalent potential temperature profiles for Nauru at 0600 UTC 18 December.

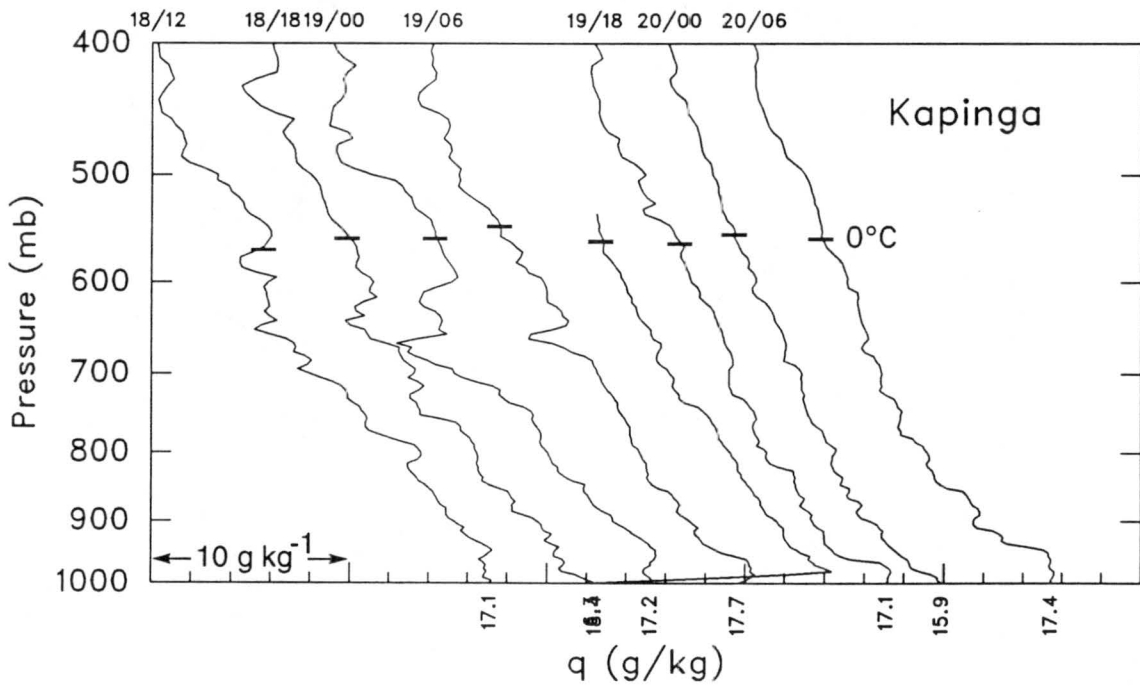
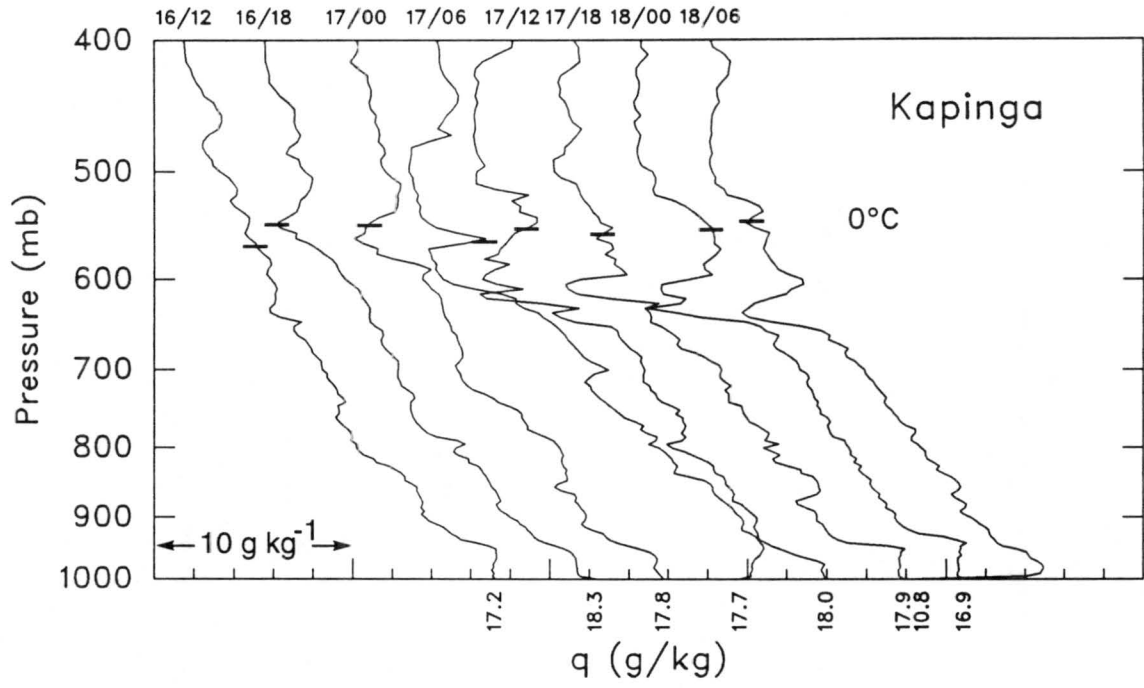


Figure 4.4: Same as in Fig. 4.2, except for Kapingamarangi.

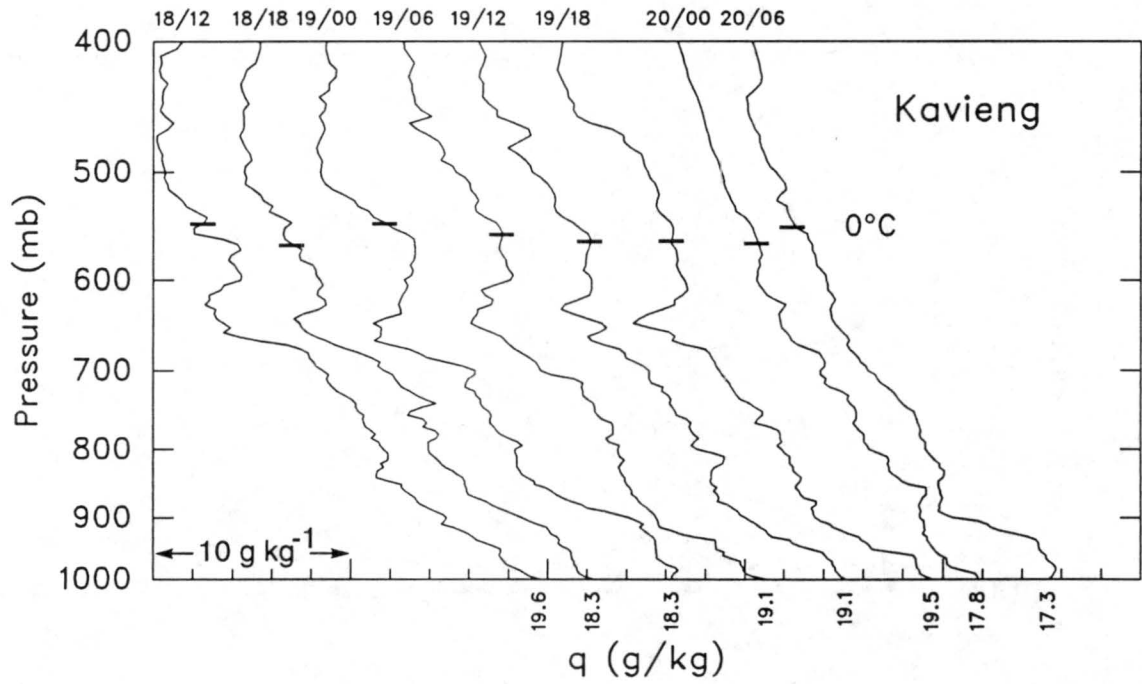
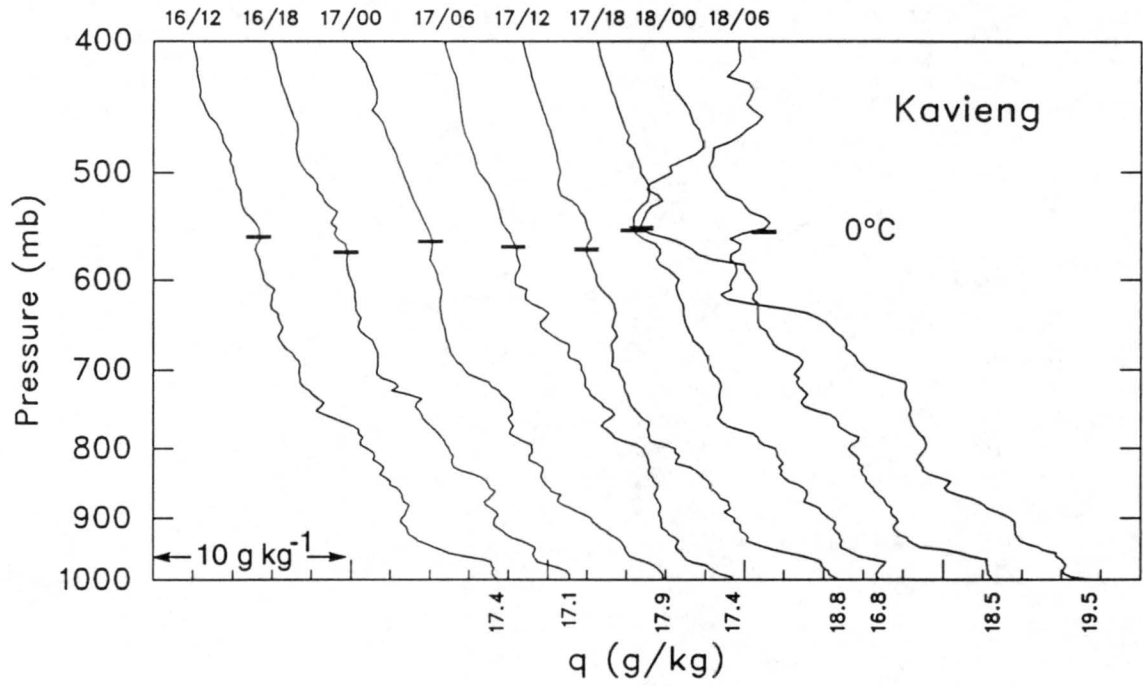


Figure 4.5: Same as in Fig. 4.2, except for Kavieng.

December, the dry regime had been subdivided into two layers, one above and one below the freezing level. A local maximum of q was observed near the freezing level.

A series of soundings for Nauru shows the evolution of the mid-tropospheric drying and subsequent q inflection (Figs. 4.6a-d). At 1200 UTC 16 December, the Nauru sounding

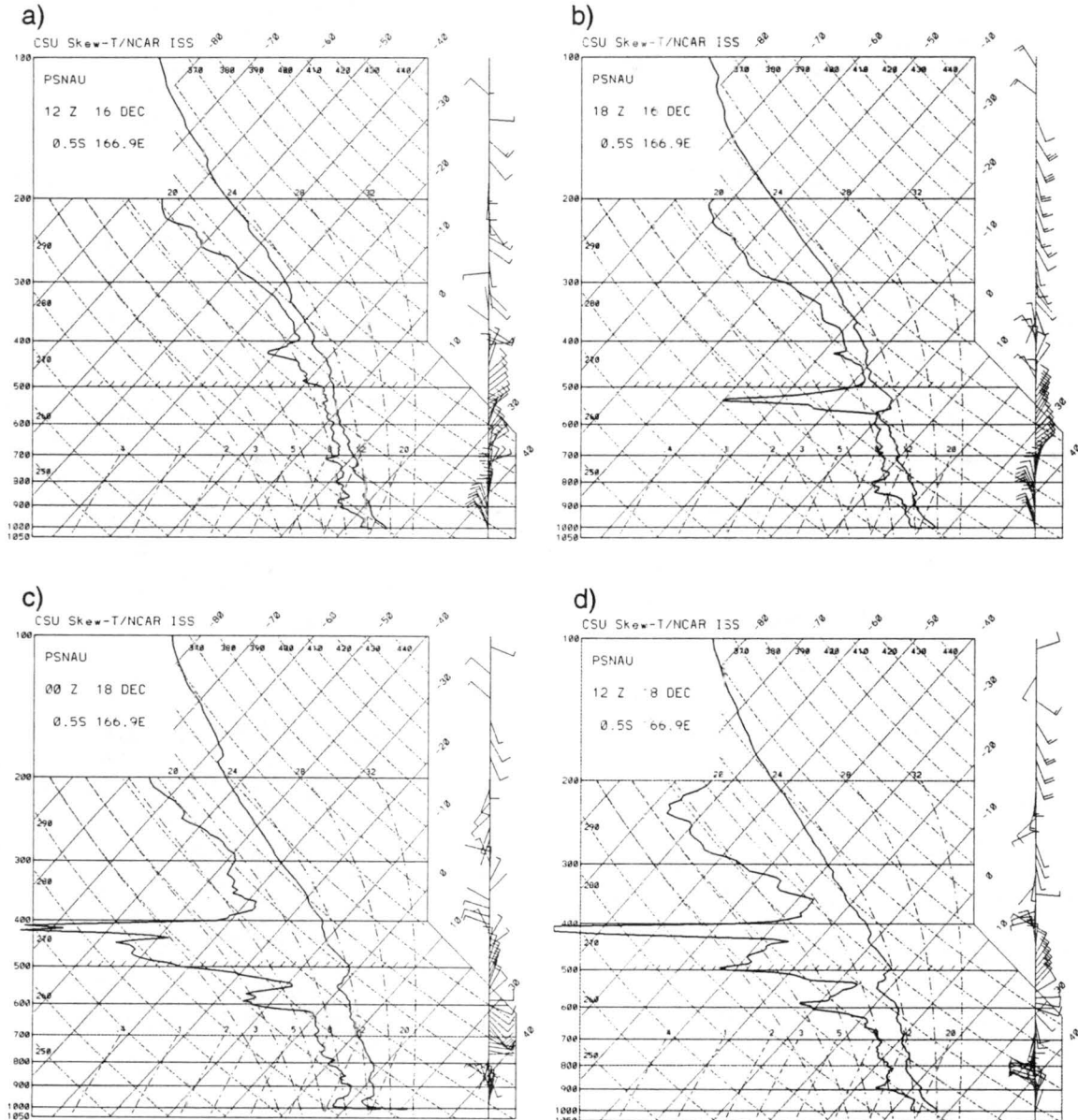


Figure 4.6: Skew-T diagrams for Nauru at a) 1200 UTC 16 December, b) 1800 UTC 16 December, c) 0000 UTC 18 December, and (d) 1200 UTC 18 December.

was moist through the entire troposphere (Fig. 4.6a). Winds were light and variable with speeds less than 5 m s^{-1} . In just six hours (Fig. 4.6b), a 70 mb-thick dry layer

developed near 540 mb. In addition, the base of the dry layer corresponded well with the base of an isothermal layer at the freezing level. The dryness in this layer indicates that the isothermal layer is not a direct result of melting over Nauru, a process which is known to produce isothermal layers in precipitation systems (Findeisen 1940). Similar temperature inversions near the melting level were observed in the eastern Pacific by Haraguchi (1968). Coincident with the warming and drying, northeast flow between 600 and 500 mb intensified markedly to 10 to 12.5 m s⁻¹. Southeast flow above 300 mb had also strengthened from light and variable to 7.5 to 15 m s⁻¹. The strengthening of the upper-level flow may have been the result of outflow from the large MCS located south of Nauru (Fig. 4.1a).

By 0000 UTC 18 December (Fig. 4.6c), the dry layer had more than doubled in depth and was now centered at 500 mb. An isothermal layer remained at the freezing level. Immediately below the temperature inversion, the sonde measured a shallow, moist layer which was reflected as a q inversion on the specific humidity time series. Below the moist layer, the dry regime resumed. The strongest winds at this time were at and just above the freezing level where northeast flow at 7.5 m s⁻¹ was observed.

The 1200 UTC 18 December sounding at Nauru (Fig. 4.6d) was nearly identical to the sounding from twelve hours prior. A dry atmosphere between 620 and 380 mb was divided by a shallow, moist layer near 550 mb. The moist air coincided with the base of an isothermal layer which persisted just above the melting level. The increase in southeast winds above the 250 mb level may have been the outflow response to the large MCS which had redeveloped south of Nauru.

The nearly simultaneous nature of this feature across a large horizontal domain (on the order of 2000 km) may indicate a possible link to a synoptic-scale pattern. Although the onset was delayed by 24 hours at Kavieng, the westernmost of the three observation sites, the depth, duration, and level of the q maximum were consistent at all three locations.

The mid-tropospheric drying was accompanied by a marked increase in northeasterly flow at each of the stations examined in this case. Skew-T diagrams for 0000 UTC and 1200 UTC 16 December at Kwajalein (8.7°N, 167.7°E) and Majuro (7.1°N, 171.4°E), located

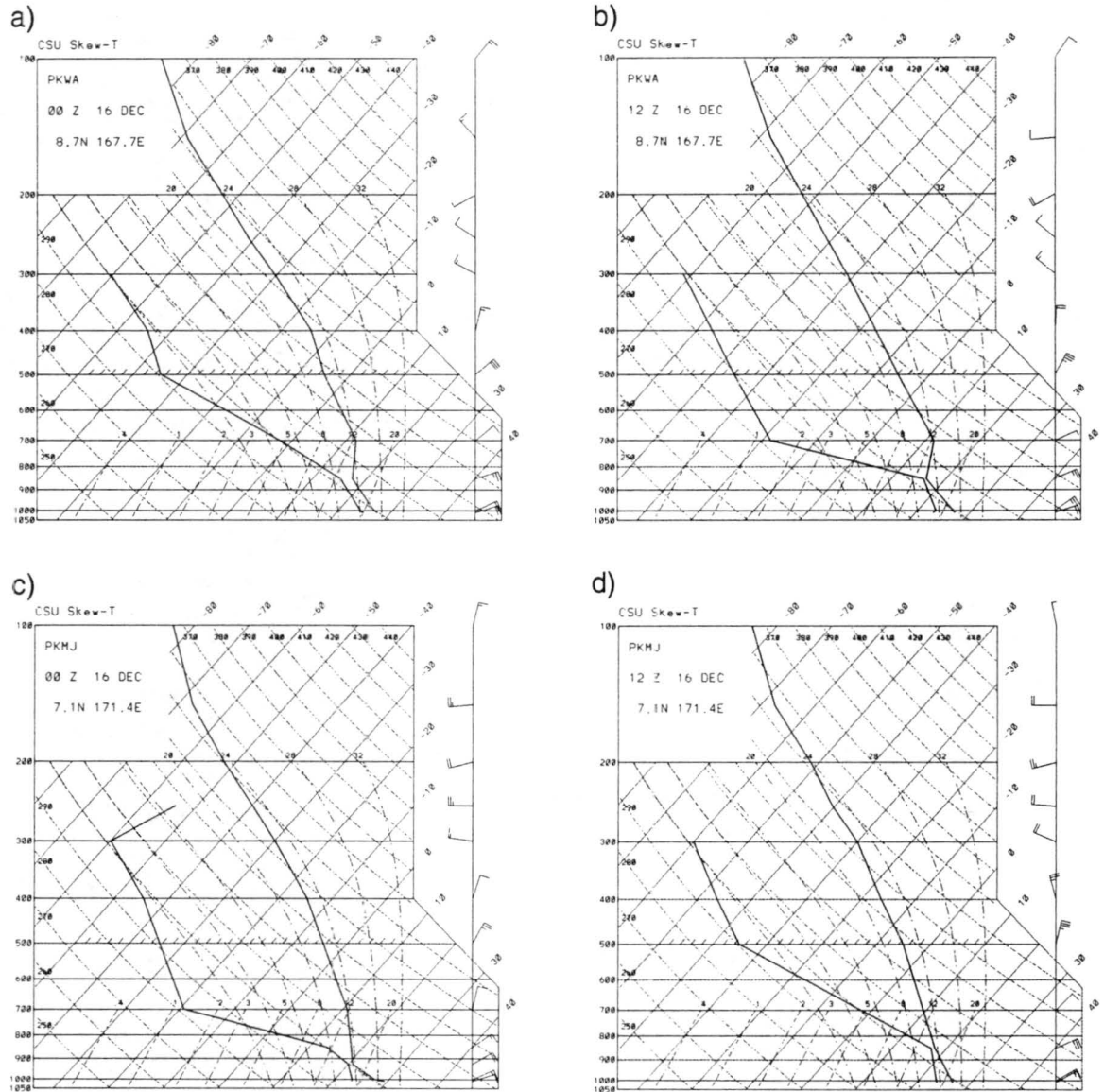


Figure 4.7: Skew-T diagrams for Kwajalein at (a) 0000 UTC 16 December and (b) 1200 UTC 16 December and Majuro at (c) 0000 UTC 16 December and (d) 1200 UTC 16 December.

upstream under these conditions, are shown in Figs. 4.7a-d. Only mandatory level data (WMO 1987) were reported, leaving many shallow features unresolved. The soundings do, however, depict very dry conditions above the CBL along with strong northeasterly flow at 500 mb (12.5 to 17.5 m s⁻¹). These soundings at Kwajalein and Majuro suggest that the mid-tropospheric features observed during case I over the OSA and IFA may have been advected from higher latitudes northeast of the sounding arrays.

A series of east-west cross-sections of relative humidity (with respect to liquid water at all temperatures) are shown in Figs. 4.8a-d. At 0000 UTC 16 December (Fig. 4.8a), low relative humidities ($\leq 35\%$) above 500 mb were observed east of 174°E . These low RH values descended and spread westward during the next three days (Figs. 4.8a-c), perhaps under the influence of northeasterly advection. Advective effects and other possible explanations for the nearly simultaneous behavior of moisture and temperature inversions near 0°C will be explored in chapter 6.

The recurring mid-tropospheric stable layer is illustrated in a time series of potential temperature profiles computed from 1200 UTC 16 December to 0600 UTC 20 December at Nauru (Fig. 4.9). The 1800 UTC 16 December profile shows the first indication of a stable layer near 550 mb, where the potential temperature increased more rapidly with height. The marked stable layer underwent a series of complex changes over the next 18 hours, including a separation into two distinct parts, but was observed through 1200 UTC 18 December.

A series of north-south cross-sections of relative humidity from 10°S to 10°N representing averages of gridded data from 150°E to 160°E are shown in Figs. 4.10a-c. At 0000 UTC 17 December (Fig. 4.10a), a dry layer appeared between 600 and 500 mb just north of the equator. This feature may not have been completely real since there was an absence of sounding data between Kapingamarangi and Ponape. By 0000 UTC 18 December (Fig. 4.10b), a local maximum of relative humidity was observed near the melting level along the equator. Twelve hours later (Fig. 4.10c), a layer with relative humidity values greater than 60 % had expanded southward into the Southern Hemisphere. This shallow, moist layer was bounded aloft and below by significantly drier air. These cross-sections reveal the broadscale nature of the moist layer.

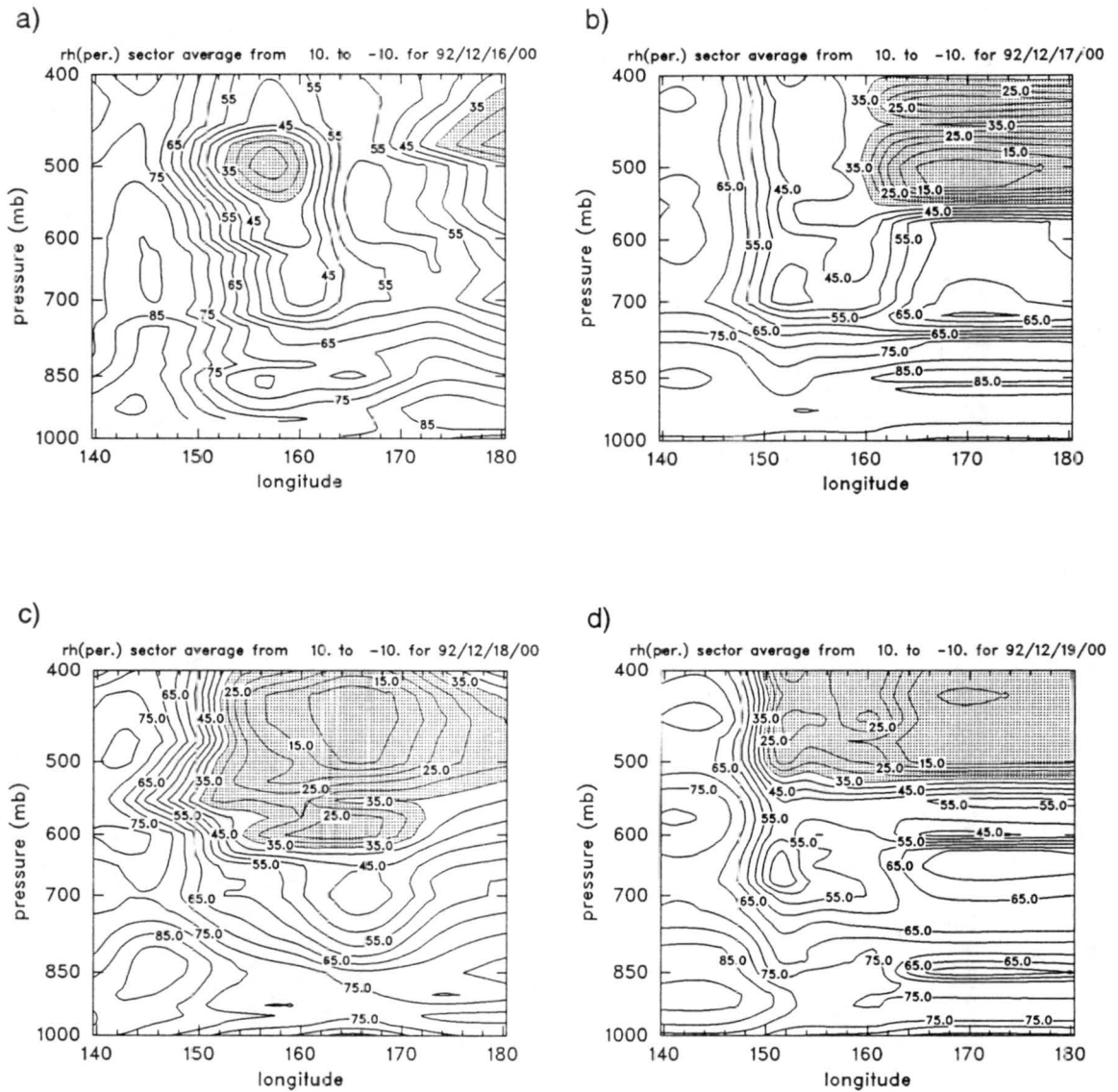


Figure 4.8: East-west relative humidity cross-sections of LSA from 140°E to 180°E averaged from 10°S to 10°N at (a) 0000 UTC 16 December, (b) 0000 UTC 17 December, (c) 0000 UTC 18 December, and (d) 0000 UTC 19 December. Contours of relative humidity are every 5%. Values $\leq 35\%$ are shaded.

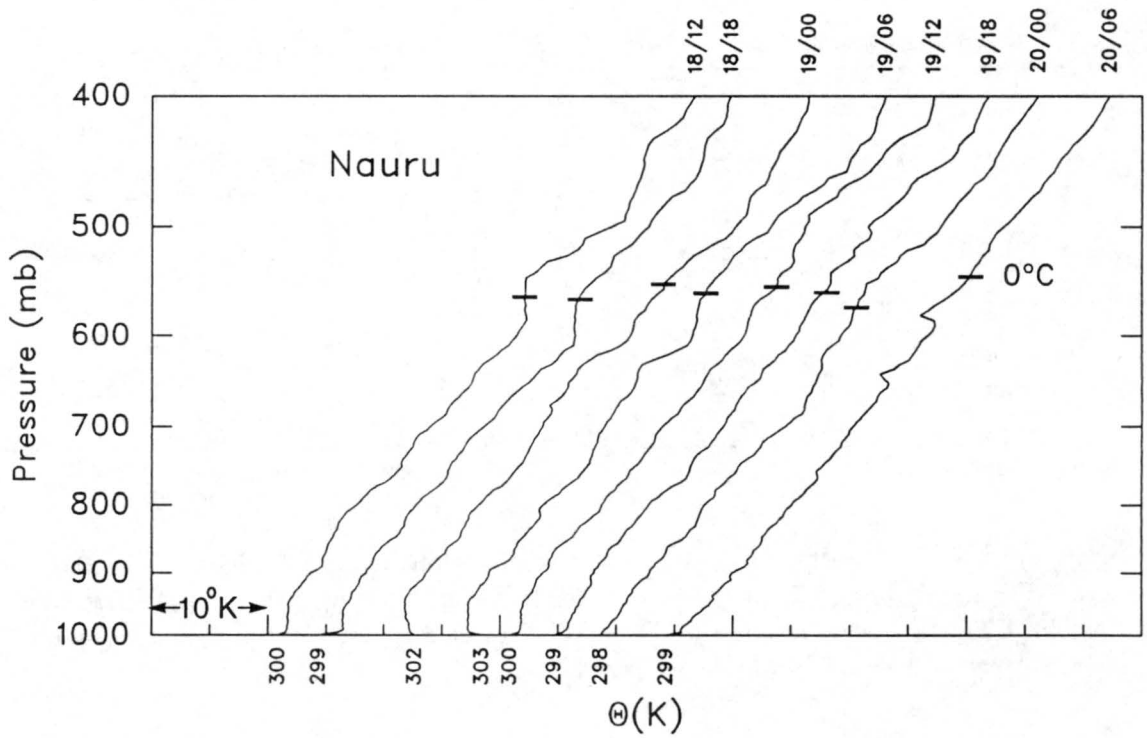
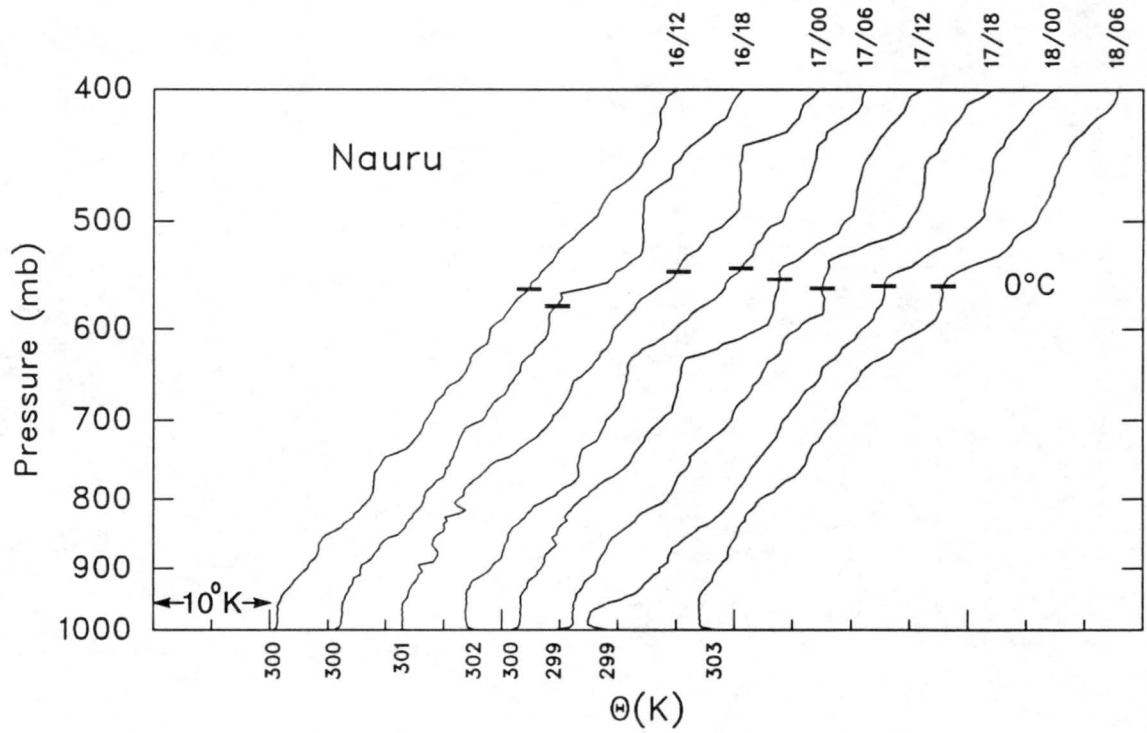


Figure 4.9: Potential temperature time series for Nauru from 1200 UTC 16 December to 0600 UTC 20 December. The scale for each curve is shifted to the right by 5°K to avoid overlap. Day/GMT hour is indicated along the top.

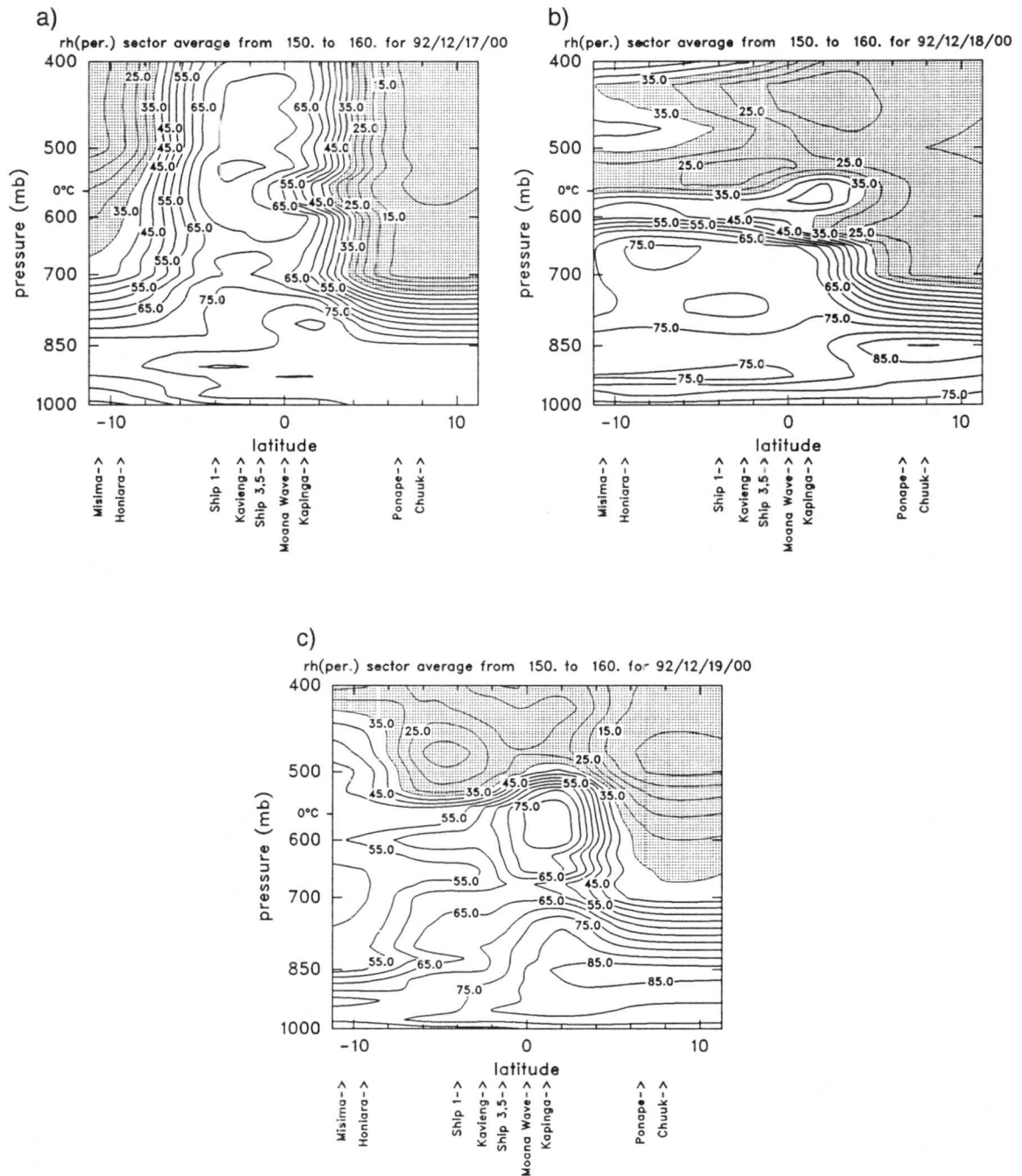


Figure 4.10: North-south relative humidity cross-sections of LSA from 10°S to 10°N averaged from 150°E to 160°E at (a) 0000 UTC 17 December, (b) 0000 UTC 18 December, and (c) 0000 UTC 19 December. Contours of relative humidity are every 5%. Values $\leq 35\%$ are shaded.

4.2 Case II - 1200 UTC 29 December 1992 to 1200 UTC 1 January 1993

The next extended period of mid-tropospheric moisture and temperature inversions was observed from 29 December 1992 to 1 January 1993. The inversions were most pronounced over the western portions of the sounding arrays. The analysis for this case will focus on soundings taken at Manus and Kavieng.

4.2.1 Satellite Overview

The sequence of satellite images (Figs. 4.11a-d) from 29 and 30 December illustrate the pattern of convection over the LSA. The deepest convection was generally organized in latitudinal bands that were horizontally removed from the ISS sites under examination. The mid-tropospheric temperature and moisture inversions were observed in areas that appeared relatively undisturbed.

At 0645 UTC 29 December (Fig. 4.11a), a large MCS was observed north of Nauru. Cloud tops associated with the MCS were colder than -65°C . A smaller area of deep convection was also found east of Kavieng in the western half of the IFA. Conditions were much less convective near Manus and Kapingamarangi.

Twelve hours later (Fig. 4.11b), more suppressed conditions had replaced the convection over the western IFA and west central OSA. Deep convection associated with an area of convergence remained east of 156°E between the equator and 5°S . Kapingamarangi was near the western boundary of a cirrus cloud shield that extended to 152°E .

By 0545 UTC 30 December (Fig. 4.11c), a MCS just north of the equator had intensified with a large area of cloud tops colder than -65°C . The convection associated with the system was oriented in a latitudinal band from 160°E to 168°E . The dry regime immediately south of the equator had expanded eastward through the eastern border of the OSA. All of the ISS sites, with the exception of Nauru and Kapingamarangi, remained away from any deep convection.

By 1745 UTC 30 December (Fig. 4.11d), the deep convection in the Northern Hemisphere had dissipated considerably. The dry intrusion immediately south of the equator separated two bands of convection. The deepest convection was associated with the MCS

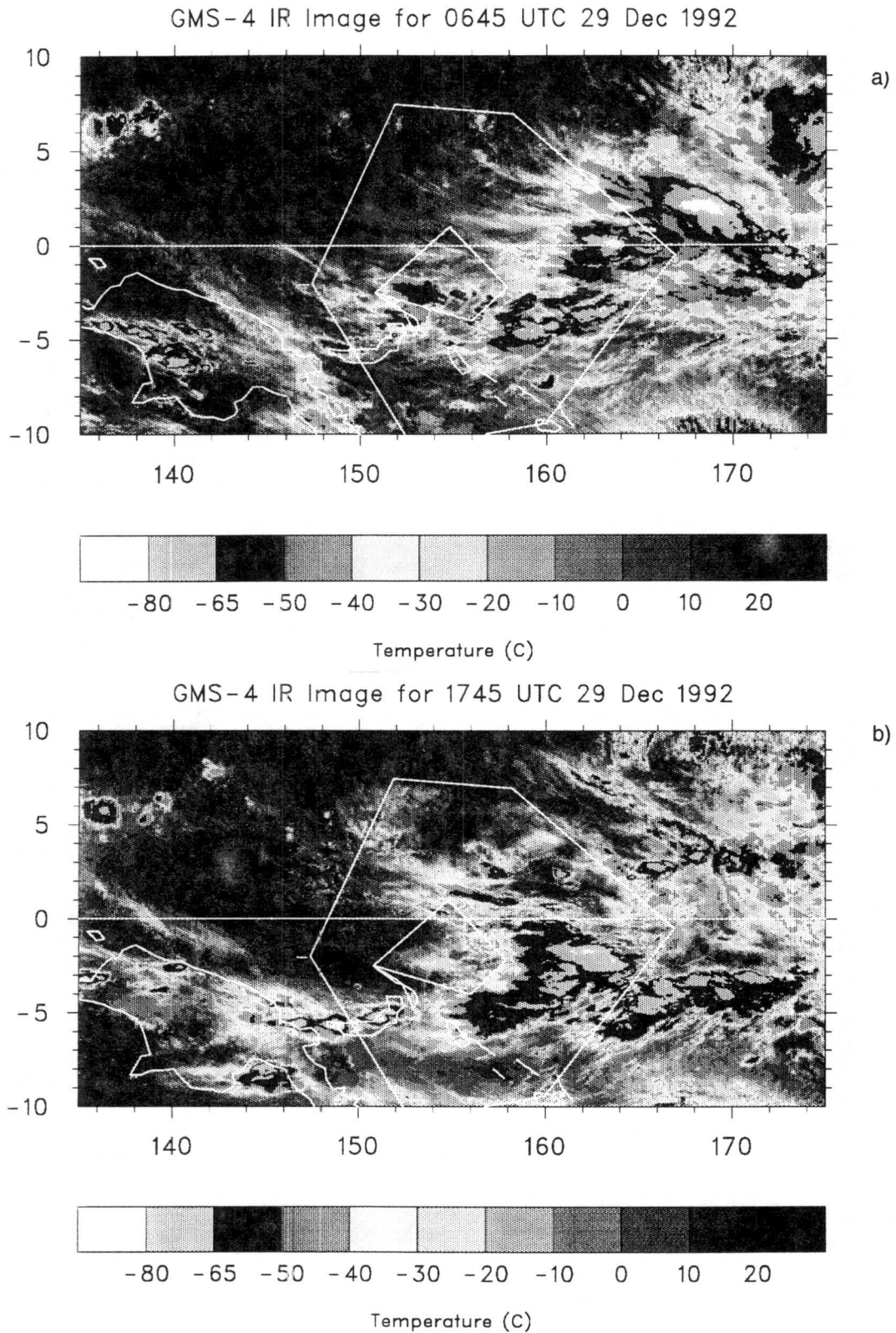
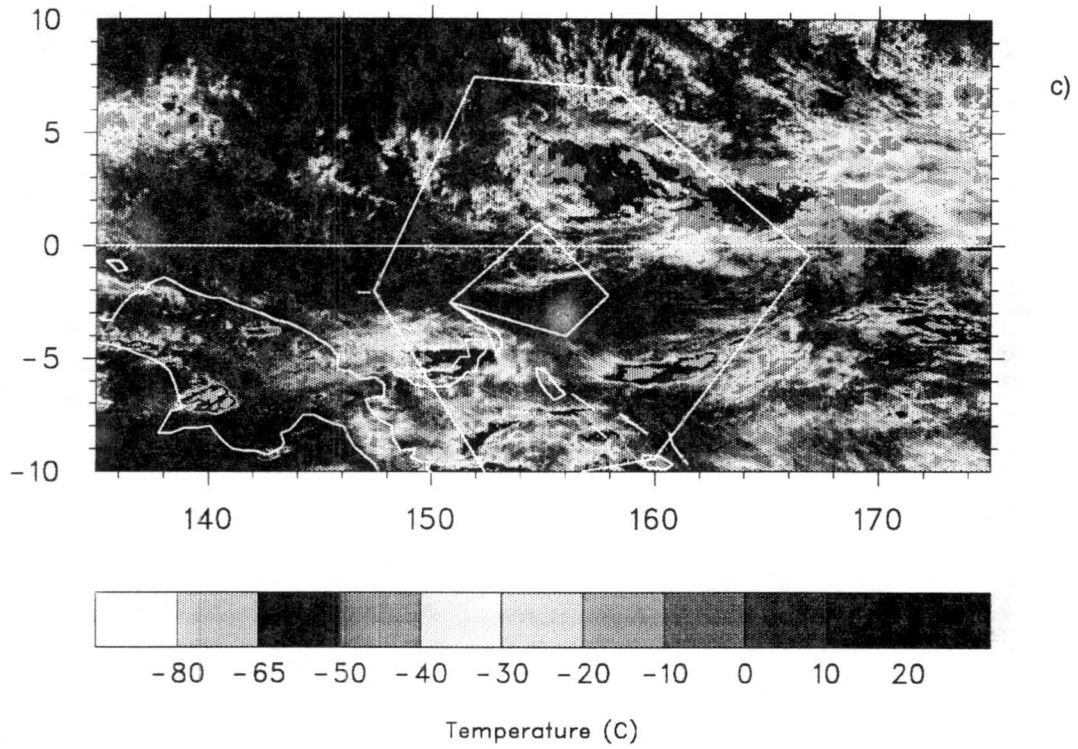


Figure 4.11: GMS-IR satellite images of the TOGA COARE region at (a) 0645 UTC 29 December, (b) 1745 UTC 29 December, (c) 0545 UTC 30 December, and (d) 1745 UTC 30 December.

GMS-4 IR Image for 0545 UTC 30 Dec 1992



GMS-4 IR Image for 1745 UTC 30 Dec 1992

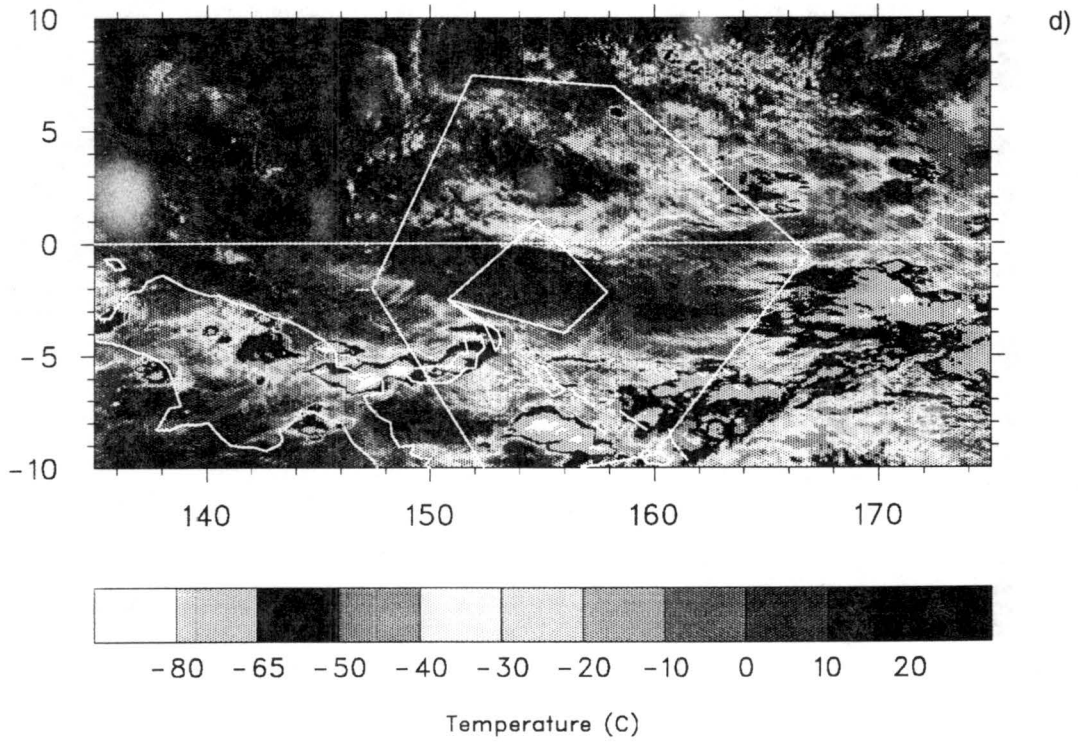


Figure 4.11: Continued.

located east of 160°E. Cirrus outflow from an area of convection over the Salomon Islands (see Fig. 3.2) had spread to just south of Kavieng and covered Manus. Conditions north and west of the IFA/OSA region were noticeably undisturbed.

4.2.2 Thermodynamic and Kinematic Structure

Figure 4.12 shows a time series of specific humidity profiles at Manus spanning the four days from 0000 UTC 29 December to 1800 UTC 1 January 1993. Data from the 1200 UTC 31 December sounding were missing. Mid-tropospheric thermodynamic and kinematic features consistent with case I were observed during this period.

The onset of a mid-tropospheric dry layer was observed at 0600 UTC 29 December. The dry regime deepened considerably over the next six hours, extending to near 650 mb by 1200 UTC 29 December. The most pronounced drying (on the order of 6 g kg^{-1}) had occurred in a 50-mb layer centered at 625 mb. During the next 18 hours, the dry air descended to near the 700 mb level. The dry regime above 700 mb extended through 400 mb, but was interrupted by a shallow, moist layer near the melting level (about 560 mb). The result was a reversal in q which lasted for a period of 66 hours.

A four-day time series of specific humidity profiles at Kavieng (Fig. 4.13) from 0000 UTC 29 December 1992 to 1800 UTC 1 January 1993 shows a similar sequence of events. The inflection in q near 500 mb at 1200 UTC 29 December suggests that significantly drier conditions were measured above this level. The onset of similar drying was observed at Manus just six hours prior. Dry air extended to as low as 650 mb at Kavieng by 1800 UTC 29 December.

By 0000 UTC 30 December at Kavieng, a local maximum in q near the 0°C level was bounded above and below by significantly drier air. The inflection in specific humidity that resulted lasted for the next 60 hours. The recurring q inflection measured at both Kavieng and Manus dissipated at about 1200 UTC 1 January 1993.

Figure 4.14 depicts the θ_e and θ_{es} profiles computed from the 1200 UTC 30 December sounding at Kavieng. A θ_e maximum and θ_{es} minimum can be seen near the melting level. The θ_e and θ_{es} signatures found near the 0°C level resemble those found by Betts and Albrecht (1987) in the lower troposphere. These lower tropospheric features in θ_e and θ_{es} ,

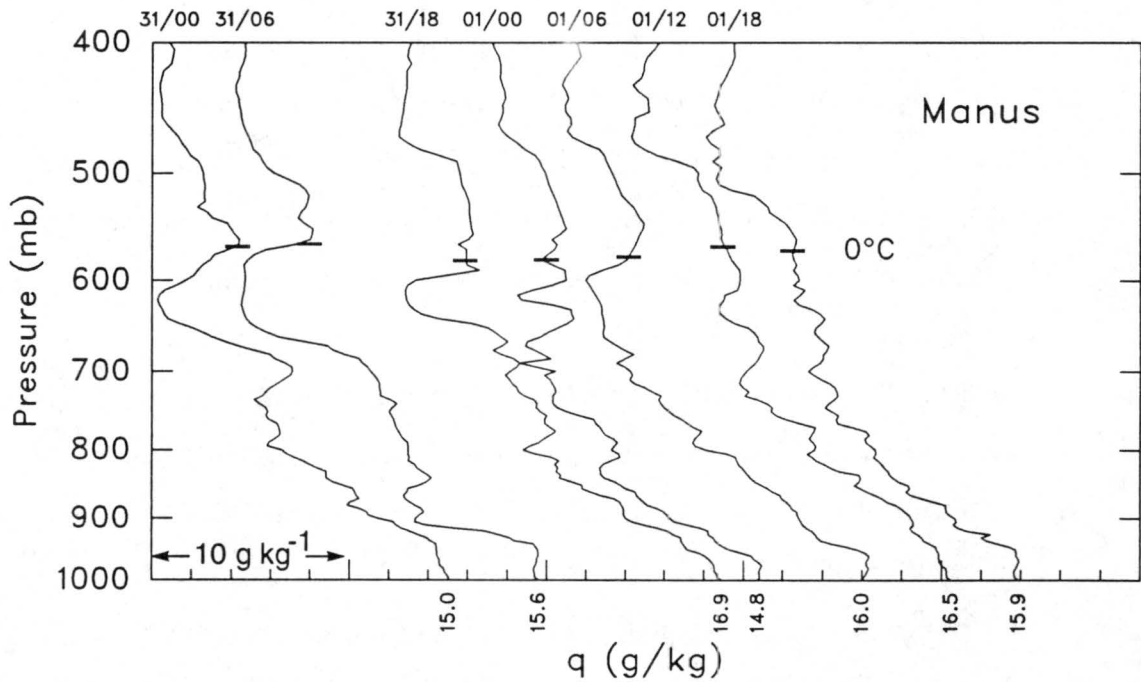
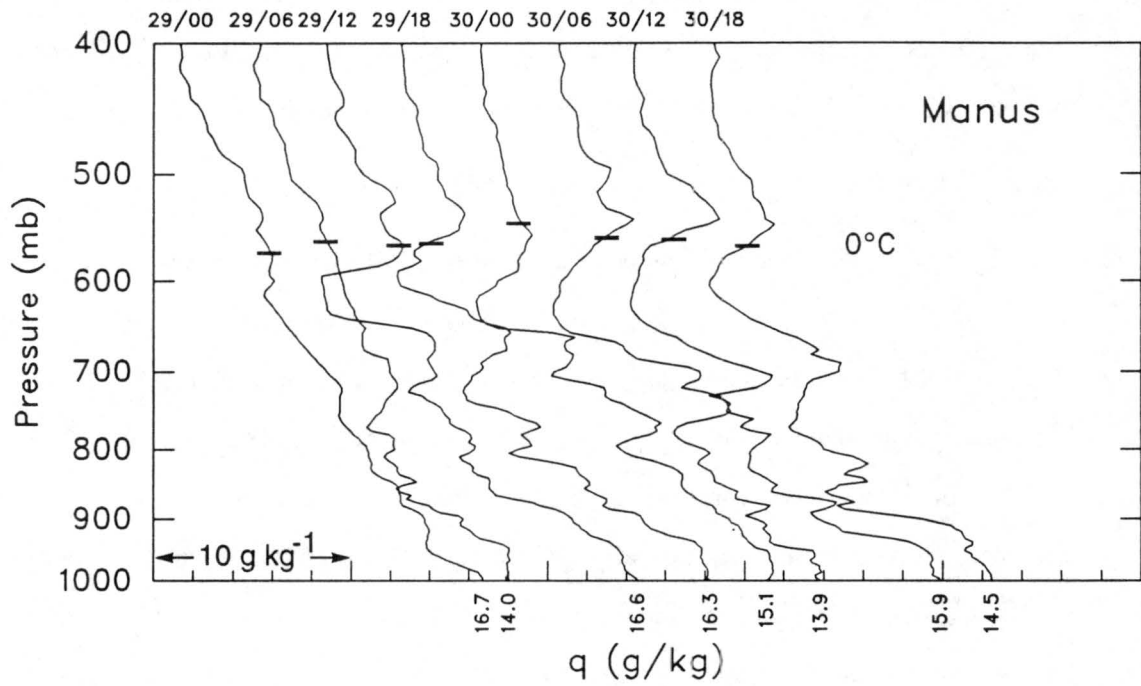


Figure 4.12: Specific humidity time series for Manus from 0000 UTC 29 December to 1800 UTC 1 January 1993. The scale for each curve is shifted to the right by 4 g kg^{-1} to avoid overlap. Day/GMT hour is indicated along the top.

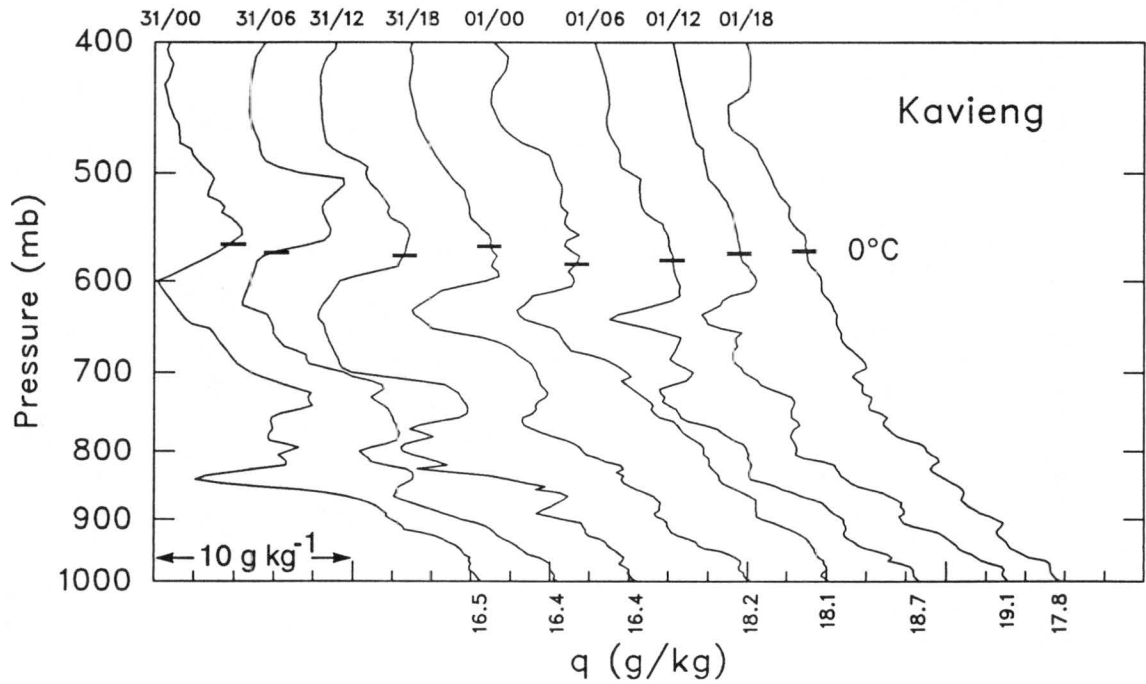
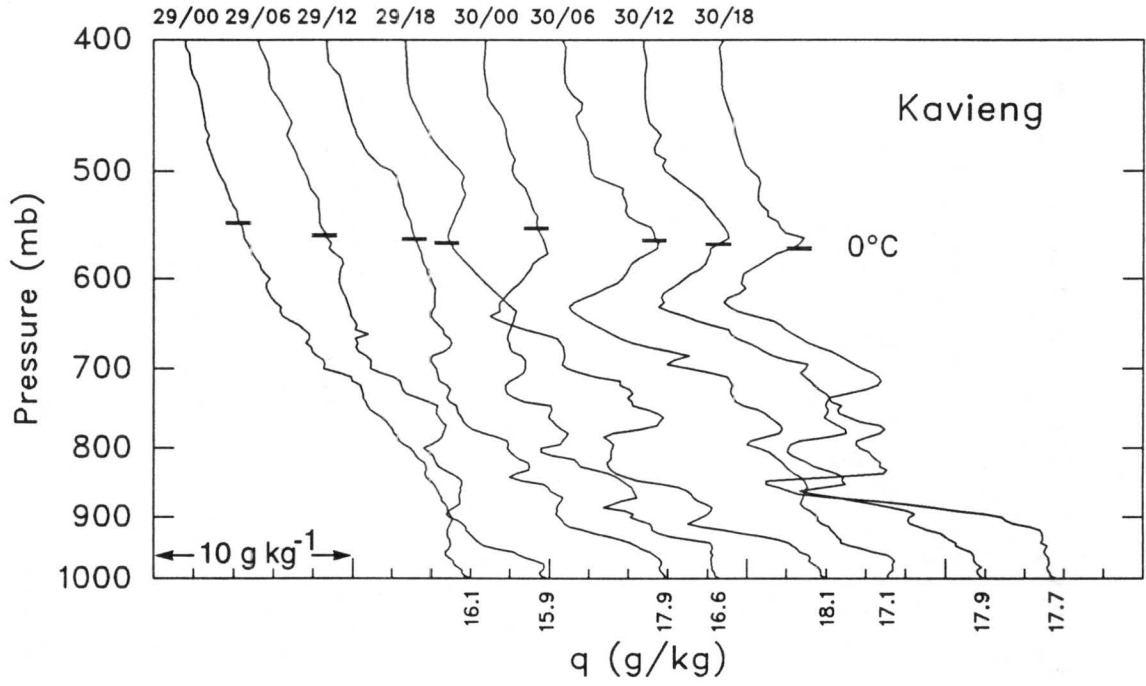


Figure 4.13: Same as in Fig. 4.12, except for Kavieng.

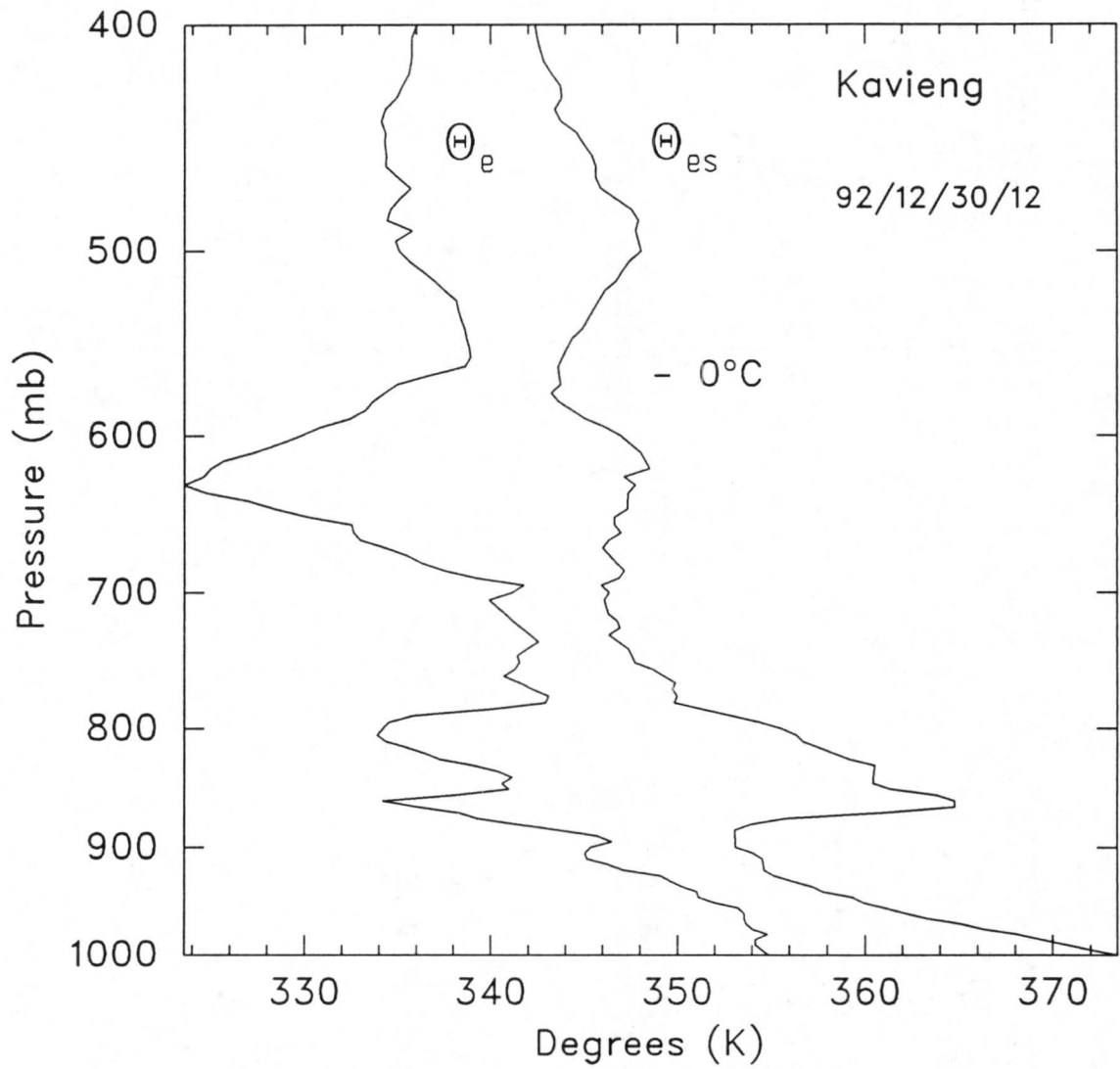


Figure 4.14: Equivalent potential temperature and saturation equivalent potential temperature profiles for Kavieng at 1200 UTC 30 December.

also evident in Fig. 4.14 near 900 mb, were linked to q reversals by Betts and Albrecht (1987).

A series of upper-air soundings from Kavieng is shown in Figs. 4.15a-h. Similar conditions were found on soundings taken at Manus. The 0600 UTC 29 December sounding at Kavieng (Fig. 4.15a) was moist through the entire troposphere with the exception of a dry layer between 350 and 300 mb.

Within six hours, the same dry layer had descended to 500 mb (Fig. 4.15b). The atmosphere below 500 mb remained moist. Winds at 1200 UTC 29 December (Fig. 4.15b) were westerly at 5 to 15 m s^{-1} below 500 mb. In the dry layer between 500 and 300 mb, winds were northwesterly through northerly at 7.5 to 10 m s^{-1} . Above 300 mb, easterly winds were as strong as 35 m s^{-1} .

By 0600 UTC 30 December (Fig. 4.15c), dry air at Kavieng began to appear between 600 and 700 mb. A shallow, moist layer at the melting level coincided with the base of a shallow temperature inversion. Westerly winds continued below 400 mb while east to northeasterly winds were observed above 400 mb.

The 1200 UTC 30 December sounding at Kavieng (Fig. 4.15d) was nearly identical to the sounding six hours prior. A stable layer, with a base near the freezing level, capped a shallow, moist layer near 560 mb. This stable, often isothermal, layer near the 0°C level persisted virtually unchanged for the next 24 hours (Figs. 4.15e-g). The moist regime was restricted to a shallow layer at the base of the stable layer for the same period.

By 0600 UTC 1 January 1993 (Fig. 4.15h), a pronounced dry layer centered at 640 mb remained, but the sonde was now moist above 600 mb. The result still produced an inflection in the specific humidity profile (Fig. 4.13) which lasted through 1200 UTC 1 January. The sonde had entered a cloud layer above 600 mb, yielding a moist-adiabatic sounding and destroying the isothermal layer. Satellite images (not shown) indicated that mid- and upper-level clouds associated with deep convection south of Kavieng had drifted over the site.

The kinematic features observed during this period at Kavieng can be related to the passage of a Madden-Julian Oscillation (MJO; Madden and Julian 1972). Three eastward-propagating MJOs were observed with the TOGA COARE sounding arrays during the

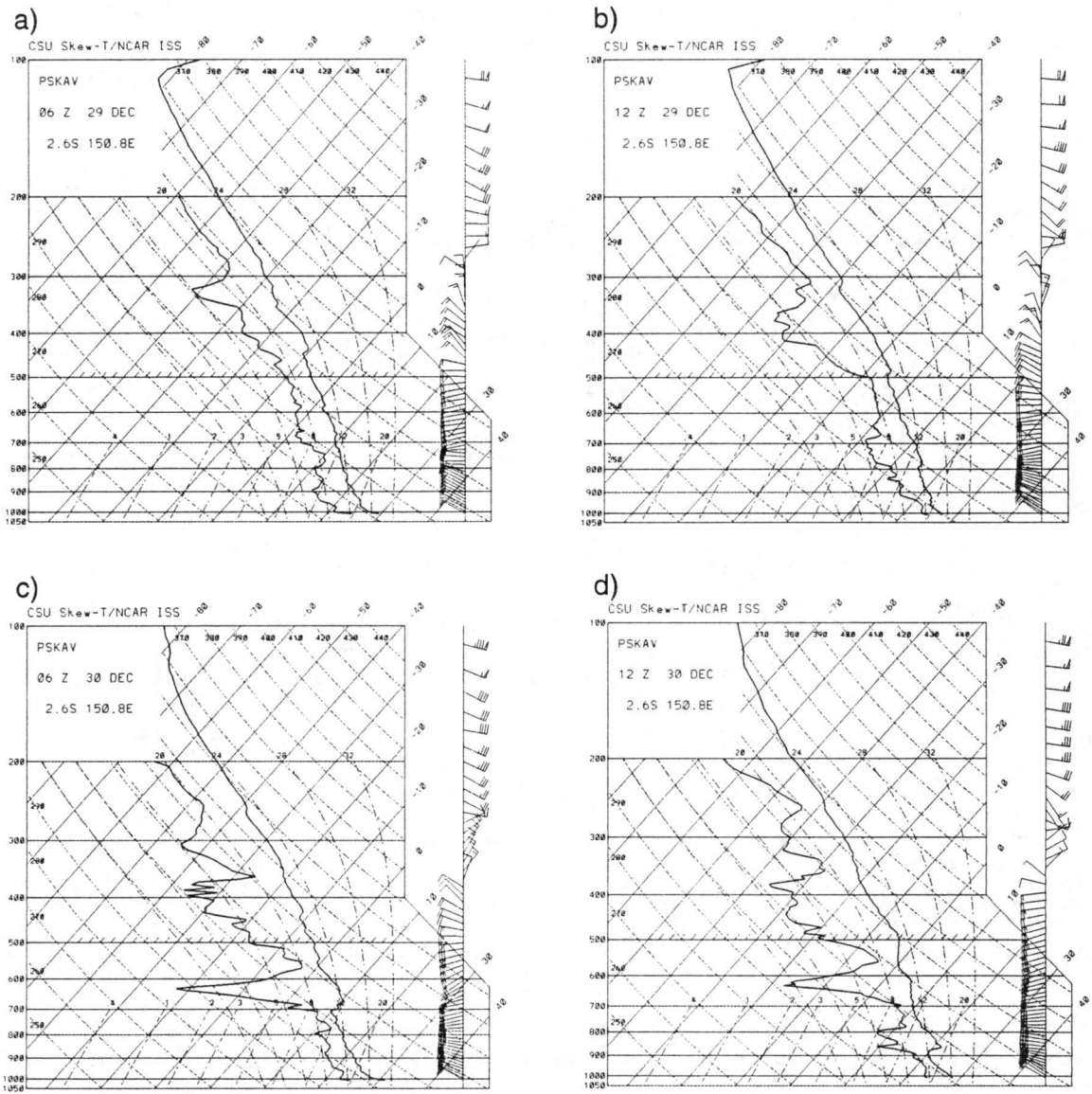


Figure 4.15: Skew-T diagrams for Kavieng at (a) 0600 UTC 29 December, (b) 1200 UTC 29 December, (c) 0600 UTC 30 December, (d) 1200 UTC 30 December, (e) 1800 UTC 30 December, (f) 0000 UTC 31 December, (g) 1200 UTC 31 December, and (h) 0600 UTC 1 January.

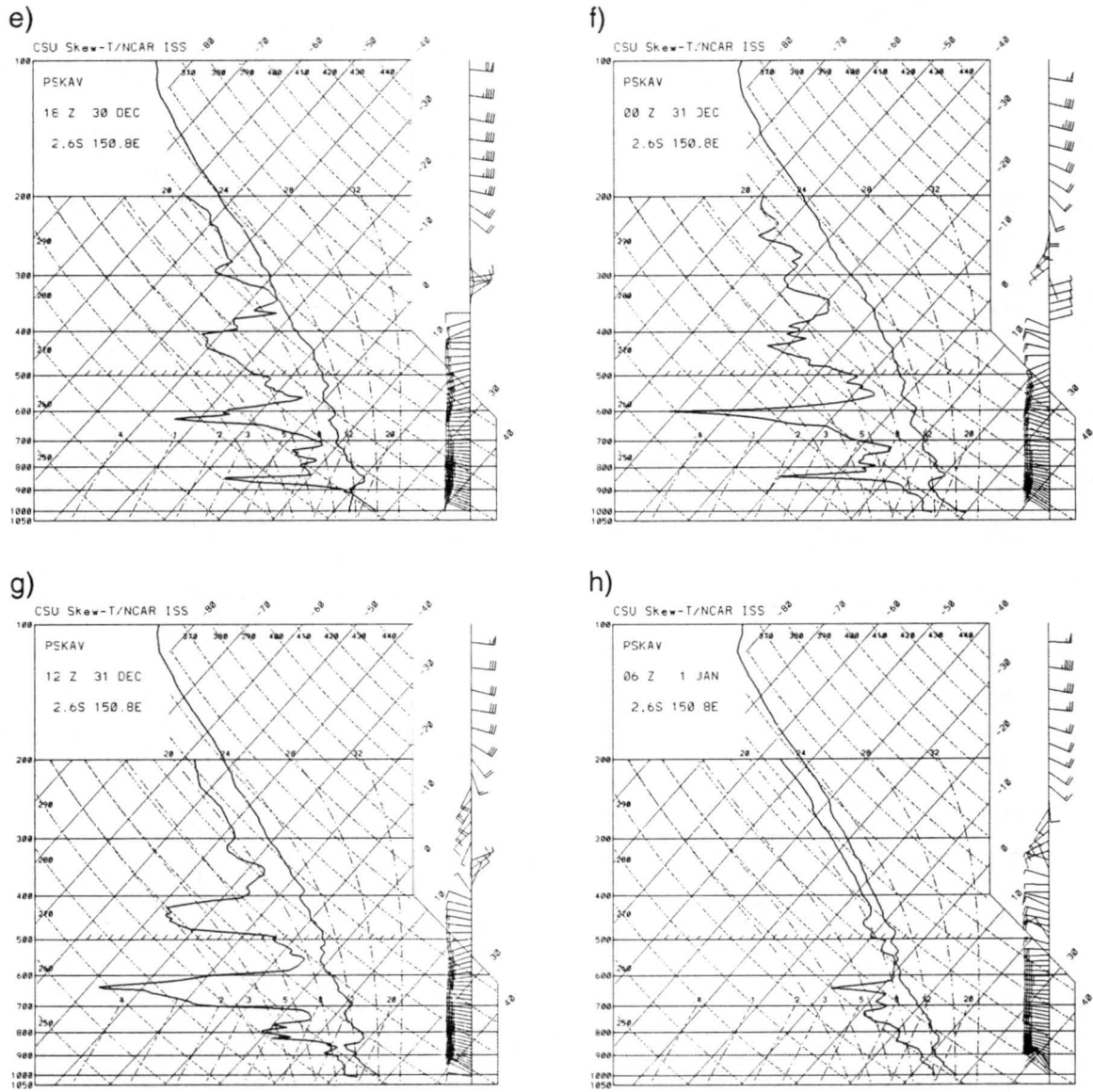


Figure 4.15: Continued.

IOP. The first MJO was observed in early November, the second in late December-early January and the last in late January-early February. The passage of each MJO was characterized by low-level westerlies or “westerly wind bursts” (Gutzler et al. 1993). Johnson et al. (1993) found a connection between the low-level westerlies and the intensification of upper-level easterlies (near 100 mb) during the second and third MJOs observed during the IOP.

The westerlies below 400 mb acted to advect drier air as shown by the series of east-west cross-sections of average relative humidity from 10°S to 10°N in Figs. 4.16a-d. On the 0000 UTC 28 December and 0000 UTC 29 December cross-sections (Figs. 4.16a-b), a strong gradient of average relative humidity (on the order of 30%) could be found near 164°E. By 0000 UTC 30 December (Fig. 4.16c), the strong gradient in average relative humidity had shifted to the east near 170°E. Generally dry conditions ($RH \leq 45\%$) above the CBL west of this boundary were being advected by westerly flow. By 0000 UTC 31 December (Fig. 4.16d), low average relative humidities above the CBL were depicted across nearly the entire IFA. A local maximum in RH is noted near the freezing level (~ 550 mb) west of 155°E on both the 30 December (Fig. 4.16c) and 31 December (Fig. 4.16d) cross-sections.

A series of north-south cross-sections of relative humidity from 10°S to 10°N representing averages of gridded data from 140°E to 160°E are shown in Figs. 4.17a-d. These north-south cross-sections are different from those used in case I as they have been expanded westward to 140°E to include the soundings taken at Manus and Madang. The 0000 UTC 29 December cross-section (Fig. 4.17a) shows high relative humidity values ($\geq 65\%$) through 500 mb in areas south of the equator. By 0000 UTC 30 December (Fig. 4.17b), a local maximum of relative humidity ($\geq 50\%$), centered at the freezing level in the Southern Hemisphere was bounded aloft and below by very dry conditions. This regime of moist air near the 0°C level surrounded by very dry conditions aloft and below persisted for the next two days (Figs. 4.17c-d).

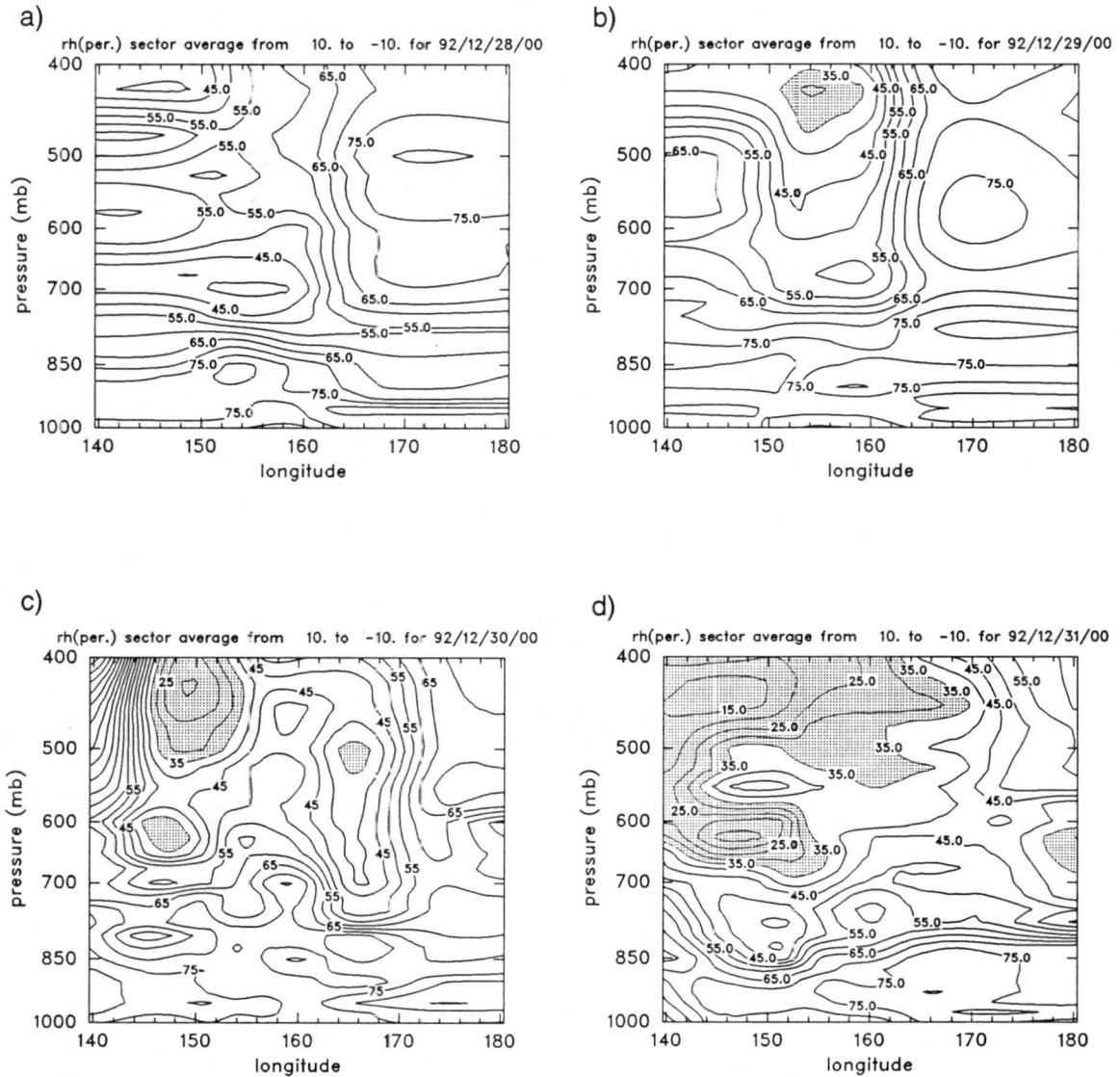


Figure 4.16: East-west relative humidity cross-sections of LSA from 140°E to 180°E averaged from 10°S to 10°N at (a) 0000 UTC 28 December, (b) 0000 UTC 29 December, (c) 0000 UTC 30 December, and (d) 0000 UTC 31 December. Contours of relative humidity are every 5%. Values $\leq 35\%$ are shaded.

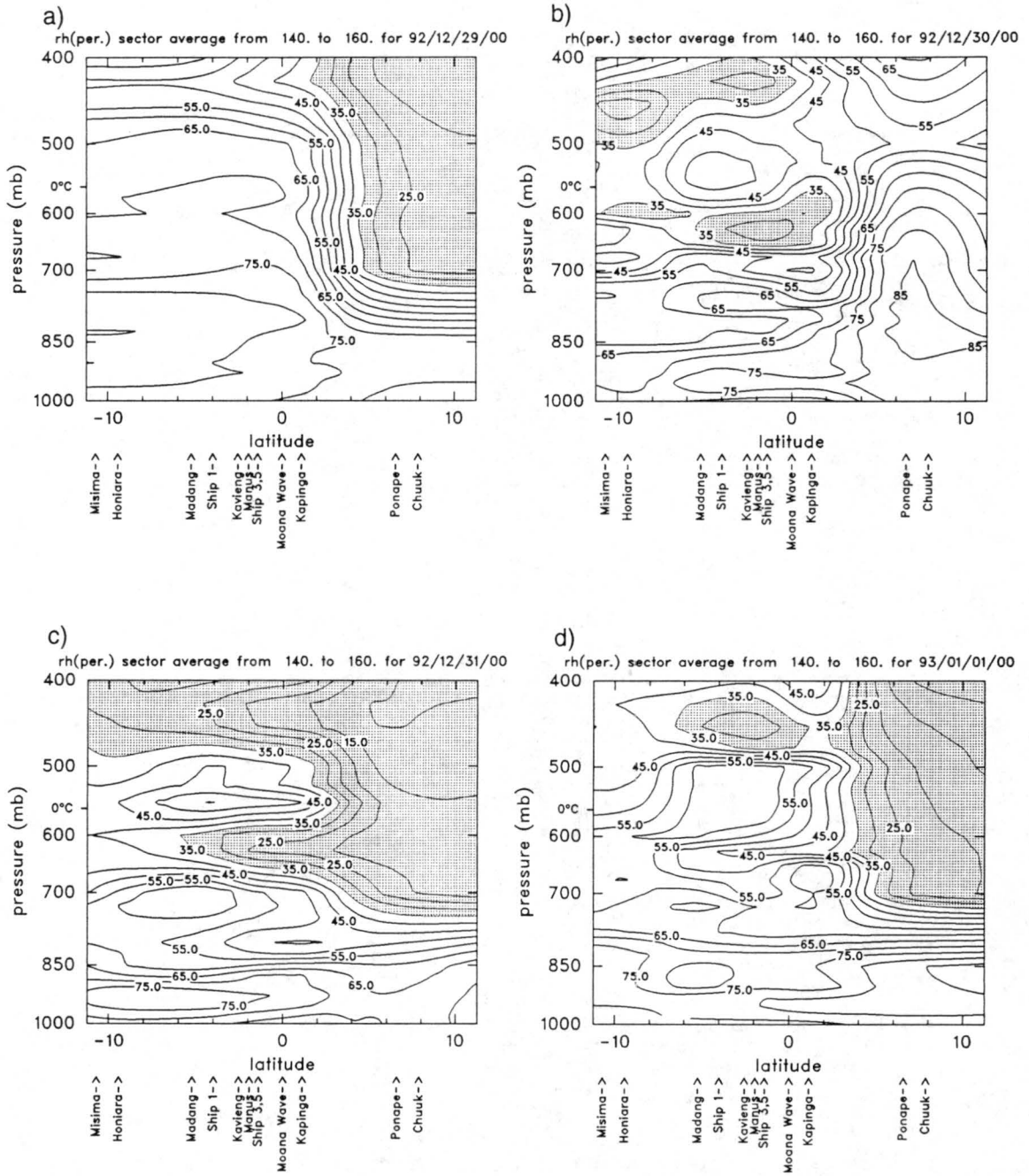


Figure 4.17: North-south relative humidity cross-sections of LSA from 10°S to 10°N average from 140°E to 160°E at (a) 0000 UTC 29 December, (b) 0000 UTC 30 December, (c) 0000 UTC 31 December, and (d) 0000 UTC 1 January. Contours of relative humidity are every 5%. Values $\leq 35\%$ are shaded.

4.3 Case III - 0000 UTC 2 February 1993 to 0000 UTC 5 February 1993

The third extended period of mid-tropospheric stable layers and moisture inversions studied were observed between 0000 UTC 2 February and 0000 UTC 5 February 1993. Similar to case II, this case occurred during a westerly-burst event. Pronounced q reversals and stable layers near the melting level were observed first at Kapingamarangi, then at Nauru 24 hours later.

4.3.1 Satellite Overview

The satellite sequence (Figs. 4.18a-d) shows the development of convection from 1-4 February. At 1745 UTC 1 February (Fig. 4.18a), the most dominant feature was a MCS located east of the OSA and south of the Equator where cloud tops were colder than -80°C across a large area. A tongue of dry air had entered the western portion of the OSA near the equator at this time. Some moderate convection was observed north of Kapingamarangi in a band between 3 and 5°N .

The large MCS in the Southern Hemisphere maintained its size and position through 1745 UTC 2 February 1993 (Fig. 4.18b). Convection over the IFA and central OSA was replaced by an eastward moving tongue of dry air. Conditions north and west of the sounding arrays were free of any deep convection.

Over the course of the next day, the suppressed conditions spread even farther to the east. This latitudinally oriented band of drier air had reached the eastern boundary of the OSA by 1745 UTC 3 February (Fig. 4.18c). The area of deep convection east of the OSA and south of the equator had dissipated. Two bands of convergence had formed a double-ITCZ structure similar to that observed in Case I. The Northern Hemisphere band was centered on 3°N while the Southern Hemisphere band was observed between 5 and 10°S . At 1745 UTC 4 February (Fig. 4.18d), all of the ISS sites remained away from deep convection and the ITCZ bands laid generally in the same position as 24 hours prior.

4.3.2 Thermodynamic and Kinematic Structure

Figure 4.19 shows a four-day time series of specific humidity profiles taken at Nauru

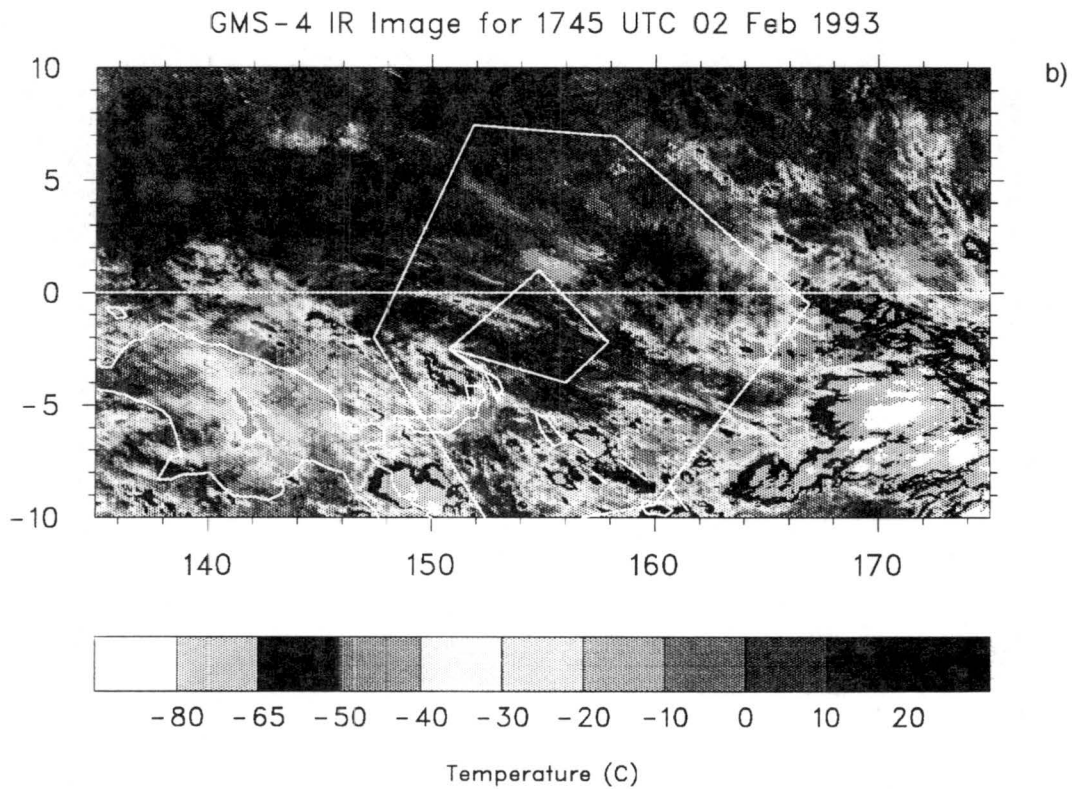
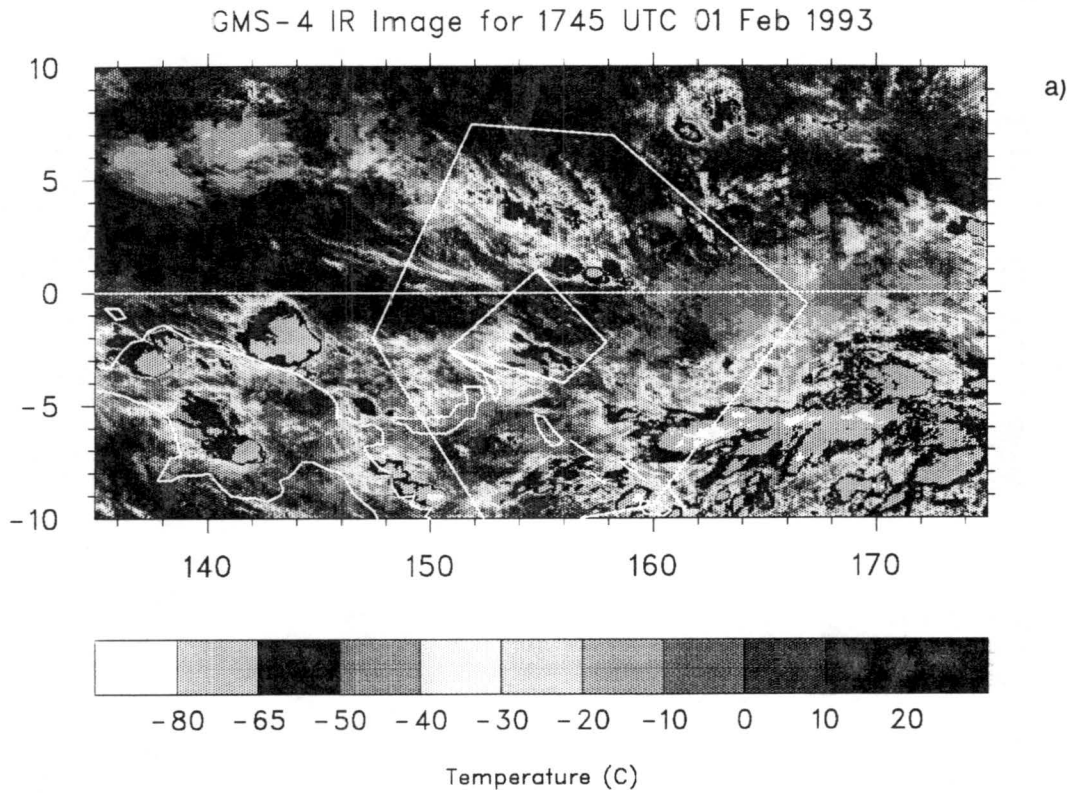
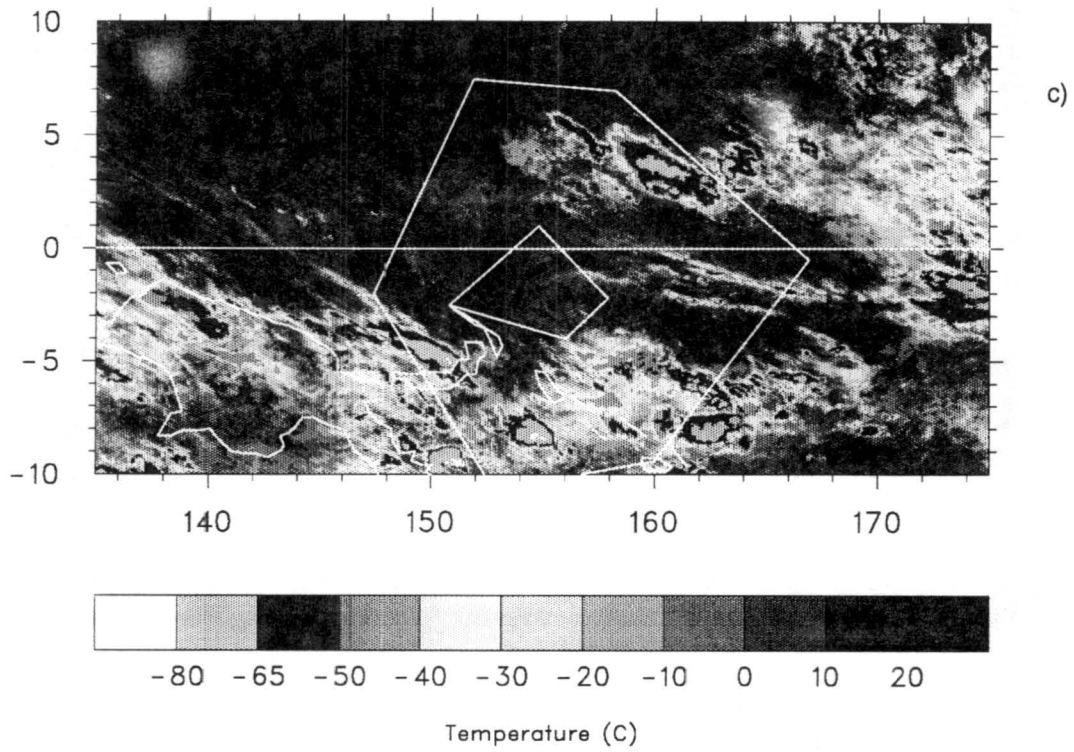


Figure 4.18: GMS-IR satellite images of the TOGA COARE region at (a) 1745 UTC 1 February, (b) 1745 UTC 2 February, (c) 1745 UTC 3 February, and (d) 1745 UTC 4 February 1993.

GMS-4 IR Image for 1745 UTC 03 Feb 1993



GMS-4 IR Image for 1745 UTC 04 Feb 1993

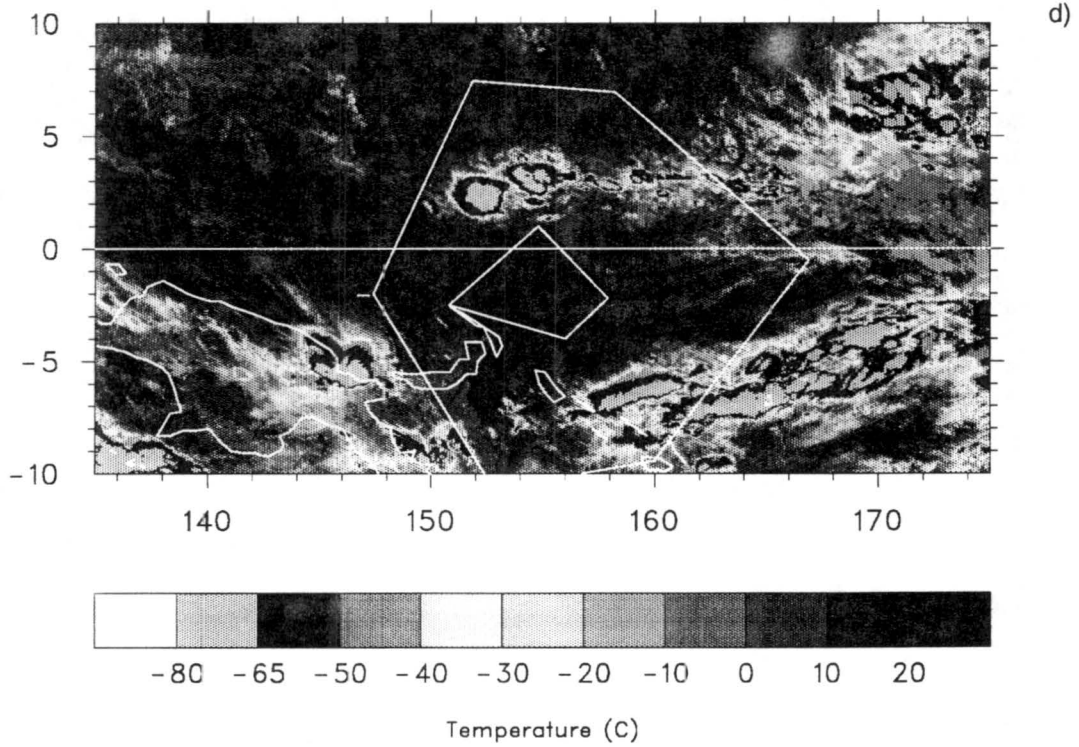


Figure 4.18: Continued.

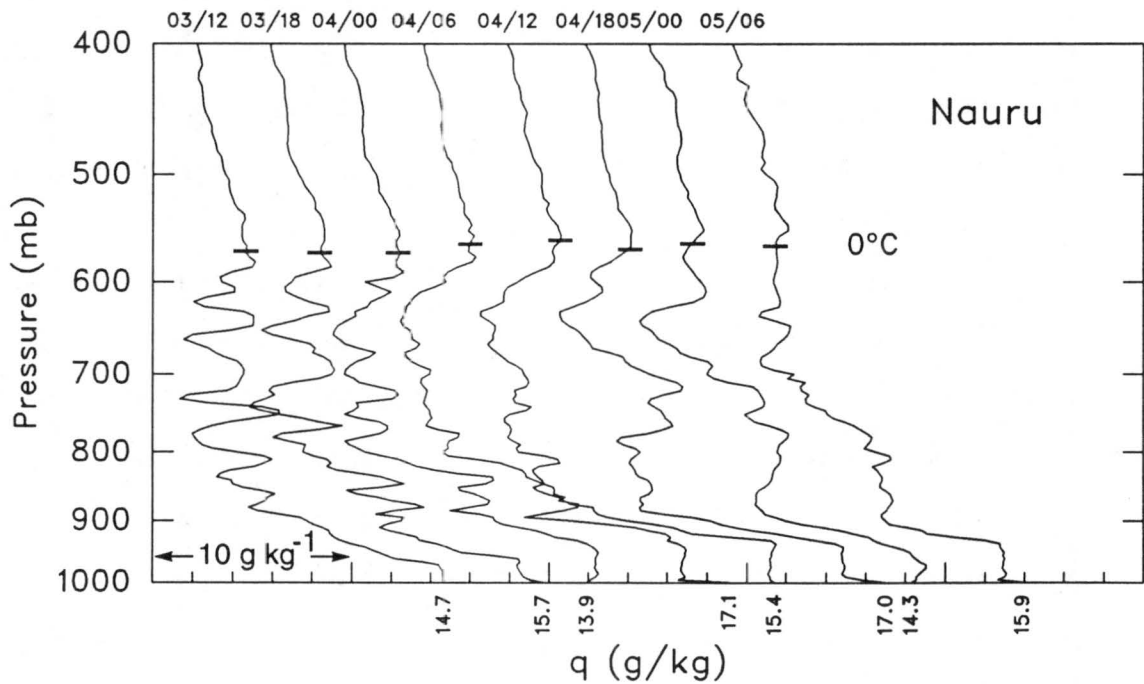
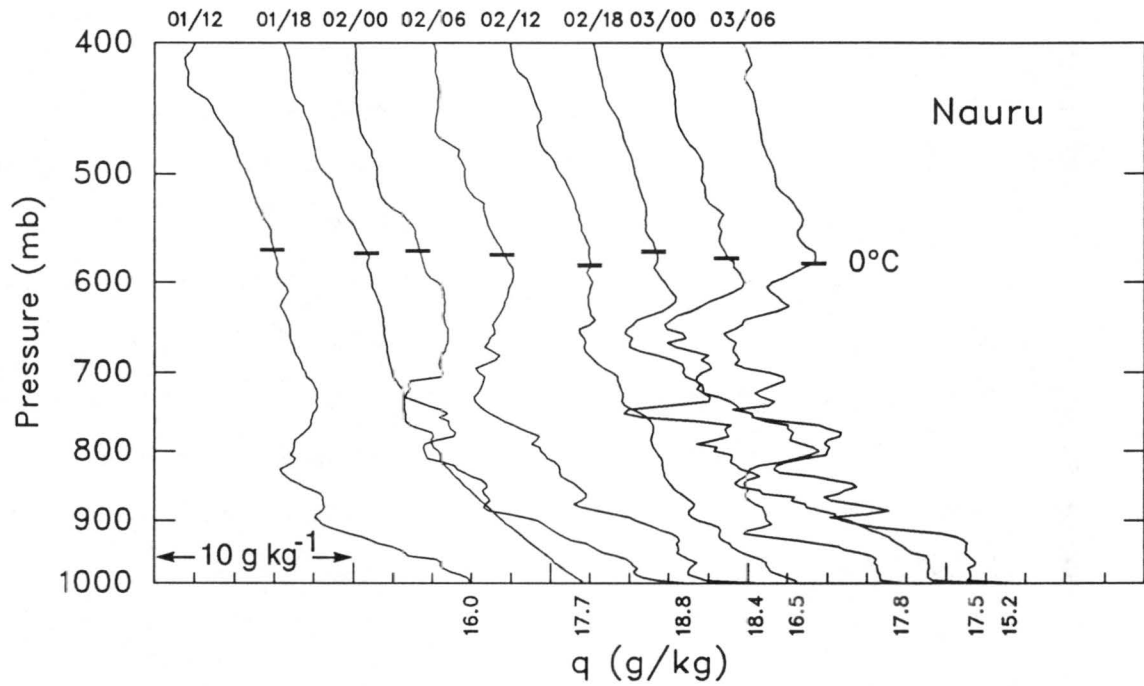


Figure 4.19: Specific humidity time series for Nauru from 1200 UTC 1 February to 0600 UTC 5 February 1993. The scale for each curve is shifted to the right by 4 g kg^{-1} to avoid overlap. Day/GMT hour is indicated along the top.

every six hours from 1200 UTC 1 February to 0600 UTC 5 February. At 1800 UTC 1 February and prior to this time, soundings at Nauru were moist through the entire troposphere. By 0000 UTC 2 February there was evidence of a dry layer near 750 mb and above the freezing level near 550 mb. Six hours later there was a local maximum of specific humidity near 600 mb or just below the melting level.

The sounding at 1200 UTC 2 February did not show a well-defined local maximum in q near the 0°C level. The close proximity of deep convection at 1200 UTC moistened the sounding and obscured the mid-tropospheric inflection in q , however, a slight reversal in q remained. A more pronounced q inflection was observed again by 1800 UTC 2 February near the 600 mb level. This pronounced inflection in specific humidity continued through 0000 UTC 5 February.

Specific humidity profiles for the same four-day period at Kapingamarangi are shown in Fig. 4.20. The onset of the inflection in mid-tropospheric humidity values was about 24 hours prior to that at Nauru. This was likely the result of the eastward progression of dry air depicted in the satellite sequence (Fig. 4.18) since Kapingamarangi is located about 1200 km to the west of Nauru. Winds in the lower troposphere were on the order of 15 m s^{-1} during this period. Wind speeds of this magnitude would be capable of advecting an air mass across distances as large as 1200 km in 24 hours. The moisture inversion persisted at Kapingamarangi through 0000 UTC 4 February and was observed to descend during the later stages of this period.

East-west cross-sections of zonal wind speed averaged from 10°S to 10°N are shown in Figs. 4.21a-d. Wind speeds are in m s^{-1} and positive values are westerlies. For the entire three-day period, from 0000 UTC 2 February to 0000 UTC 5 February, westerlies were generally observed below 550 mb between 150°E and 170°E . Easterlies were found above 550 mb for the same longitudes. In this case, as was the situation in Case II, the westerlies were a source of drier air. Conditions to the east of the OSA were particularly moist in association with the MCS there. Therefore, easterly flow was generally a source of higher relative humidities due to mid- and upper-level water vapor from the MCS.

A series east-west cross-sections of relative humidity from 140°E to 180°E , representing average values from 10°S to 10°N , is shown in Figs. 4.22a-d. Average relative humidity

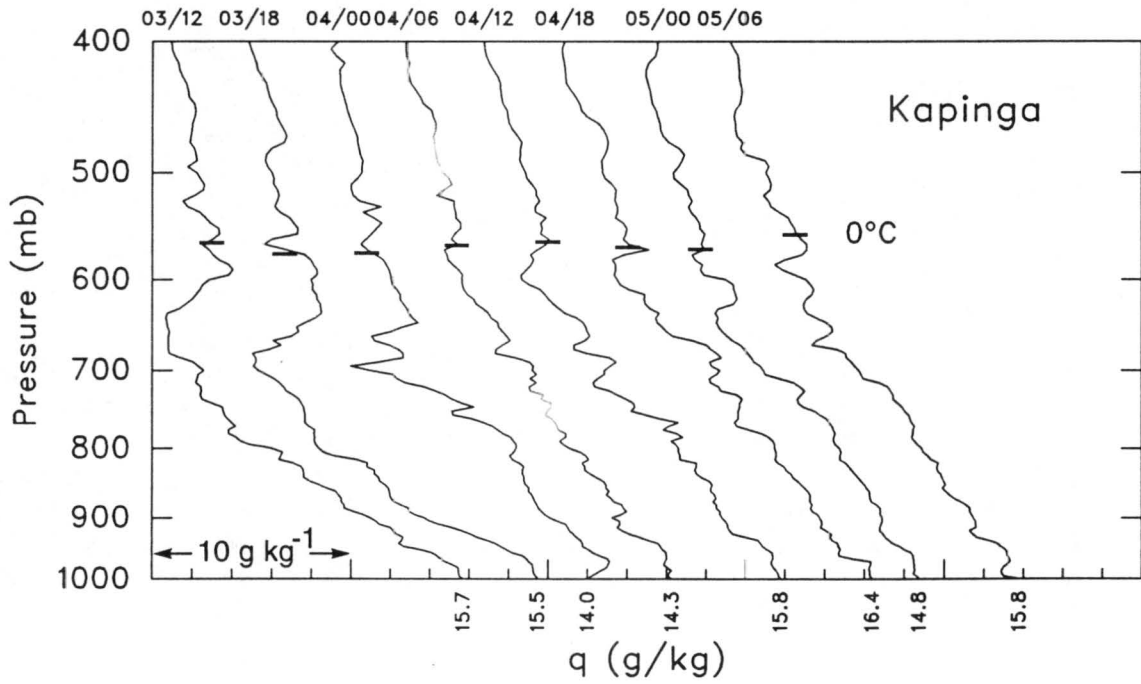
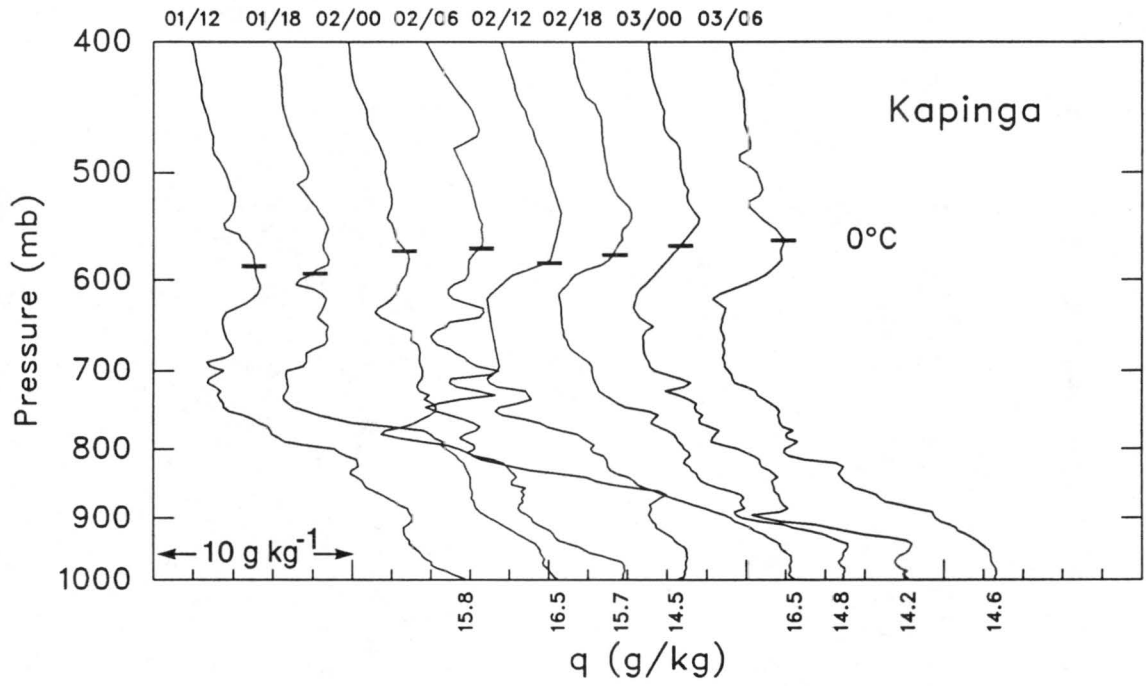


Figure 4.20: Same as in Fig. 4.19, except for Kapingamarangi.

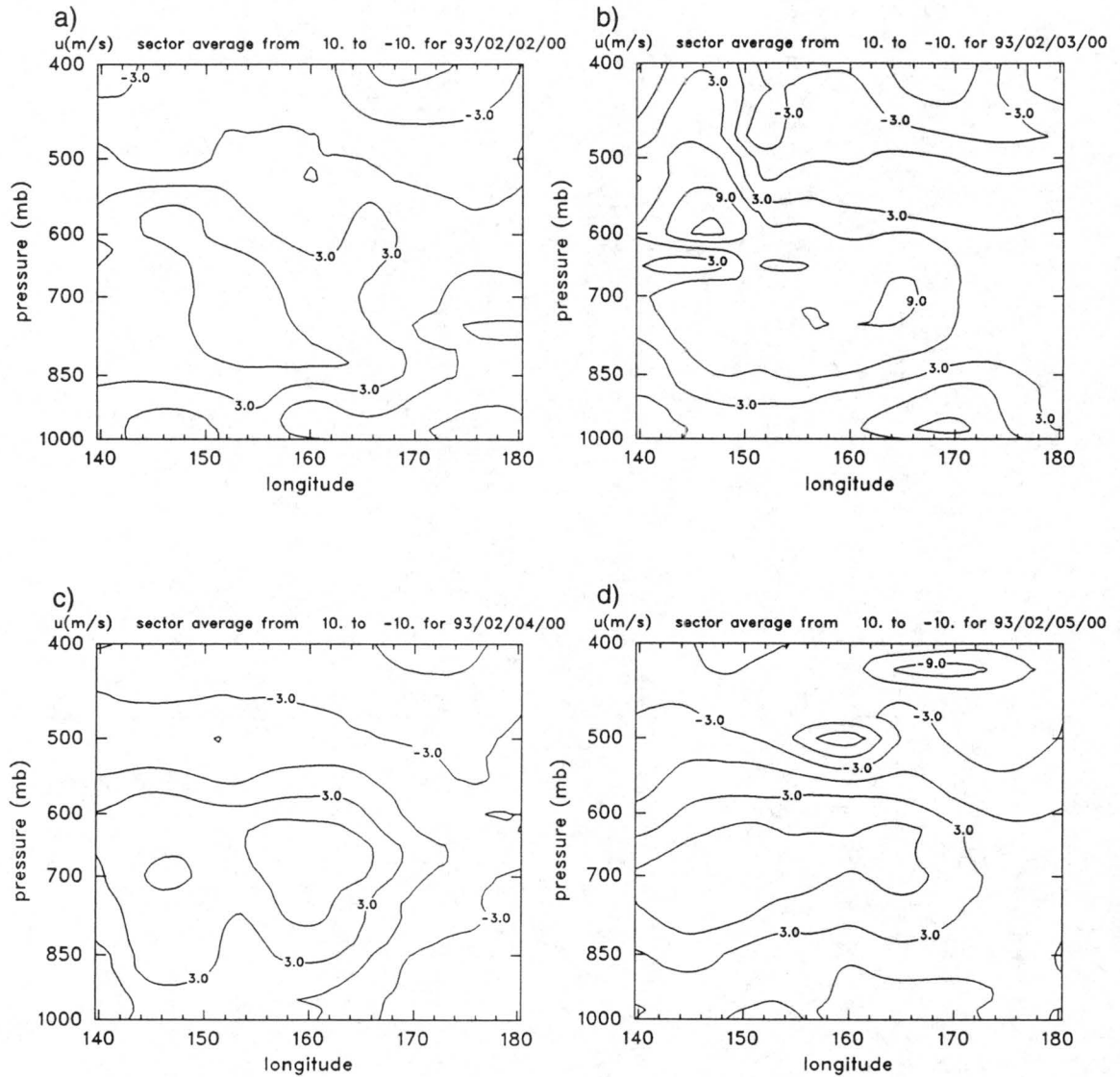


Figure 4.21: East-west zonal wind cross-sections of LSA from 140°E to 180°E averaged from 10°S to 10°N at (a) 0000 UTC 2 February, (b) 0000 UTC 3 February, (c) 0000 UTC 4 February, and (d) 0000 UTC 5 February. Contours are every 3 m s⁻¹.

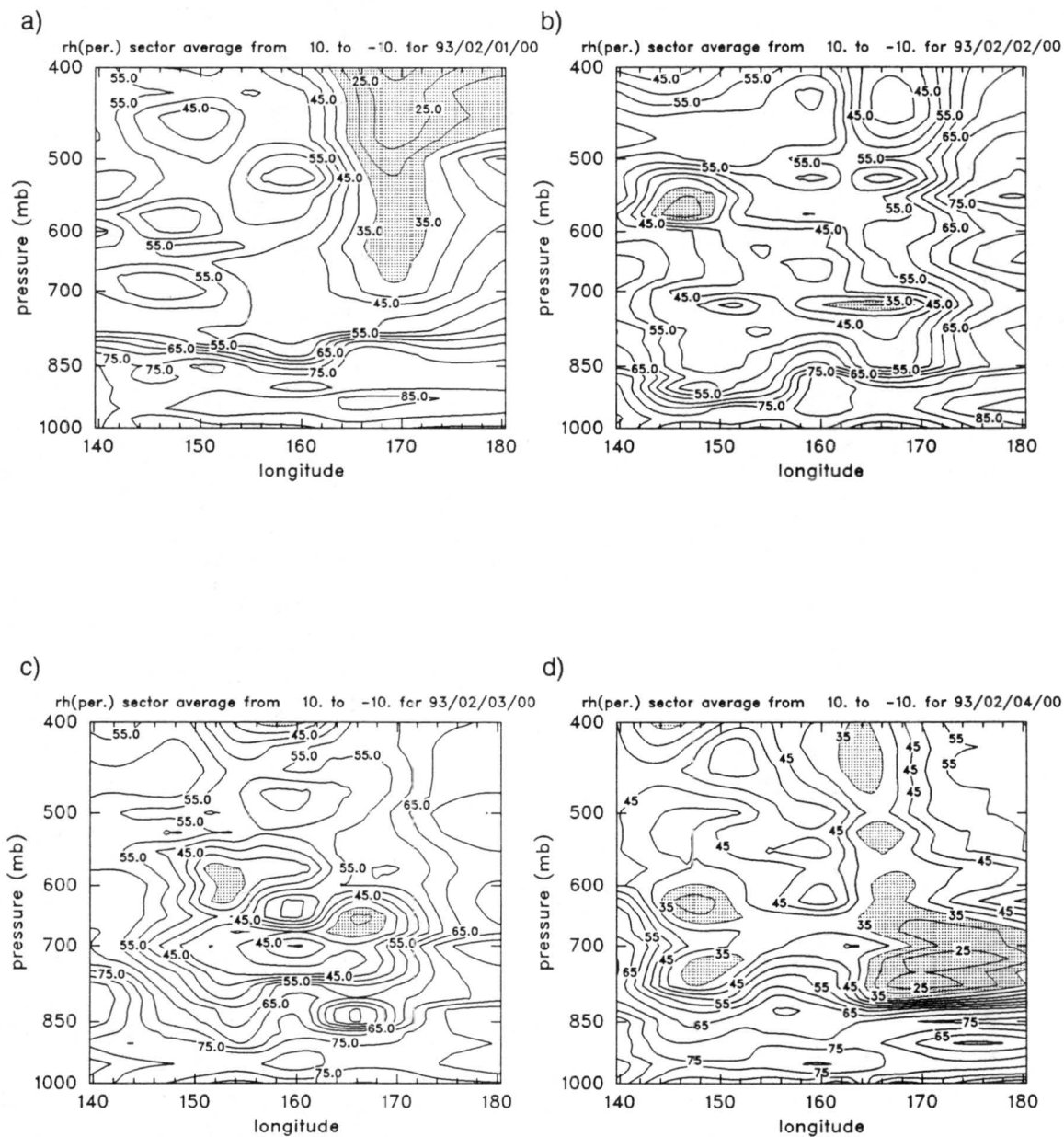


Figure 4.22: East-west relative humidity cross-sections of LSA from 140°E to 180°E averaged from 10°S to 10°N at (a) 0000 UTC 1 February, (b) 0000 UTC 2 February, (c) 0000 UTC 3 February, and (d) 0000 UTC 4 February. Contours of relative humidity are every 5%. Values $\leq 35\%$ are shaded.

values between 800 and 550 mb were observed to decrease with time from west to east while average humidity values above 550 mb were observed to increase with time from east to west. Average relative humidity values in the CBL remained fairly constant through the period.

A series of Skew-T diagrams for Nauru (Figs. 4.23a-d) from 1200 UTC 1 February

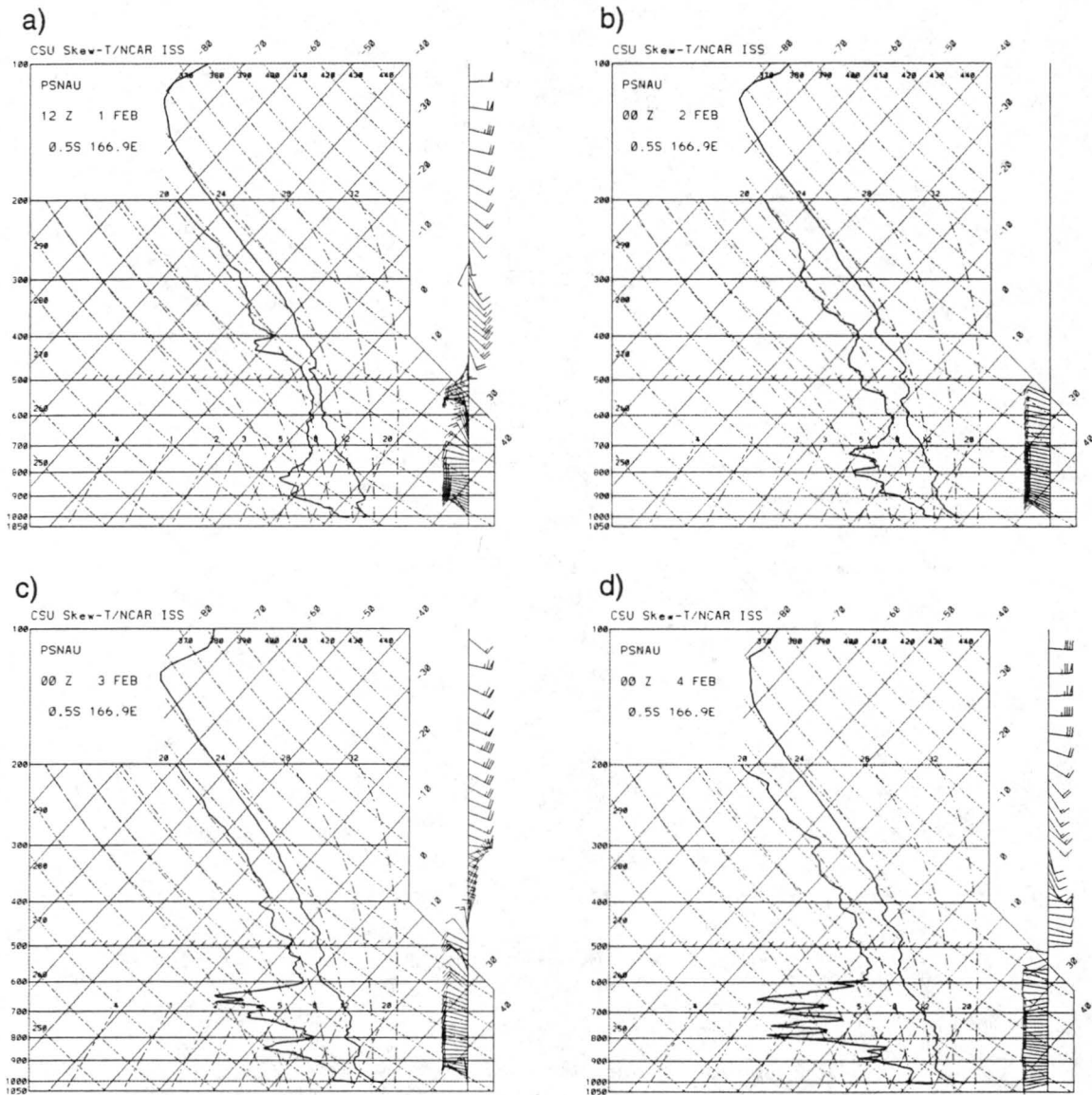


Figure 4.23: Skew-T diagrams for Nauru at (a) 1200 UTC 1 February, (b) 0000 UTC 2 February, (c) 0000 UTC 3 February, and (d) 0000 UTC 4 February.

through 0000 UTC 4 February reflects the evolution of thermodynamic and kinematic features. Except for a dry lower troposphere (below 700 mb), the 1200 UTC 1 February

sounding (Fig. 4.23a) was rather moist. West to northwest flow at 7.5 to 15 m s⁻¹ was predominant below 500 mb and southeast to easterly flow was observed above 500 mb. Strong easterly flow aloft and westerly flow at low-levels is a signature of a MJO event. The third of three MJO's observed during the IOP crossed the sounding arrays in late January - early February (Gutzler et al. 1993).

By 0000 UTC 2 February (Fig. 4.23b), an isothermal layer near the melting level had developed. The atmosphere remained dry below 600 mb. A shallow, moist layer was evident near the 0°C level. The top of the moist layer coincided with the base of the isothermal layer. Winds were westerly through 500 mb and wind data above this level were missing.

Twenty-four hours later (Fig. 4.23c), an isothermal layer could be found just above the 0°C level. A similar isothermal layer, with a base near 800 mb, may have been the result of tradewind cumulus clouds. The base of each of these stable layers marked the locations of local maxima in humidity. The resulting q inversions were depicted in Fig. 4.19. The low-level q inflection was again consistent with those observed by Betts and Albrecht (1987). Winds below 500 mb remained westerly and above 300 mb strong easterlies persisted. Between 500 and 300 mb, a transition layer was observed as winds backed with height.

Few changes were observed 24 hours later at 0000 UTC 4 February (Fig. 4.23d). Conditions below 600 mb were generally dry except for a shallow layer of higher humidity which coincided with the top of the CBL. Higher concentrations of mid- and upper-level water vapor, likely the outflow from the MCS south and east of Nauru, resulted in a moist sounding above 600 mb. This pattern differed from the first two cases when very dry conditions were observed above the freezing level.

North-south cross-sections of relative humidity from 10°S to 10°N averaged from 150°E to 170°E to include the eastern portions of the OSA are shown in Figs. 4.24a-d. At 0000 UTC 2 February (Fig. 4.24a), low relative humidity values above 700 mb in the Northern Hemisphere were separated by the equator from higher relative humidity values in the Southern Hemisphere. The higher relative humidity values were influenced by the large MCS south of the equator.

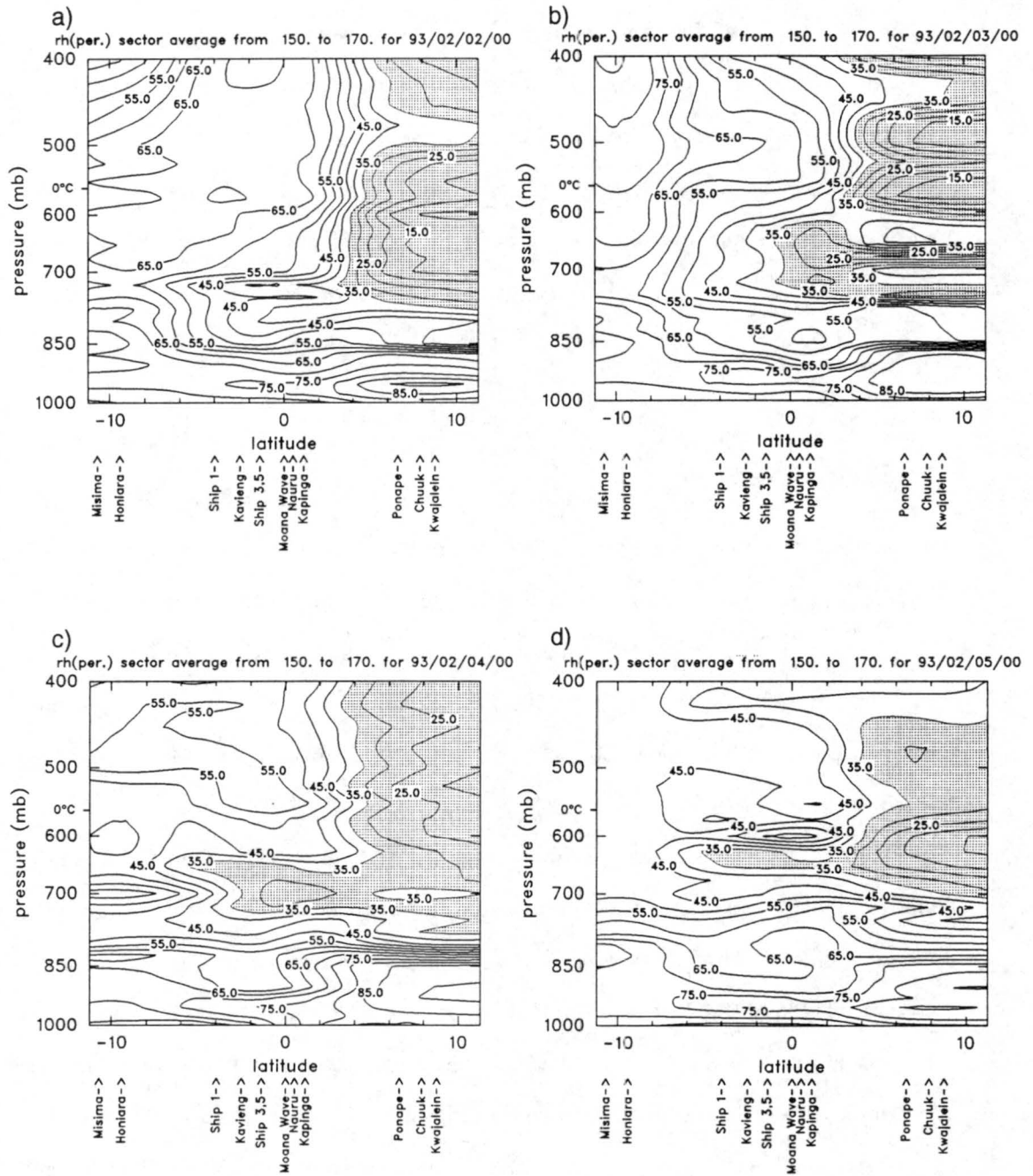


Figure 4.24: North-south relative humidity cross-sections of LSA from 10°S to 10°N averaged from 150°E to 170°E at (a) 0000 UTC 2 February, (b) 0000 UTC 3 February, (c) 0000 UTC 4 February, and (d) 0000 UTC 5 February. Contours of relative humidity are every 5%. Values $\leq 35\%$ are shaded.

By 0000 UTC 3 February (Fig. 4.24b), a very dry layer (RH values $\leq 35\%$) centered near 700 mb was observed from the equator northward. A local maxima of relative humidity appeared near 550 mb over a large area. Twenty-four hours later, at 0000 UTC 4 February (Fig. 4.24c), the dry regime near 700 mb (RH values $\leq 35\%$) reached as far south as 4°S . The local maximum of humidity near the melting level persisted over a large horizontal domain near the equator.

The 0000 UTC 5 February cross-section of relative humidity (Fig. 4.24d) shows a shallow, moist layer across the equator at 600 mb. The cross-section depicts significantly drier air in a shallow layer immediately below 600 mb. The lower troposphere remained moist. The mid-tropospheric features depicted above resulted in a reversal in q .

4.4 Synthesis of Results and Interpretation

The preceding three cases have illustrated that temperature and moisture inversions occur simultaneously (or nearly so) over large domains for extended periods of time. This section will synthesize the observations from each case into average or typical structures. Numerous similarities between the cases were found.

4.4.1 Typical Skew-T Profiles

Typical profiles of temperature, dewpoint temperature, and wind are provided on a Skew-T diagram in Fig. 4.25. The average profiles serve as a consensus of soundings observed at several locations during each case, but the values plotted have not been objectively computed. The temperature profile was very similar for each case, so only one has been plotted.

In Case I, the soundings were generally moist prior to the rapid onset of a mid-tropospheric dry regime which began near 550 mb. The dry air was characterized by an isothermal layer at the melting level. A temperature inversion also frequently occurred in the lower troposphere with a base near 800 mb. East to northeasterly flow accompanied the mid-tropospheric dry intrusion. After deepening with time, dry air in the middle troposphere was separated by a shallow, moist layer just below the temperature inversion

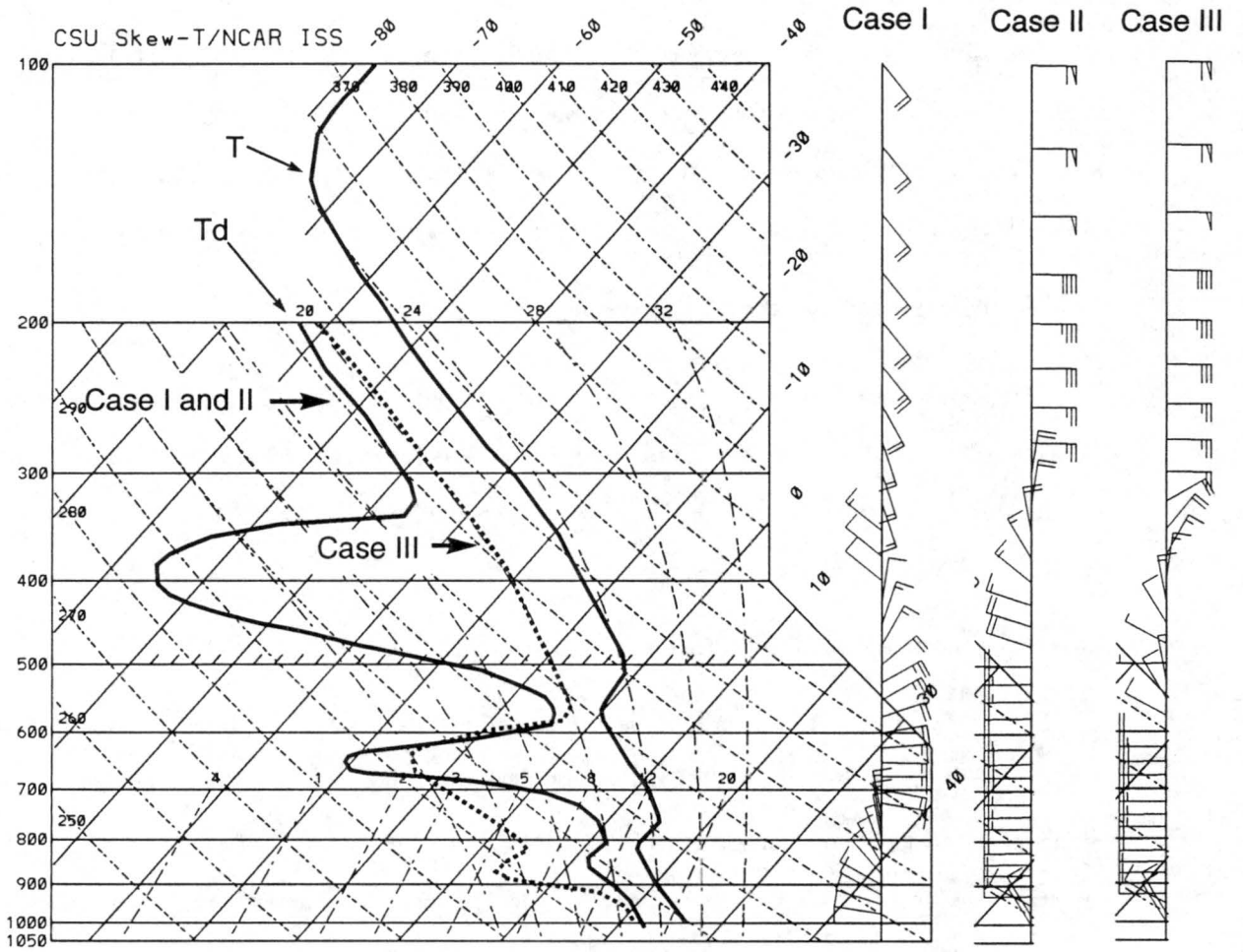


Figure 4.25: Typical Skew-T profiles for Case I, Case II, and Case III.

at the 0°C level. As in Case I, rather moist soundings were found prior to the rapid onset of dry conditions in the midtroposphere during Case II.

The primary difference between Case I and Case II was the wind direction. In Case II, winds were westerly from 950 through 400 mb in association with the second of three MJO's to cross the TOGA COARE sounding array during the IOP. Case I winds were westerly from the surface through 700 mb where they turned northeast to easterly up to 400 mb. Above 400 mb in Case I, winds were highly variable in speed and direction.

Soundings observed in Case III differed from the previous two cases with respect to conditions above the freezing level. The average dewpoint profile for Case III reflects a moist sounding above the 600 mb level. In the previous two cases, dry conditions resumed above the freezing level. In addition, westerlies associated with the active phase of a MJO were usually present in Case III from the surface to between 600 and 550 mb. Westerlies in Case II, however, were generally observed through the 400 mb level.

4.4.2 Typical Specific Humidity Profiles

The typical specific humidity profiles for each case depicted a q inflection, or reversal in the midtroposphere just below the melting level (Fig. 4.26). For the first two cases, an additional inflection, sometimes two, were observed in the lower troposphere. The position of this lower-level inflection varied, but was commonly seen between 850 and 700 mb. As was discussed earlier, the specific humidity during Case III did not decrease rapidly with height above the freezing level. Consequently, the local maxima in q in the midtroposphere were not as pronounced in Case III. The low-level specific humidity inflections observed in the first two cases were also seen in Case III.

4.4.3 Synoptic Pattern Illustrations

The synoptic pattern depictions shown in Fig. 4.27 are designed to illustrate large-scale features observed during each case. The pattern in Case I (Fig. 4.27a) evolved into a "double-ITCZ" structure separated by conditions which were less convective near the equator. Two bands of deep convection were found along latitudinally oriented convergence lines in each hemisphere. The individual sounding sites analyzed in this case ascended in areas free of deep convection.

Typical Specific Humidity Profiles

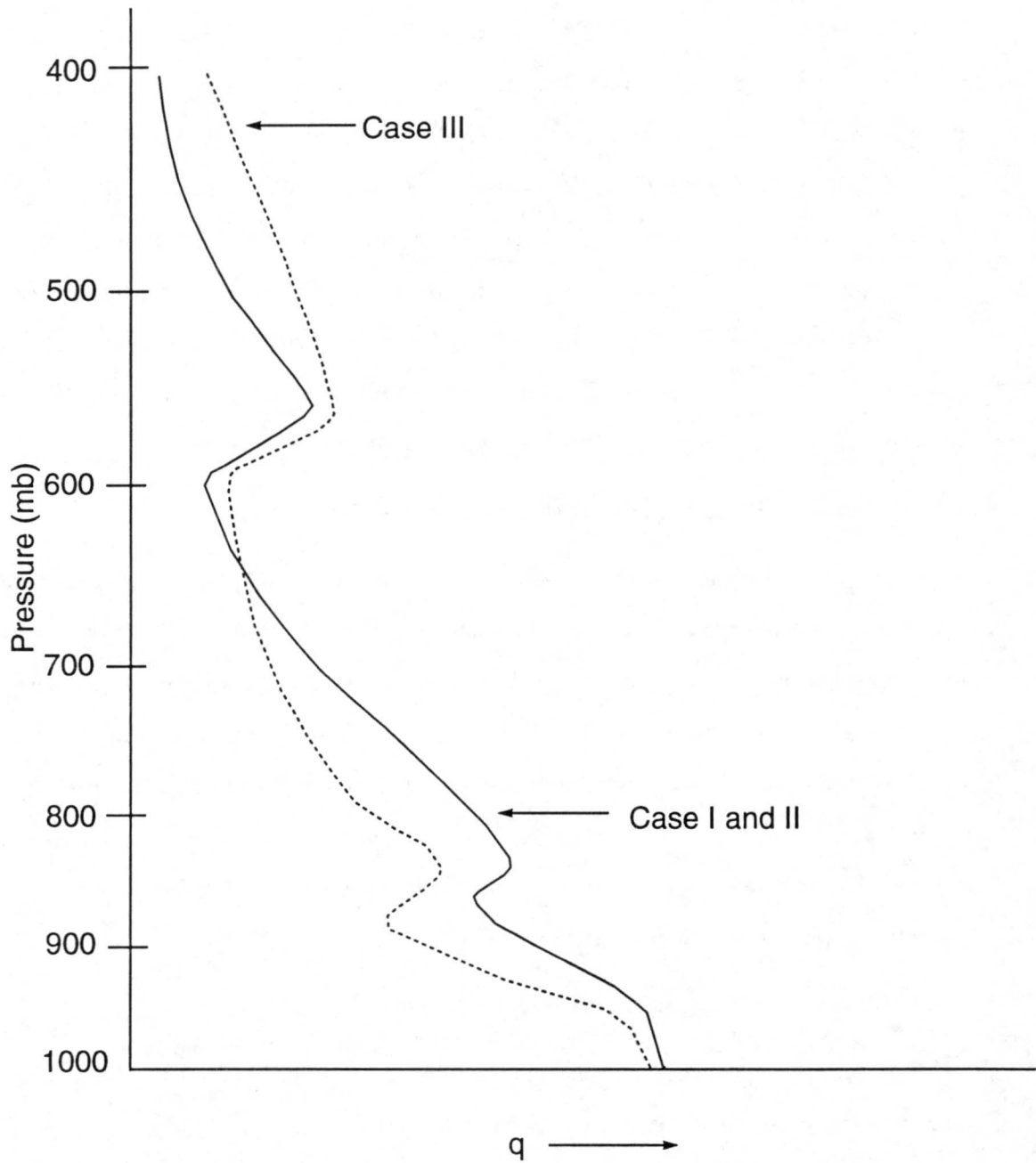


Figure 4.26: Typical specific humidity profiles for Case I, Case II, and Case III.

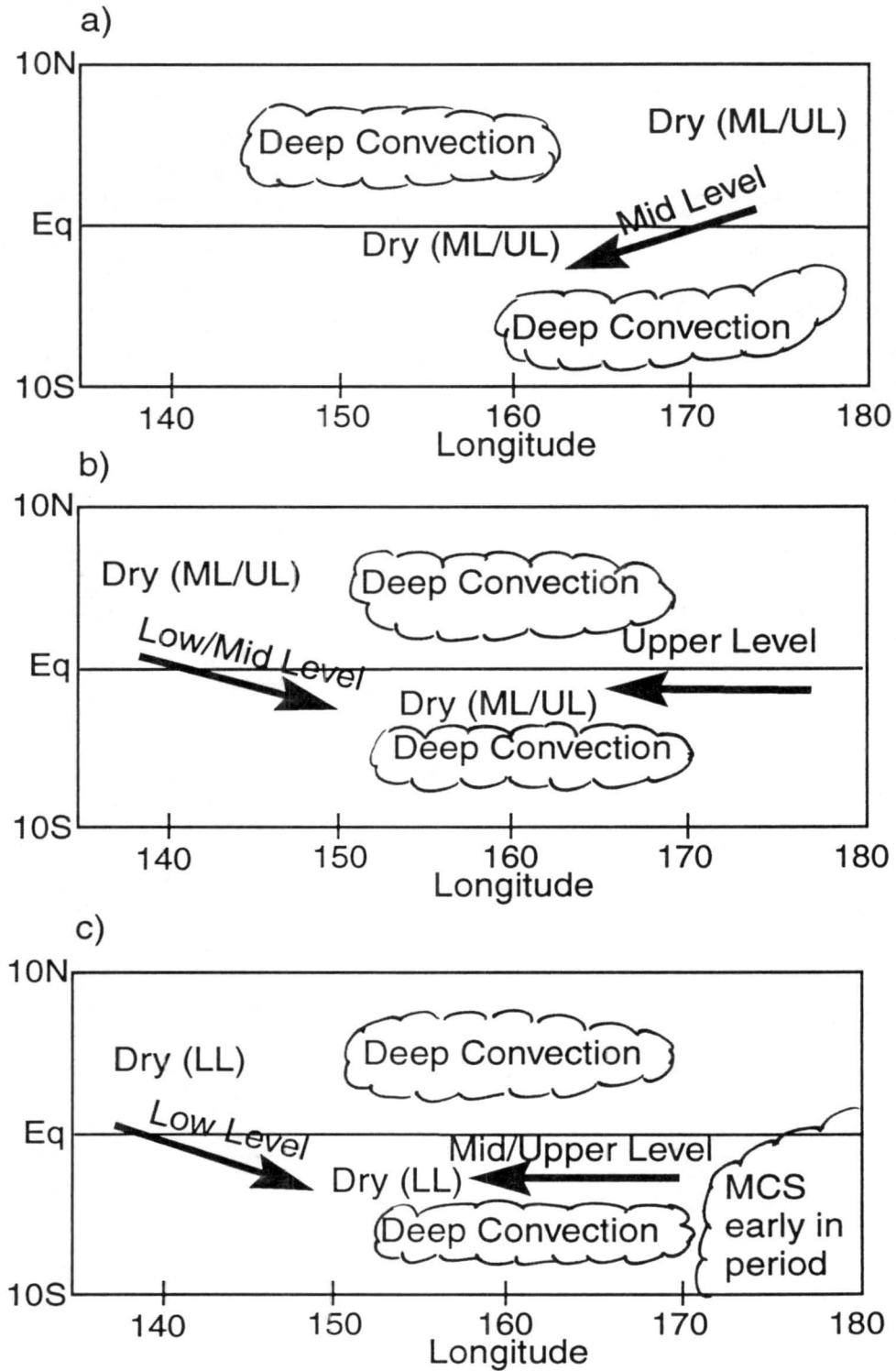


Figure 4.27: Synoptic pattern illustrations for (a) Case I, (b) Case II, and (c) Case III. Dry conditions are characterized by low-level (LL), mid-level (ML), and upper-level (UL).

Case II conditions closely resembled those observed in Case I. Generally less convective conditions along the equator separated bands of deep convection in both the Northern and Southern Hemispheres. Once again, individual soundings examined during this case were launched in regions free of deep clouds or organized convection.

As was the case in the previous periods, the "double-ITCZ" structure was also observed in Case III. In addition, a large MCS persisted in the Southern Hemisphere just east of the OSA. Water vapor outflow from the MCS acted to moisten the mid- and upper-levels of soundings examined in Case III.

Chapter 5

SUMMARY STATISTICS

Recurring moisture and temperature inversions (or stable layers) were common enough to be evidenced in station averages computed for the entire IOP. This chapter will first present station mean profiles of relative humidity and $d\theta/dp$ for Manus, Kavieng, Kapingamarangi, and Nauru. Specific humidity and temperature inversion locations for the entire IOP have been collected and these distributions will be presented for each station. Finally, conserved variable diagrams will be used to summarize microphysical processes observed during the IOP.

5.1 IOP Averages

A total of 479 soundings were scheduled for launch at each of the sites. Although some soundings were terminated early due to icing or bad transmission, only a few soundings were completely missing for each ISS site. Table 5.1 includes the total number of missing soundings at the four stations. Humidity data for the first 24 days of December at Manus were discarded due to instrumentation errors.

ISS Site	Missing Soundings
Manus	33
Kavieng	11
Kapingamarangi	4
Nauru	17

Table 5.1: The number of missing soundings during the IOP.

The mean relative humidity (with respect to liquid water) profiles vs. pressure are shown for Manus, Kavieng, Kapingamarangi, and Nauru in Figs. 5.1a-d. Several features

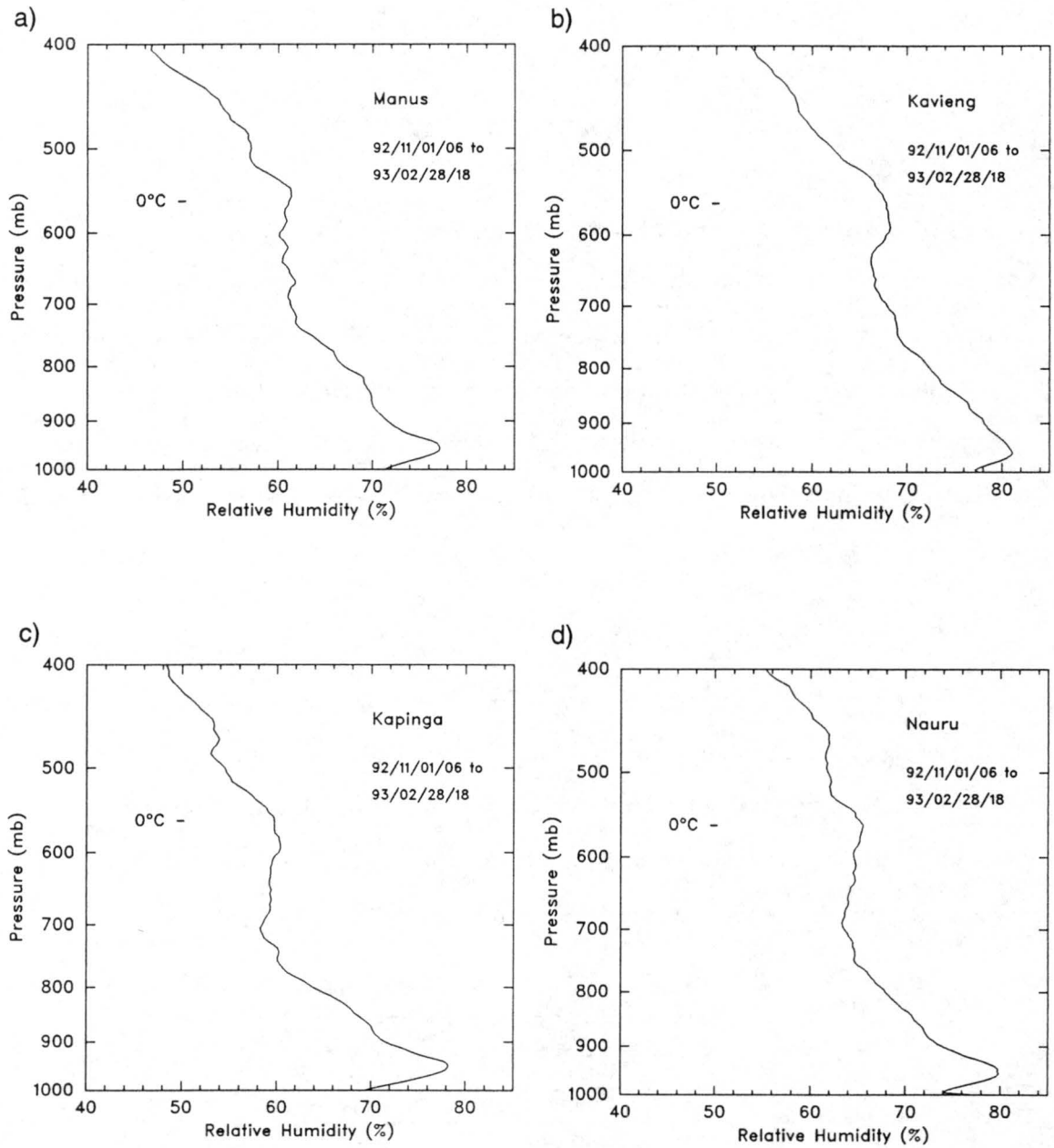


Figure 5.1: Mean relative humidity profiles for four-month IOP at (a) Manus, (b) Kavieng, (c) Kapingamarangi, and (d) Nauru.

are consistent with the tropical study results of Liu et al. (1991) and Gutzler (1993). The maximum relative humidity at each station was observed near 950 mb. Each of the four relative humidity averages displayed a nearly uniform layer in the midtroposphere between 750 and 500 mb. All of the stations, except for Manus (Fig. 5.1a) actually observed a relative humidity reversal in the middle troposphere with maxima between 600 and 550 mb. Similar results were obtained from the nine years of radiosonde data averaged by Liu et al. (1991) and the 16 years of data averaged by Gutzler (1993). Above 500 mb, a linear decrease of relative humidity with pressure was observed at all four locations.

Figures 5.2a-d show the IOP mean stability or $d\theta/dp$ profiles at Manus, Kavieng, Kapingamarangi, and Nauru. Average profiles of temperature and potential temperature vs. pressure were found unusable in the examination of stable layers. However, the first derivative (e.g. $d\theta/dp$) accentuates variations in slope. Since potential temperature generally increases with decreasing pressure, the value of $d\theta/dp$ is almost always negative. Larger negative values correspond to increased stability. The $d\theta/dp$ values plotted were computed over 20 mb depths for each sounding and then averaged for the four-month IOP.

The IOP average $d\theta/dp$ profiles at the four ISS stations exhibit several similar features. From just above the surface (near 980 mb) to 900 mb, the curve is very steep. Between 900 and 800 mb, $d\theta/dp$ continues to decrease reaching local minima between 800 and 750 mb. This corresponds to the frequent low-level temperature inversions referred to in chapter 4. $d\theta/dp$ is roughly constant through a mid-tropospheric layer between 750 and 625 mb, but then begins to decrease sharply again. At each of the four stations, the rapid decrease in $d\theta/dp$ ends near 550 mb, often as a local minimum. The change in slope, or local minimum, near the melting level would correspond to a zone of maximum stability.

5.2 Inversion Location Frequencies

The common occurrence of stable temperature layers and moisture inversions can be seen in the following series of frequency diagrams. Stable temperature layers were determined by computing the lapse rate for each 5 mb layer between 1000 and 400 mb. This temperature lapse rate was compared to a critical lapse rate which was subjectively

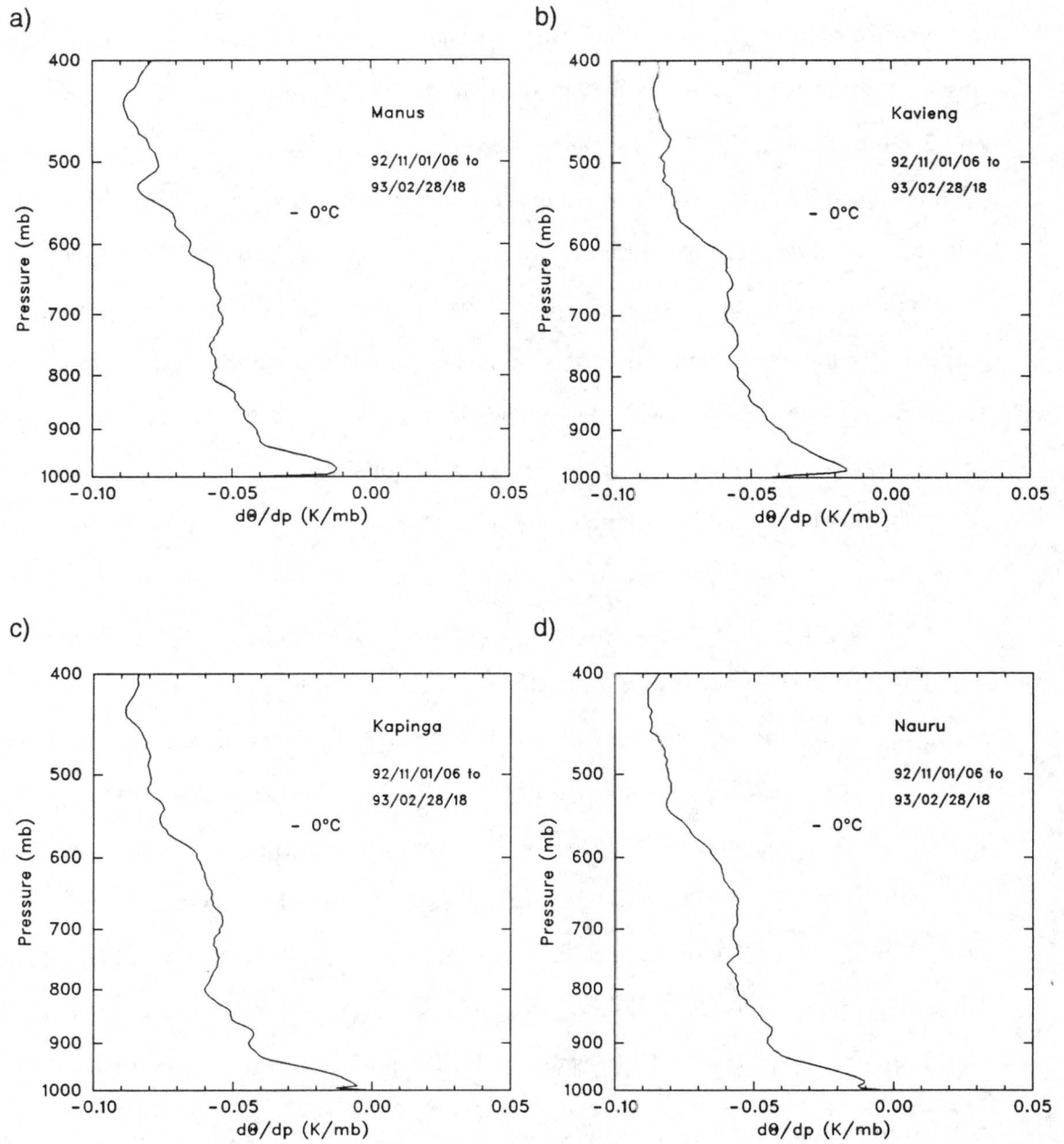


Figure 5.2: Mean $d\theta/dp$ profiles for four-month IOP at (a) Manus, (b) Kavieng, (c) Kapingamarangi, and (d) Nauru.

determined to be $4^{\circ}\text{K km}^{-1}$. All lapse rates less than $4^{\circ}\text{K km}^{-1}$ observed in a layer that was at least a specified depth (e.g. 15, 20, or 25 mb) were considered stable layers. The location of the stable layer was determined by computing the mean pressure of the layer. The same process was followed for determining the locations of specific humidity layers. The critical lapse rate for q is zero (i.e., when dq/dp becomes negative, there is a q inversion).

Figures 5.3a-d show the stable layer frequency distributions (using a 25-mb depth) for the IOP at Manus, Kavieng, Kapingamarangi, and Nauru. Each distribution shows that a maximum number of stable layers - corresponding to tradewind cumulus inversions - occurred between 801 and 850 mb at each location. Between 95 and 120 or nearly one in four of the soundings launched at each of the four stations showed evidence of a tradewind cumulus inversion.

All of the stable layer frequency distributions (Figs. 5.3a-d), except Kapingamarangi, exhibit a secondary frequency maximum in the 501 to 550 mb range. The Kapingamarangi distribution displayed a broad maximum which was spread across three classifications centered on the 501-550 mb bin. Between 15 and 25 or 4 to 5 % of the soundings at each site reflected stable layers in the 501-550 mb range, just above the average melting level of 560 mb. The selection of 25 mb as a depth was rather stringent as many shallower stable layers were observed.

The statistical significance of the secondary frequency maxima in the 501-550 mb range was examined using the following adaptation of the chi-square (χ^2) test. First, the number of degrees of freedom (DOF) were computed from

$$DOF = \frac{2N - \frac{m}{2}}{m}, \quad (5.1)$$

where N denotes the number of occurrences and m denotes the number of bins (Panofsky and Brier 1968). For Manus, the total number of occurrences was 293 and the number of bins was 12, yielding approximately 50 degrees of freedom. Using a chi-square distribution table, the 0.1% limit of chi-square ($\chi_{.999}^2$) was found to be 86.7. Thus, $\frac{\chi_{.999}^2}{DOF}$ is 1.73 which implies there is a 99.9% probability that the observed value will be within 73% of the

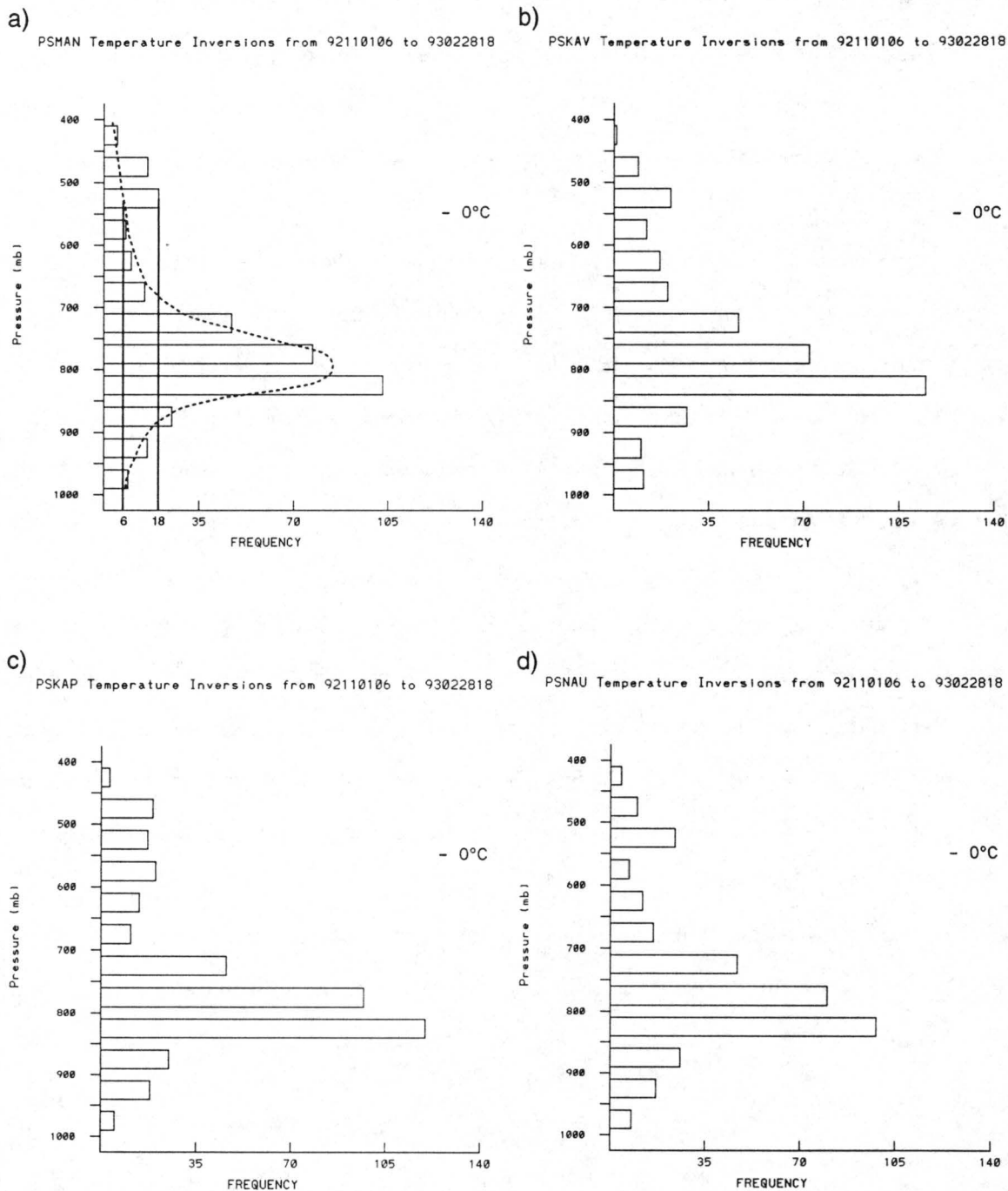


Figure 5.3: Stable layer locations during IOP at (a) Manus, (b) Kavieng, (c) Kapingamarangi, and (d) Nauru. Critical depth is 25 mb. The dashed line represents the null hypothesis for Manus (a). Expected and observed values for the 501-550 mb range at Manus are 6 and 18, respectively.

expected value or null hypothesis. The null hypothesis value for Manus in the 501 to 550 mb range was graphically computed (Fig. 5.3a) to be 6, assuming a null hypothesis which “tailed-off”. Therefore, the observed value of 18 at Manus is significant at the 99.9% level. Similar verifications were completed for the other sites.

Distributions of stable layers as a function of inversion depth are shown for Nauru in Fig. 5.4. Figure 5.4 shows that varying the depth requirement (shown to the right of

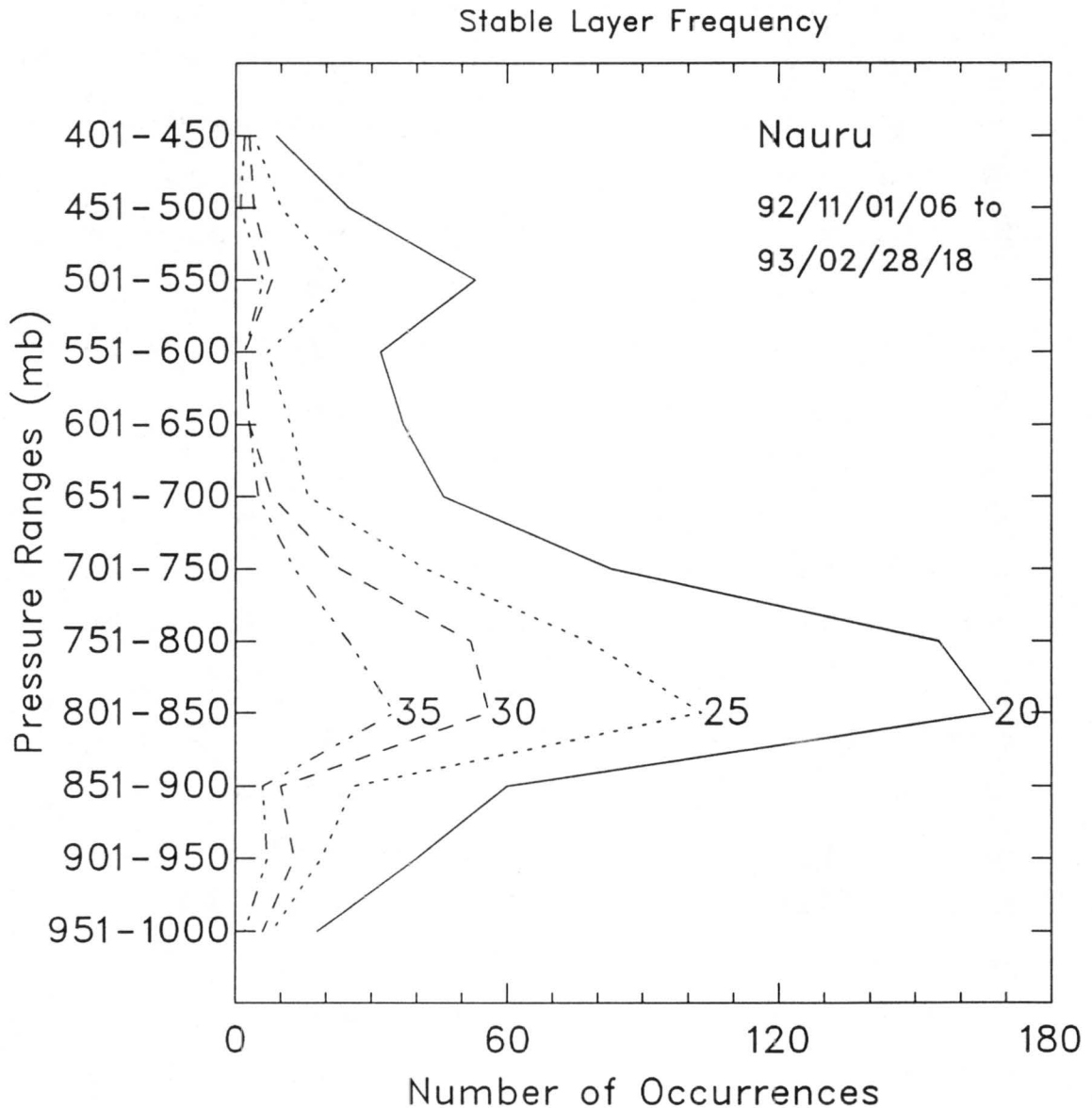


Figure 5.4: Stable layer locations ($\leq 4^{\circ}\text{K km}^{-1}$) at Nauru as a function of layer depth. Depth criteria (mb) are shown to the right of each curve.

each curve) did not change the prevalent double-peak structure. A maximum number of occurrences were observed in the 801-850 mb range. A secondary maximum occurred in the 501-550 mb range which corresponds to pressure levels just above the melting level. The fact that these stable layers occurred just above the melting level rather than below rules out the direct effects of melting (on soundings ascending through rain areas) as an explanation for this maximum. Reduction of the stable layer depth from 25 to 20 mb increases the frequency of inversions just above the melting level from about 5 to 12 %.

Stable layer distributions as a function of critical lapse rate are shown for Nauru in Fig. 5.5. The more stable (e.g. 2 to $3^{\circ}\text{K km}^{-1}$) lapse rate requirements (shown to the right of each curve) did not yield the pronounced double-peak structure found when the less stable lapse rates were used (e.g. $4^{\circ}\text{K km}^{-1}$). The more stable (stringent) lapse rate requirements produced a much more uniform distribution of stable layer locations. Similar distributions of stable layers as a function of depth and lapse rate were found at other sites.

Frequency distributions of specific humidity inversions are shown in Figs. 5.6a-d. A depth of 25 mb was subjectively chosen as the critical q inversion or reversal depth. Each of the sounding locations shows a single-peak structure versus the double peak structure shown on the temperature distributions. The low-level maximum associated with the shallow cumulus layer was not evident due to the steeper mean lapse rate of specific humidity in the lower troposphere and the fact that the low-level q reversal often was not sufficiently deep to meet the 25 mb criteria. The peaks at all stations were observed in a range between 551 and 700 mb, or at pressures just below the melting level. The local maxima frequently observed in the lowest levels (951-1000 mb) may be a diurnal feature associated with nocturnal cooling.

Figure 5.7 shows four distributions of q inversions observed at Nauru. The distributions were computed for varying critical inversion depths (shown to the right of each curve). As would be expected, more inversions met the shallower criteria. The same single peak structure occurs with a maximum number of occurrences in the 551-600 mb range for each depth criteria. For a 20 mb depth, nearly 25% of the soundings reported

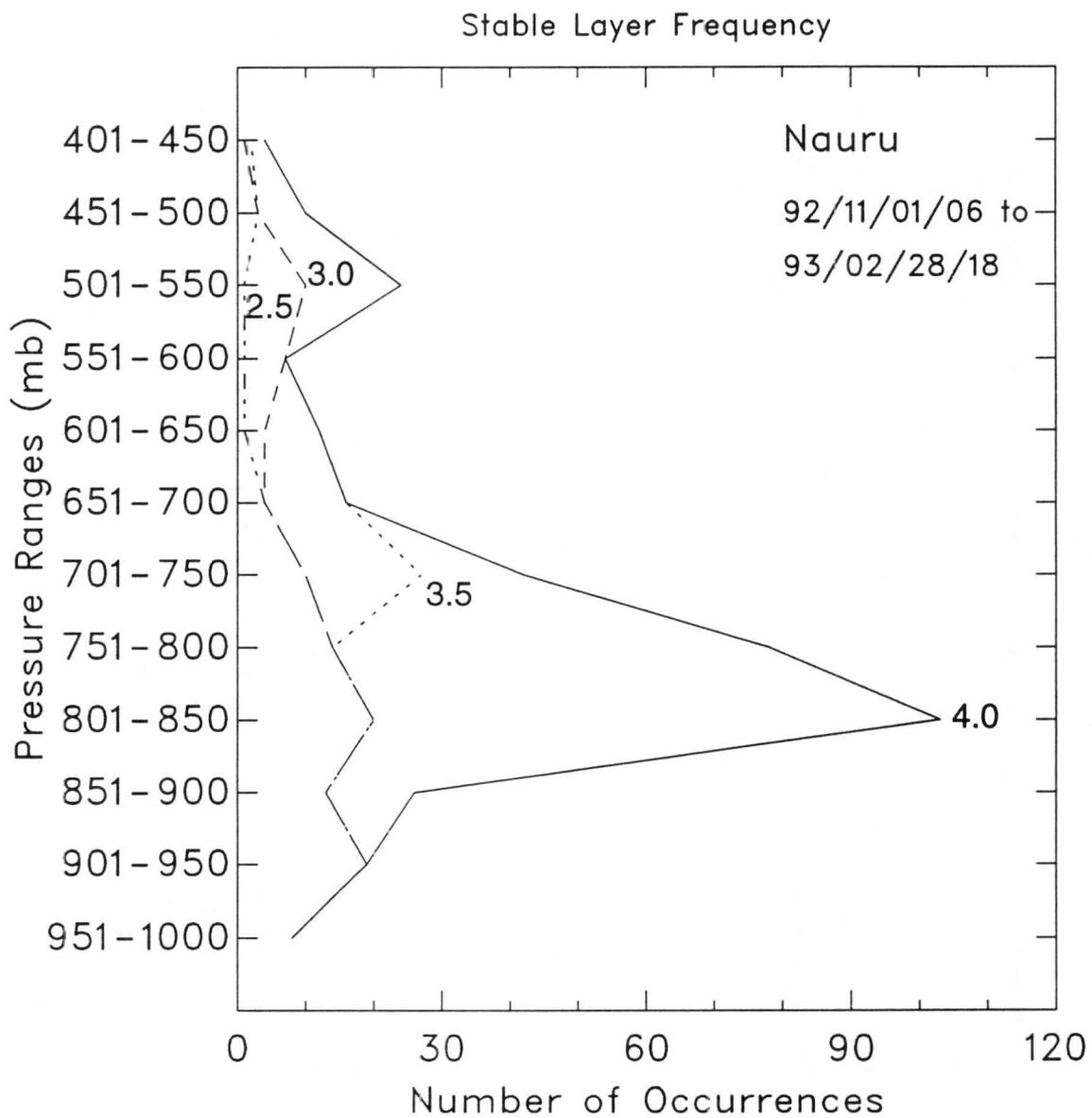


Figure 5.5: Stable layer locations at Nauru as a function of lapse rate. Lapse rate criteria ($^{\circ}\text{K km}^{-1}$) are shown to the right of each curve. Critical layer depth is held constant at 25 mb.

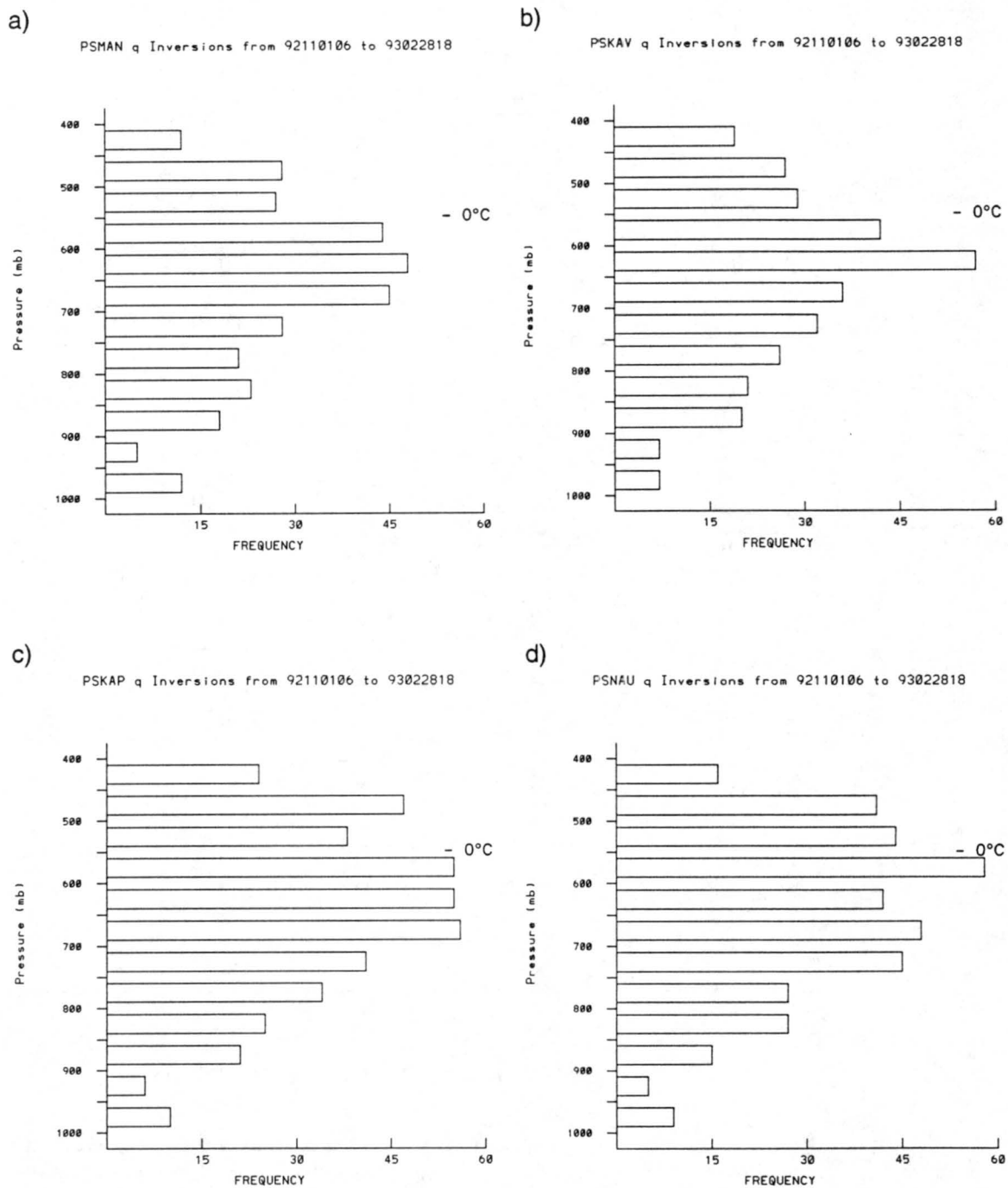


Figure 5.6: Specific humidity inversion locations during IOP at (a) Manus, (b) Kavieng, (c) Kapingamarangi, and (d) Nauru. Critical depth is 25 mb.

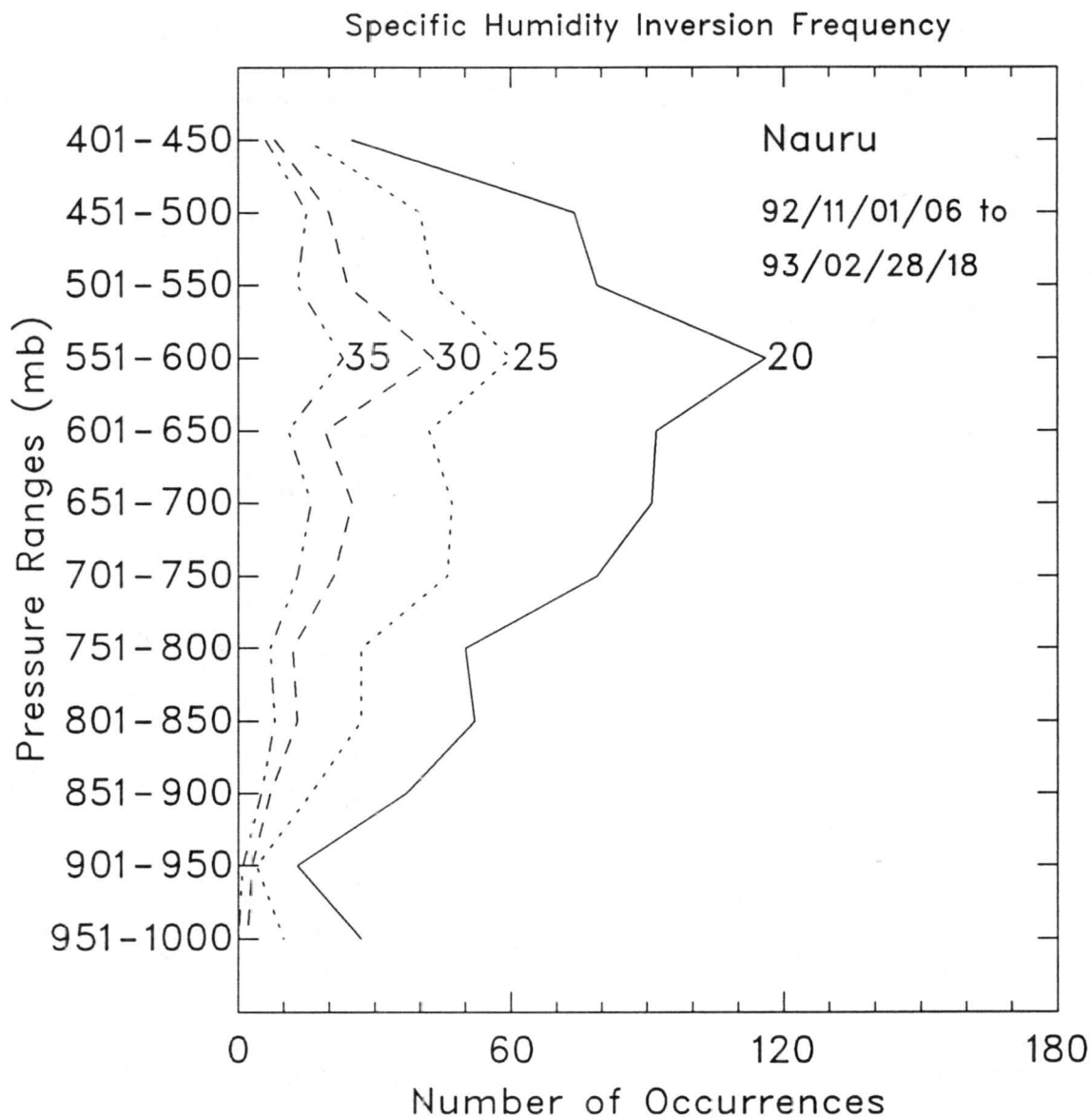


Figure 5.7: Specific humidity inversion locations at Nauru as a function of inversion depth. Depth criteria (mb) are shown to the right of each curve.

inversions between 551 and 600 mb. Similar distributions of specific humidity inversions as a function of inversion depth resulted at Kapingamarangi, Kavieng, and Manus.

5.3 Microphysical Processes

Conserved variable diagrams, similar to those introduced by Paluch (1979) to study vertical mixing in clouds, help to illustrate microphysical processes acting on air parcels. A schematic (Fig. 5.8) modified from the CBL study of Betts and Albrecht (1987) defines

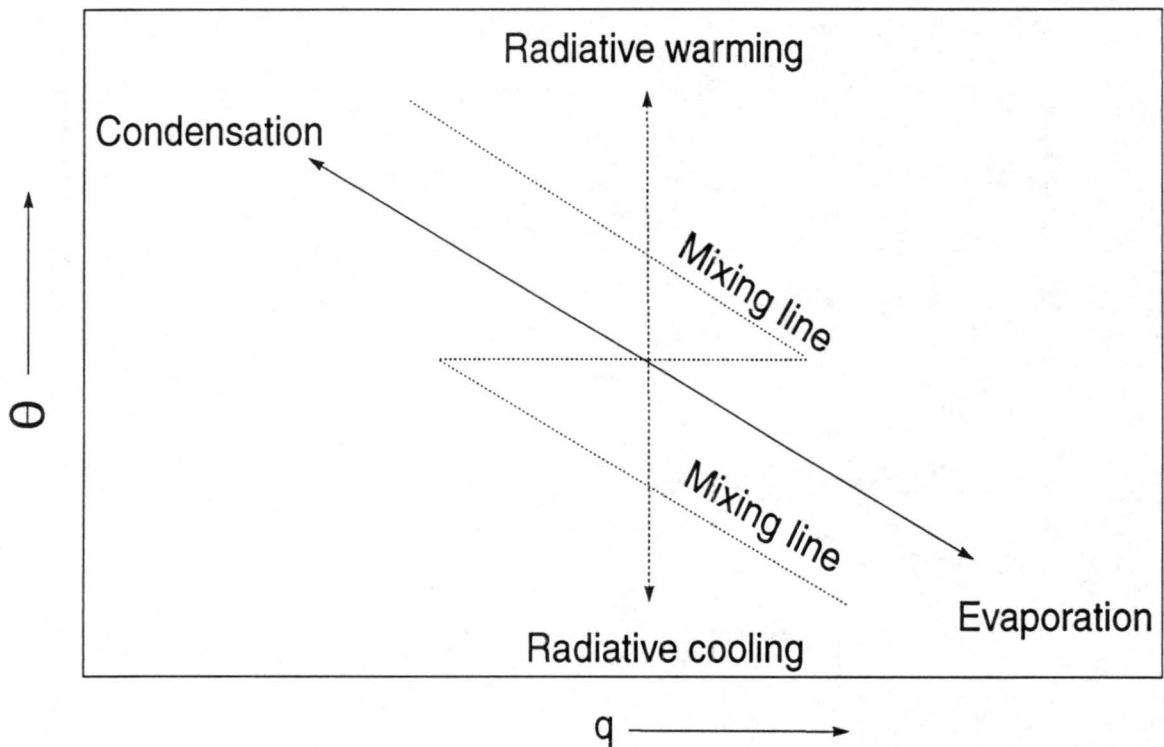


Figure 5.8: Schematic showing modification of a mixing line by microphysical processes (modified from Betts and Albrecht 1987).

the processes. The abscissa and ordinate, θ and q , are approximately equivalent to the conservative thermodynamic variables θ_l (liquid-water potential temperature) and q_T (total water mixing ratio) [Boers and Betts 1988]. The precipitation process moves parcels along lines of constant θ_e to lower q and higher θ . The evaporation of falling precipitation acts to reverse this by moving parcels to higher q and lower θ while conserving θ_e . The radiation process conserves q . Radiative cooling moves points to lower θ while radiative

warming conserves q by moving points to higher θ . Mixing processes occur along straight lines in the diagram.

Figure 5.9 shows a single sounding from Nauru, between 1000 and 400 mb, plotted

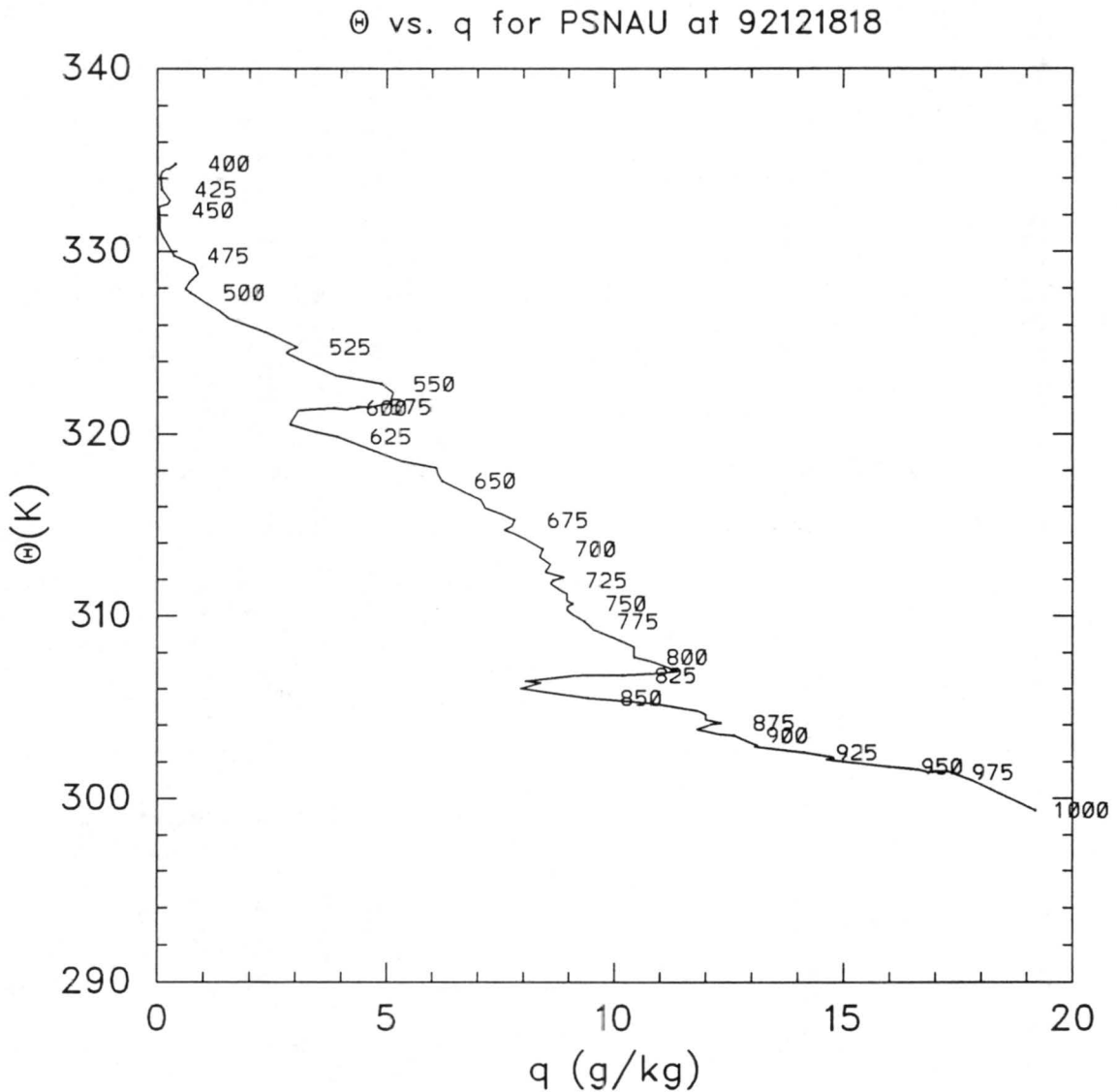


Figure 5.9: θ vs. q for Nauru at 1800 UTC 18 December.

in a θ vs. q format. Pressure levels are labeled every 25 mb along the curve, although the data are plotted every 5 mb. The lower inflection (near 800 mb) may be related to a shallow or trade cumulus layer. The other inflection occurred in the midtroposphere near the melting level. The linear orientation of points between the surface and 850 mb and between 800 and 625 mb corresponds, respectively, to mixing lines in the tradewind

cumulus layer and the layer above, which will be referred to here as the cumulus congestus layer. Betts and Albrecht (1987) argue that the q inversion associated with the tradewind cumulus layer can be explained by two populations of cumulus clouds, one shallow and one rising to higher levels, condensing and evaporating, leading to a double mixing line structure. It is conceivable that the q inversion near the melting level could have a similar explanation, if sufficient cumulus congestus exist; however, the populations of such clouds are not nearly as great as tradewind cumulus. Explanations for the q inversions will be explored in more detail in the next chapter.

One month of sounding data between 1000 and 300 mb every 20 mb at Kavieng, plotted in a similar θ vs. q format is shown in Fig. 5.10. The diagonal lines represent constant equivalent potential temperature. A well mixed boundary layer is reflected as a high density of points with low θ and high q in the lower right. Radiation in the upper troposphere is illustrated by the high density of points with high θ and nearly constant q (upper left). The roles of convective mixing, precipitation, and evaporation are depicted by the points intermediate to these two extremes. The prevalence of inversions near the melting layer can be seen from the scatter plot in Fig. 5.10. There are two areas of large variability - one corresponding to q and θ values near 7 g kg^{-1} and 310°K and the other near 2.5 g kg^{-1} and 320°K . These values correspond to the tradewind cumulus and near-melting layer inversions, respectively.

Microphysical processes in the tropics can be used to illustrate the role of the Hadley Cell circulation (Fig. 5.11) [R. Boers, personal communication]. Radiative cooling in the subsiding branch acts to lower θ at constant q . The air with the lowest θ sinks into the CBL and is mixed down the mixing line with air from below (Betts and Albrecht 1987). Surface fluxes act on the parcel in the boundary layer, increasing θ and q . Lateral transport processes act to move parcels to lower latitudes, increasing θ and q . Convection in the ascending branch acts to lower q while conserving θ_e .

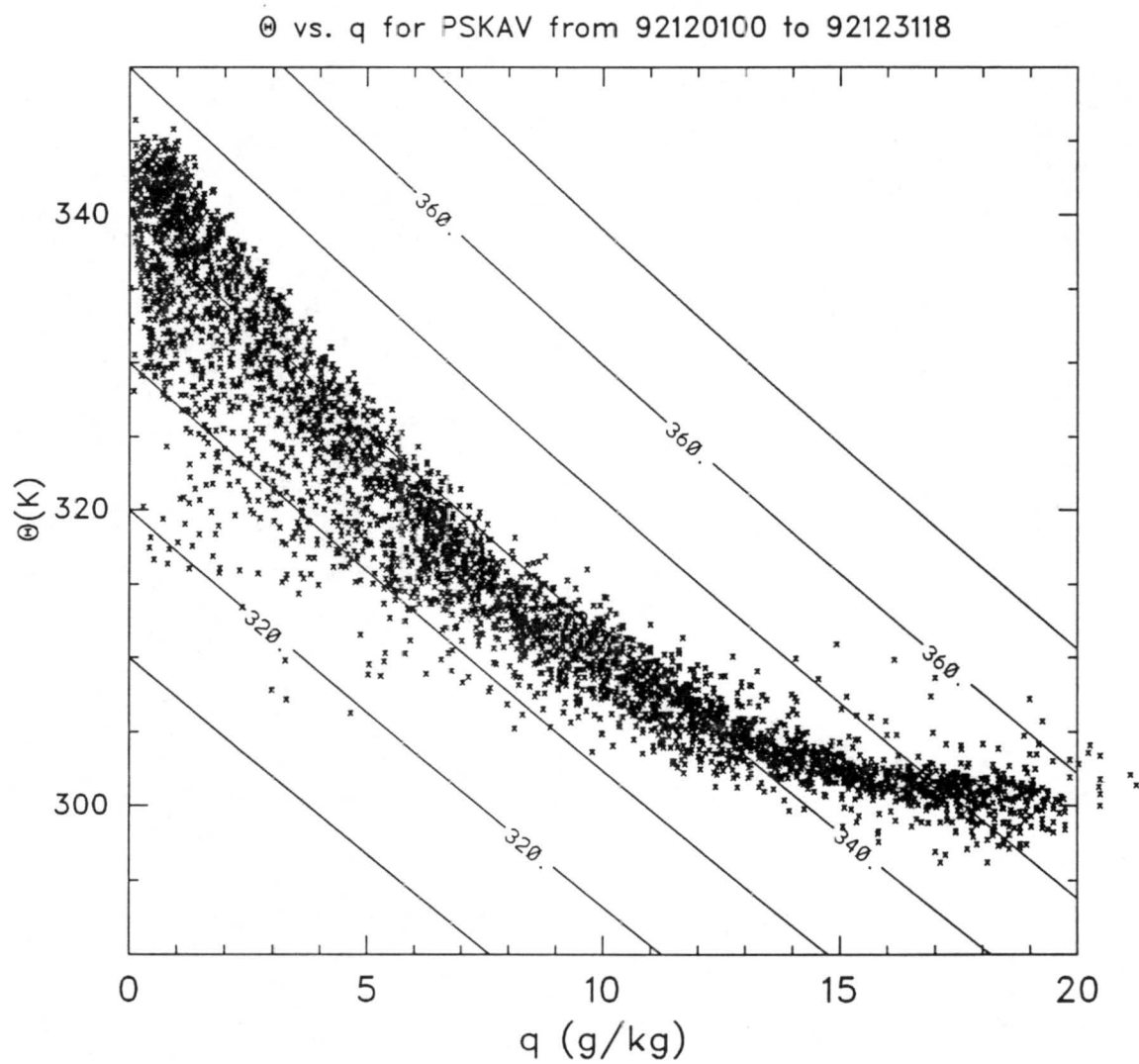


Figure 5.10: θ vs. q at Kavieng for month of December. Sloped lines are equivalent potential temperature.

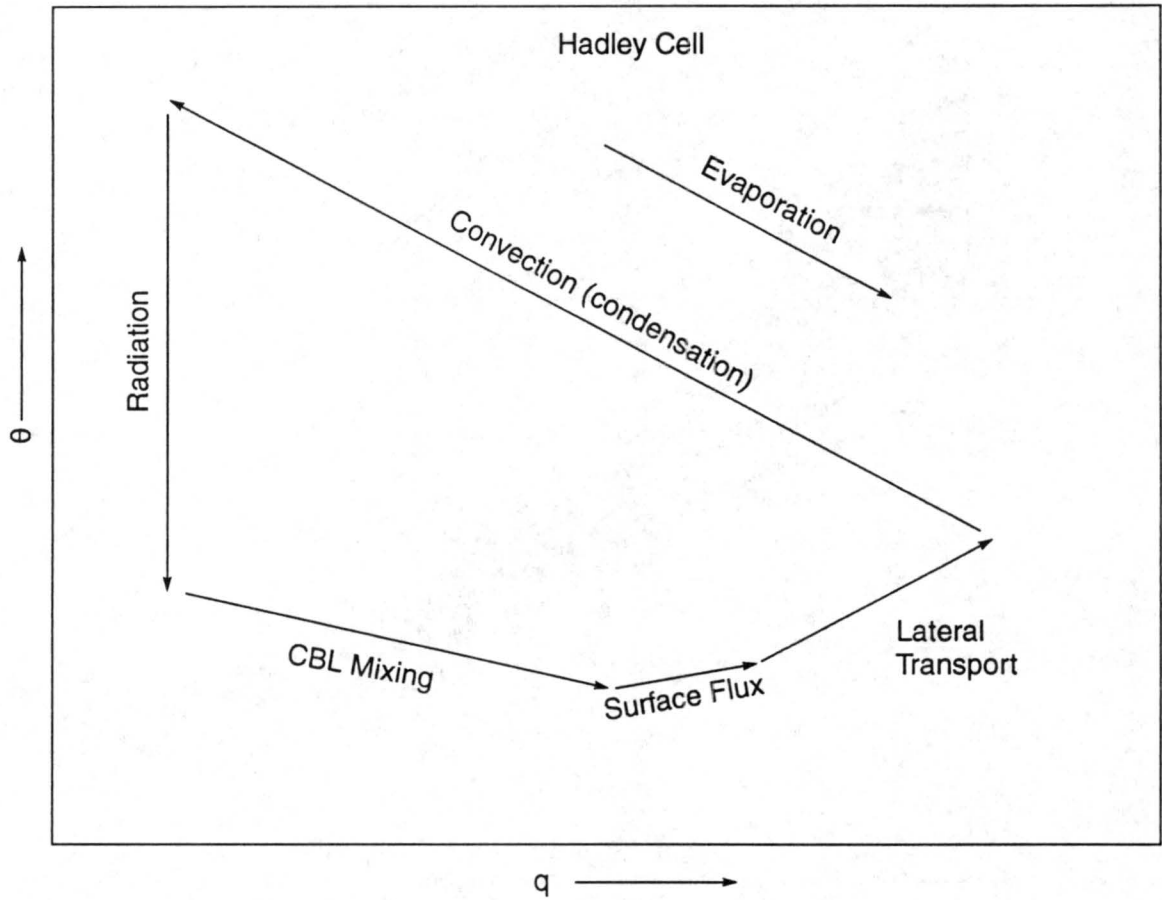


Figure 5.11: Illustration of the Hadley Cell using microphysical processes (R. Boers, personal communication).

Chapter 6

POSSIBLE CAUSES OF MOISTURE AND TEMPERATURE INVERSIONS NEAR THE 0°C LEVEL

Explanations of the possible causes of the stable layers and moisture inversions near the 0°C level leave many unanswered questions. The possible causes presented in this chapter are still a matter of speculation and remain under investigation. The simultaneous nature of the stable layer and moisture inversions over large horizontal domains and away from deep convection provides the setting for several possible explanations.

6.1 Temperature Inversions

The temperature inversions may be a remote response of potential vorticity (PV) anomalies generated by melting in stratiform cloud regions (Fig. 6.1). Heating in the stratiform region (condensation/deposition aloft and melting/evaporation below) produces a strong vertical gradient in the diabatic heating rate (i.e. $\dot{\theta}$). Mass is removed from the isentropic layer above the melting level and added to the isentropic layer below, creating a local, positive PV anomaly (e.g., Raymond and Jiang 1990; Hertenstein and Schubert 1991). Prof. W. Schubert of CSU is currently using a thermally forced, zonally symmetric, inviscid model to test this hypothesis. The model diagnoses PV given by

$$P = -\zeta_a \left(\frac{\partial \theta}{\partial p} \right), \quad (6.1)$$

where

$$\zeta_a = \zeta_r + f.$$

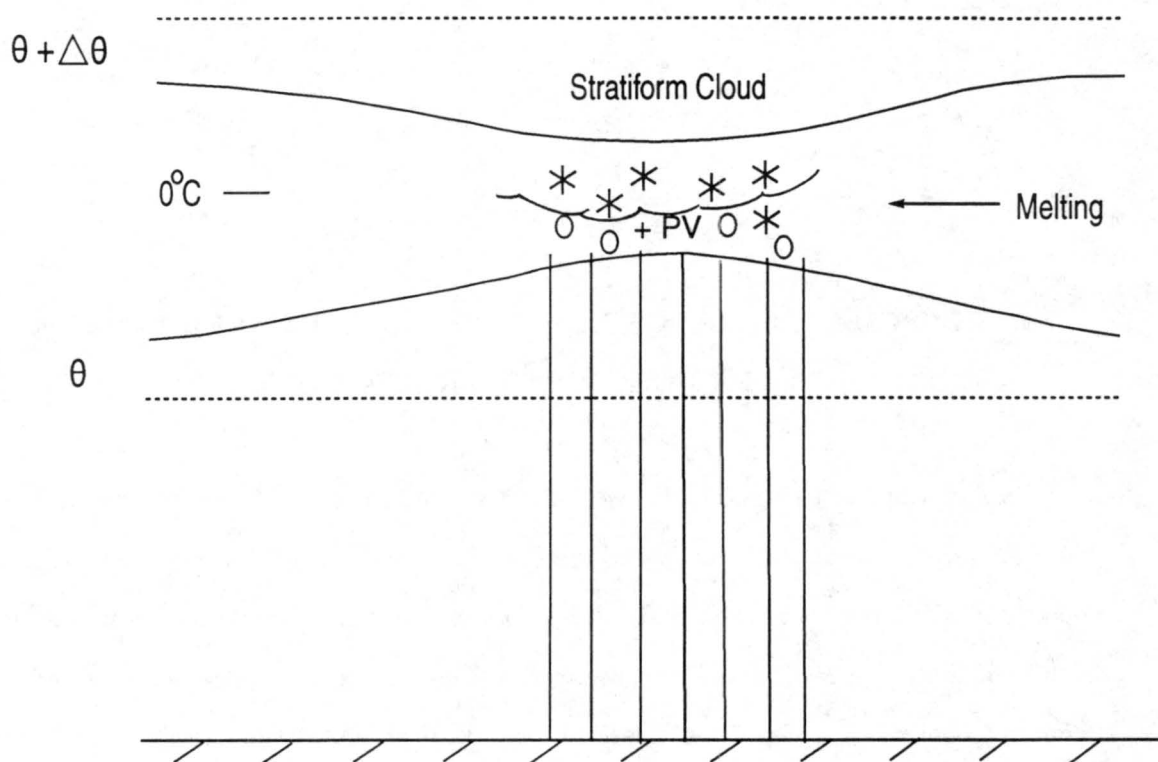


Figure 6.1: PV-induced anomaly mechanism for temperature inversions.

By exploiting the invertibility principle, the associated balanced wind and mass fields can be derived. Inversion of the PV anomaly reveals a horizontal spreading effect. Model results suggest that melting in stratiform rain areas produces temperature inversions in regions both local and remote to the precipitating region (P. Ciesielski, personal communication).

Another possibility is that thermally forced gravity waves could increase mid-tropospheric stability. Nicholls et al. (1991) developed a two-dimensional, incompressible, hydrostatic model to study transient gravity waves induced by MCS heating. The gravity wave response to stratiform-type thermal forcing propagates away from the prescribed heat source with a speed that is predicted by gravity wave theory. Nicholls et al. (1991) found two modes to be of primary importance, the external mode ($n=1$) and the first internal mode ($n=2$). The deep, fast $n=1$ mode acted to produce subsidence warming at large distances from the heat source. The $n=2$ mode moves away from the source at half the speed of the $n=1$ mode and is characterized by sinking aloft and rising motion at low-levels. A midlevel inflow develops in response to the heating. The sudden acceleration

of the winds and rapid onset of drying in the midtroposphere during case I may represent an example of the midlevel inflow response to heating. This gravity wave process may have drawn in drier air from higher latitudes as discussed in chapter 4.

Mapes (1993) shows that a heat source characteristic of a tropical MCS can cause additional convection nearby. Internal gravity waves generated by the tropical cloud clusters, referred to as "buoyancy bores" by Mapes (1993), produce upward displacements at low-levels and sinking aloft in areas outside of the convection. Positive feedbacks in convective development may result from the MCSs over warm ocean water leading to self-organizing convection (Mapes and Houze 1993). Figure 6.2, a schematic taken from Mapes (1993), illustrates the displacement of material surfaces as a result of gravity wave pulses. Mapes makes the important point that there are net vertical displacements associated with the waves - leading to increased stability in the midtroposphere.

Figure 6.3 shows a time series of specific humidity deviations from the IOP mean at Kapingamarangi from 15 December to 26 December. The negative deviations (drier than the mean) are shaded. The values shown are smoothed over a five sounding period. Early on the 17th (Day 2) a strong negative anomaly is noted above the 600 mb level while a strong positive anomaly is noted below 600 mb. These features may correspond to rising motion in the low-levels and sinking aloft associated with the gravity wave response outlined by Nicholls et al. (1991) and Mapes (1993).

A time series of temperature deviations from the IOP mean at Kapingamarangi from 15 December to 26 December is shown in Fig. 6.4. An area of strong positive temperature anomalies, beginning early on the 17th (Day 2), are centered at 500 mb. Negative temperature anomalies are found in the lower troposphere for the same time. This signature supports the gravity wave theory of low-level ascent and sinking aloft. Similar results for specific humidity and temperature deviations were found at other stations during Case I.

Finally, it is possible that the temperature inversions are a reflection of melting in stratiform clouds (e.g. Findeisen 1940). Stable layers may remain long after the stratiform cloud has dissipated. Figure 6.5 depicts how this may occur.

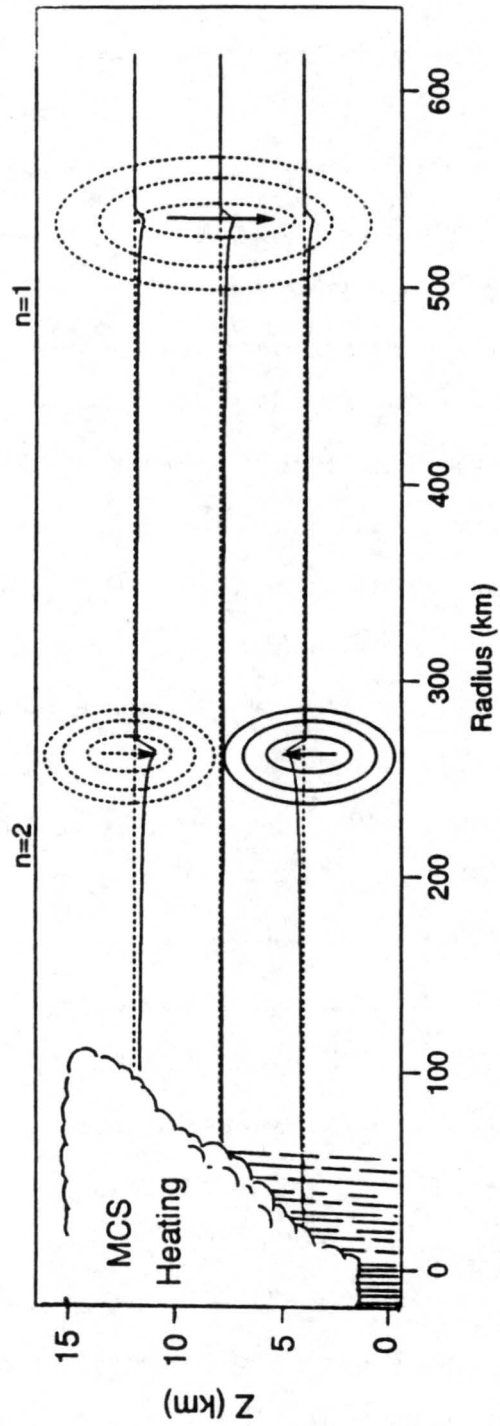


Figure 6.2: Buoyancy bore mechanism for temperature inversions (taken from Mapes 1993). Contours of w adapted from Nicholls et al. (1991).

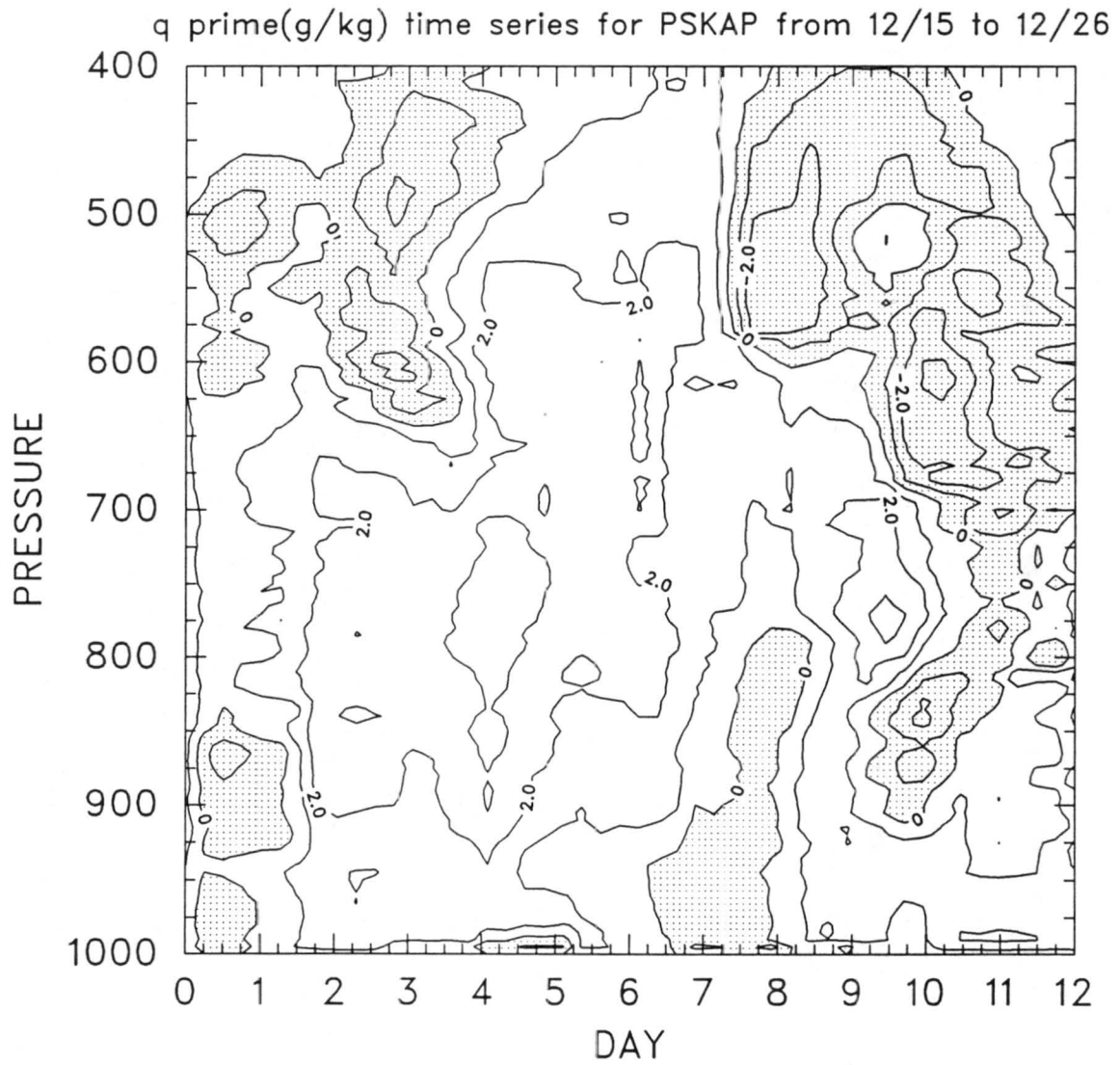


Figure 6.3: Specific humidity deviations from the IOP mean at Kapingamarangi from 15 December to 26 December. Contours are every $.5 \text{ g kg}^{-1}$.

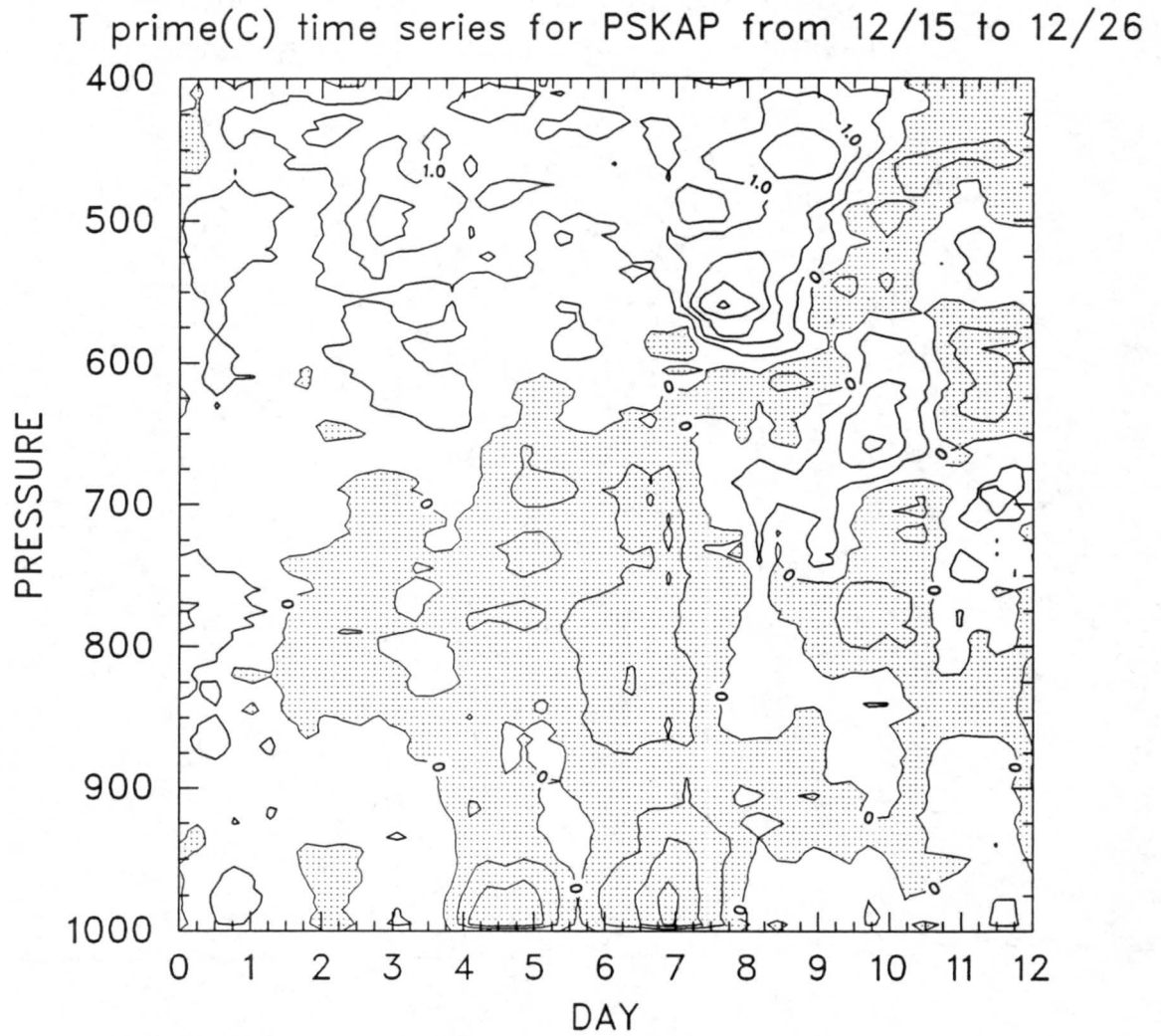


Figure 6.4: Temperature deviations from the IOP mean at Kapingamarangi from 15 December to 26 December. Contours are every $.5^{\circ}\text{C}$.

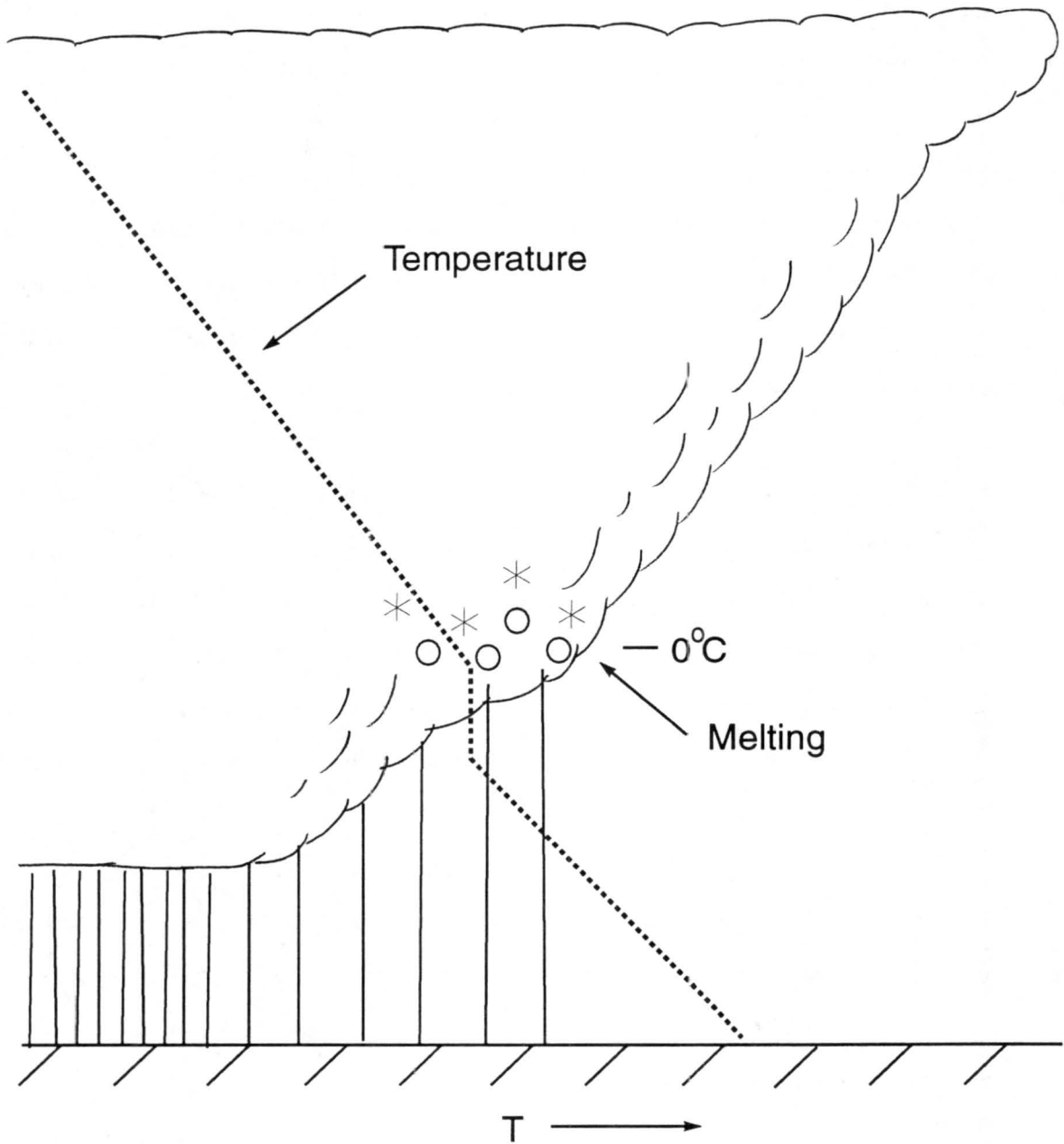


Figure 6.5: Temperature inversion formed by melting in stratiform region.

6.2 Moisture Inversions

The preceding causes may explain the temperature inversion, but they do not explain the moisture inversion. A first possible explanation relates to processes associated with stratiform clouds within MCSs. Zipser (1977) has shown that within such cloud systems, the air is nearly saturated above the 0°C level and dry below. Soundings taken in this region exhibit an “onion-like” structure (Zipser 1977). Ascents through many stratiform rain areas of this nature could conceivably “perturb” the mean relative humidity profile in such a way as to yield a local maximum near 0°C . However, the frequency of such ascents was small and, moreover, many humidity inversions were found in clear air far removed from convection. Therefore, other explanations must be sought.

Two other mechanisms are suggested by the data. First, Bretherton and Smolarkiewicz (1989) performed a 2-D numerical simulation and showed that gravity waves acted to preferentially detrain moisture from deep convective clouds near stable layers. They considered a cumulus cloud, initiated by a surface heat flux perturbation, that penetrated a stable layer about 2.5 km above cloud base. Bretherton and Smolarkiewicz (1989) found that detrainment is concentrated in levels where the cloud buoyancy relative to the far environment was decreasing with height which implies a stable layer in the environment.

Figure 6.6, taken from Bretherton and Smolarkiewicz (1989), shows the evolution of the numerically simulated cumulus cloud. The total mixing ratio Q , where Q is the sum of water vapor and cloud mixing ratios, is plotted at times $t = 20, 32, 40, 52, 64,$ and 96 minutes. Two distinct outflow areas developed - one between 4 and 5 km and the other near the tropopause at 8.5 km.

Secondly, heavily raining congestus clouds were observed to preferentially top out near the freezing level during COARE (Fig. 6.7). Moisture may have detrained near the 0°C level, leaving higher humidities. Ship-based radar data show that these heavily raining congestus clouds may account for up to $1/6$ of the total rainfall measured during COARE periods (T. Rickenbach, personal communication). Williams et al. (1994) classified rain associated with four types of cloud structures for nearly a one year period at Manus Island.

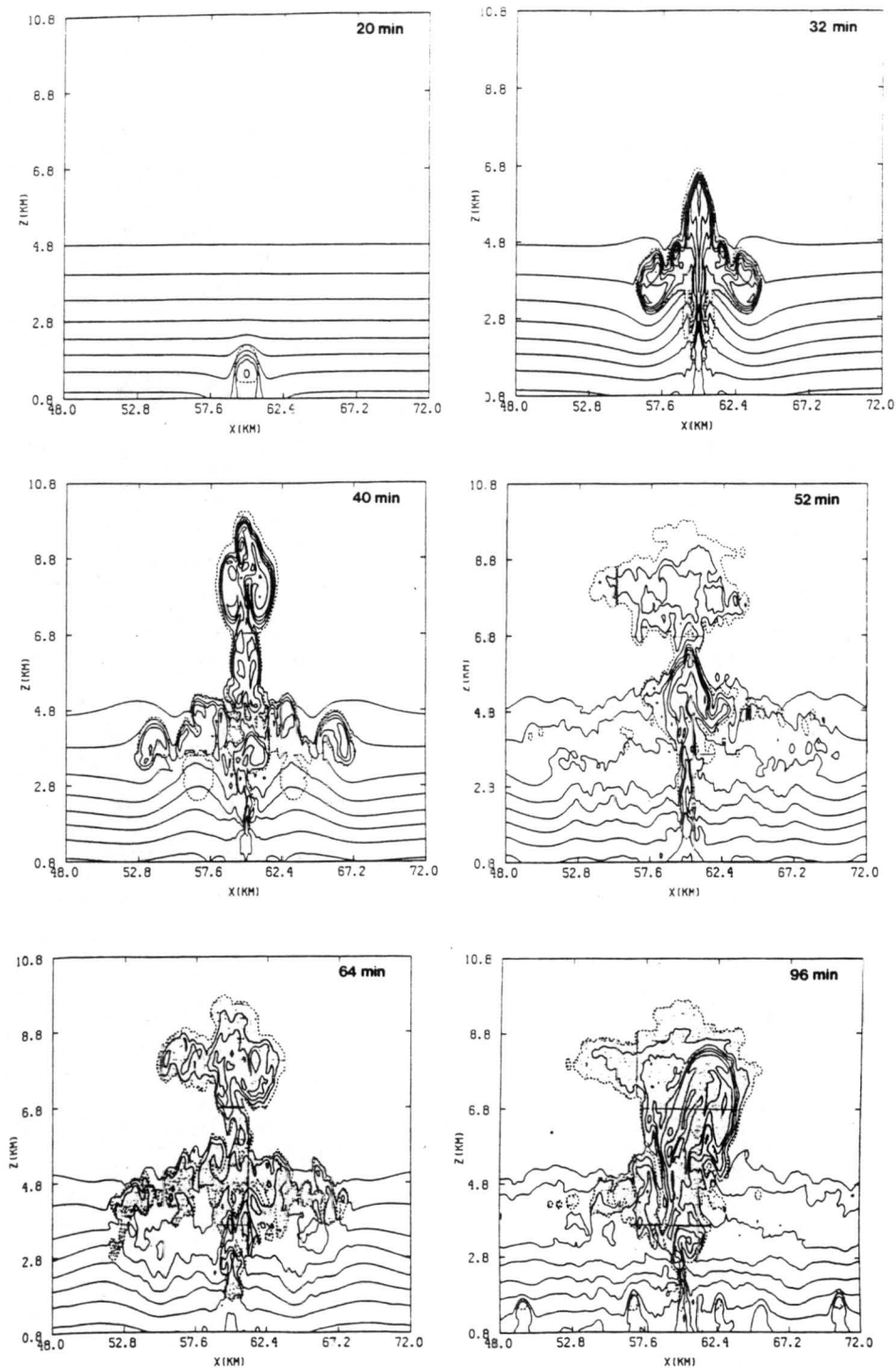


Figure 6.6: Numerical simulation of a cumulus cloud detrainment near a stable layer (taken from Bretherton and Smolarkiewicz 1989). Total mixing ratio Q contoured at intervals of 1 g kg^{-1} . Cloudy air is shaded.

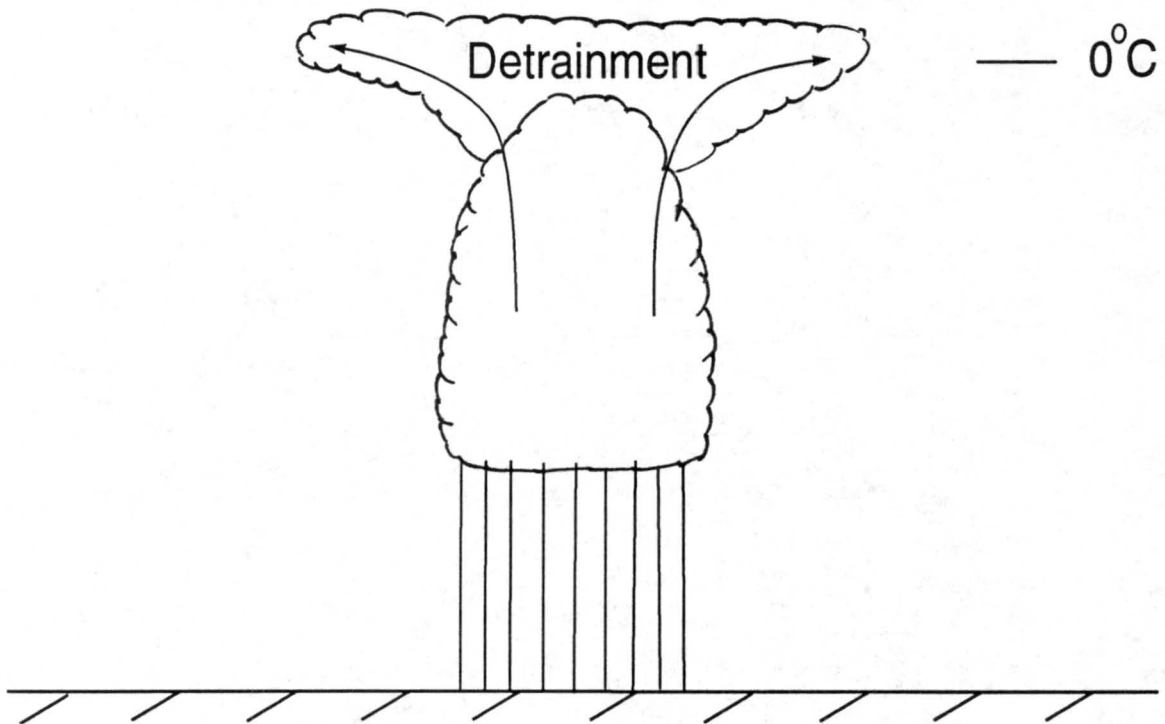


Figure 6.7: Heavily raining congestus cloud detrainment near the freezing level.

They found that 8.6% of the total precipitation was the result of “low-level” or “warm” rain clouds where hydrometeors are confined to regions below the melting layer.

Chapter 7

SUMMARY AND CONCLUSIONS

This study has documented a recurring q reversal or inflection point in a shallow layer near the melting level during the TOGA COARE IOP. The q reversals were often associated with temperature inversions (or stable layers) positioned slightly above the moist layer. The persistent stable layers are consistent with those observed by Haraguchi (1968). Although these features were observed at other times during the four-month IOP, three extended periods of the phenomena have been illustrated. The features were often observed simultaneously across large horizontal domains which may suggest a possible link to synoptic-scale controls. The inflection in q is likely responsible for the commonly observed double-peak structure in the apparent moisture sink Q_2 over tropical regions.

IR satellite images during these periods indicated that the moisture and temperature inflections occurred in regions that were generally undisturbed and away from any deep convection. Convection during these periods was typically organized into two latitudinally oriented bands, which formed a "double-ITCZ". Deep convection was suppressed near the equator where the analyzed soundings were launched.

The first case occurred prior to the onset of the active phase of the Madden Julian Oscillation (MJO) and was characterized by strong, northeast to easterly flow in the midtroposphere. During Case I, a dry regime in the midtroposphere deepened with time to include layers above and below the freezing level. The dry regime was interrupted by a shallow, moist layer which was capped by stable conditions at the melting level.

Case II evolved in a similar fashion as dry conditions deepened with time to eventually include layers above and below the melting level. Dry conditions were interrupted by a moist layer present at the 0°C level. As in Case I, stable conditions existed immediately

above the moist layer. Case II differed from Case I as it occurred during the active phase of the MJO with deep westerly flow through 400 mb.

Case III occurred during the active phase of the third MJO which crossed the sounding arrays during the IOP. In Case III, however, westerlies were only observed from the surface to between 600 and 550 mb to remain generally below the 0°C level. Easterly flow above the freezing level was characterized by higher relative humidities, likely the result of outflow from convection observed to the east of the OSA early in the period.

Average relative humidity profiles computed for the four-month IOP revealed a nearly constant layer of relative humidity between 750 and 500 mb at each of the sites examined for this study. The average relative humidity profiles at each of the stations, except for Manus, exhibited a slight reversal in relative humidity through the midtroposphere. This reversal was marked by maxima near the 0°C level. In addition, the highest average relative humidity values at each station were observed near the 950 mb level. These findings are consistent with the recent results of Liu et al. (1991) and Gutzler (1993) for tropical ocean stations. The average humidity profiles do not support the linear relation between relative humidity and pressure prescribed by Manabe and Wetherald (1967).

Average $d\theta/dp$ profiles computed for the IOP at each of the four stations showed a steep increase in stability in the midtroposphere. The layer at and above the freezing level was considerably more stable than the layer immediately below. Values of $d\theta/dp$ should typically decrease towards the tropopause, but between the 0°C level and 400 mb there was little overall change in $d\theta/dp$ observed. The resulting inflection in slope at the freezing level points to locally enhanced stability there.

Frequency distributions of temperature inversions (or stable layers) reflected a double-peak structure in the number of occurrences. The maximum number of occurrences occurred between 850 and 801 mb, likely in association with shallow cumulus clouds or a tradewind like regime. A secondary maximum was observed in the midtroposphere, usually between 550 and 501 mb. This maximum was just above the melting level, suggesting that it was not a direct manifestation of melting effects on soundings ascending through rain areas. Frequency distributions of specific humidity inversions were found to exhibit

a single-peak structure with the maximum number of occurrences in a range between 650 and 601 mb, just below the melting level.

The mechanisms by which the temperature and moisture inversions form are still unclear. Temperature inversions may be the result of melting-induced, positive potential vorticity (PV) anomalies. Diabatic cooling associated with the melting produces a downward mass flux resulting in a local, positive PV anomaly. Inverting the positive PV anomaly to obtain the associated balanced wind and mass fields reveals a horizontal spreading effect. The spreading effect allows temperature inversions to exist in regions horizontally removed from the melting. Further study of this theory is continuing under the direction of Professor W. Schubert of CSU. A second possibility involves the internal modes of gravity waves induced by tropical MCS heating. The gravity waves propagate away from the heat source, producing sinking aloft and rising motion at low levels in areas removed from the convection. The result can increase mid-tropospheric stability. Lastly, the temperature inversions may be the remnants of melting in stratiform clouds that have since dissipated.

The preceding explanations do not account for the water vapor inversions found in this study. One explanation may be related to the preferential detrainment of moisture from cumulus clouds near stable layers as modeled by Bretherton and Smolarkiewicz (1989). The second possibility involves the existence of heavily-raining congestus. Ship-based radars in COARE frequently observed heavily-raining congestus clouds preferentially topping out near the 0°C level. Detrainment associated with the congestus clouds may be leaving higher concentrations of water vapor there.

This study has documented reversals in humidity and recurring stable layers near the melting level over the Pacific "warm-pool" region. The phenomena are common enough to warrant further examination. The thermodynamic and kinematic structure of soundings associated with the inflections showed some variation. Future work should first concentrate on categorizing the types of structures found to produce moisture and temperature inversions near the freezing level. In addition, numerical simulation would likely provide further insight into the exact mechanism leading to their existence. The distributions

of moisture and temperature presented in this study may provide further information about what controls cloud populations over the tropical regions. Correlating the locations of temperature and moisture inflections with observed cloud tops using either radar or high-resolution satellite data would be useful.

REFERENCES

- Augstein, E., 1978: The atmospheric boundary layer over the tropical oceans. *Meteorology over the Tropical Oceans*. D.B. Shaw, Ed., Roy. Meteor. Soc., 73-104.
- Augstein, E., H. Riehl, F. Ostapoff and V. Wagner, 1973: Mass and energy transports in an undisturbed Atlantic trade wind flow. *Mon. Wea. Rev.*, **101**, 101-111.
- Barnes, S.L., 1973: Mesoscale objective map analysis using weighted time series observations. NOAA Tech. Memo. ERL NSSL-62, Norman, Oklahoma, 60 pp.
- Betts, A.K., 1982: Saturation point analysis of moist convective overturning. *J. Atmos. Sci.*, **39**, 1484-1505.
- Betts, A.K., and B.A. Albrecht, 1987: Conserved variable analysis of the convective boundary layer thermodynamic structure over the tropical oceans. *J. Atmos. Sci.*, **44**, 83-99.
- Boers, R., and A.K. Betts, 1988: Saturation point structure of marine stratocumulus clouds. *J. Atmos. Sci.*, **45**, 1156-1175.
- Bolton, D., 1980: The computation of equivalent potential temperature. *Mon. Wea. Rev.*, **108**, 1046-1053.
- Bretherton, C.S., and P.K. Smolarkiewicz, 1989: Gravity waves, compensating subsidence and detrainment around cumulus clouds. *J. Atmos. Sci.*, **46**, 740-759.
- Brock, F.V., G.H. Saum, and S.R. Semmer, 1986: Portable Automated Mesonet II. *J. Atmos. and Ocean. Tech.*, **3**, 573-582.

- Cole, H., 1993: The TOGA COARE ISS radiosonde temperature and humidity sensor errors. NCAR Technical Report, Boulder, CO, 26 pp.
- Findeisen, W., 1940: The formation of the 0°C isothermal layer and fractocumulus under nimbostratus. *Meteor. Z.*, **57**, 49-54.
- Firestone, J.K, and B.A. Albrecht, 1986: The structure of the atmospheric boundary layer in the central equatorial Pacific during January and February of FGGE. *Mon. Wea. Rev.*, **114**, 2219-2231.
- Gutzler, D.S., 1993: Uncertainties in climatological tropical humidity profiles: Some implications for estimating the greenhouse effect. *J. Climate*, **6**, 978-982.
- Gutzler, D.S., G.N. Kiladis, G.A. Meehl, K.M. Weickmann, and M. Wheeler, 1994: The global climate of December 1992-February 1993. Part II. Large-scale variability across the tropical western Pacific during TOGA COARE. *J. Climate*, **7**, submitted for publication.
- Haraguchi, P.Y., 1968: Inversions over the tropical eastern Pacific Ocean. *Mon. Wea. Rev.*, **96**, 177-185.
- Hertenstein, R.F.A., and W.H. Schubert, 1991: Potential vorticity anomalies associated with squall lines. *Mon. Wea. Rev.*, **119**, 1663-1672.
- Holland, J.Z., and E. Rasmusson, 1973: Measurements of the atmospheric mass energy and momentum budgets over a 500 kilometer square of tropical ocean. *Mon. Wea. Rev.*, **101**, 44-55.
- Johnson, R.H., 1976: The role of convective-scale precipitation downdrafts in cumulus and synoptic scale interactions. *J. Atmos. Sci.*, **33**, 1890-1910.

- Johnson, R.H., 1984: Partitioning tropical heat and moisture budgets into cumulus and mesoscale components: Implications for cumulus parameterization. *Mon. Wea. Rev.*, **112**, 1590-1601.
- Johnson, R.H., J.F. Bresch, P.E. Ciesielski, and W.A. Gallus, Jr., 1993: The TOGA COARE atmospheric sounding array: Its performance and preliminary scientific results. *Preprints, 20th Conference on Hurricanes and Tropical Meteorology*, San Antonio, Texas, Amer. Meteor. Soc., 343-348.
- Kloesel, K.A., 1993: Above-inversion profiles of moisture and ozone observed during FIRE. *Mon. Wea. Rev.*, **121**, 683-694.
- Kloesel, K.A., and B.A. Albrecht, 1989: Low-level inversions over the tropical Pacific – thermodynamic structure of the boundary layer and the above-inversion moisture structure. *Mon. Wea. Rev.*, **117**, 87-101.
- Lindzen, R.S., 1990: Some coolness concerning global warming. *Bull. Amer. Meteor. Soc.*, **71**, 288-299.
- Lindzen, R.S., A.Y. Hou, and B.F. Farrel, 1982: The role of convective model choice in calculating the climate impact of doubling CO_2 . *J. Atmos. Sci.*, **39**, 1189-1205.
- Liu, W.T., W. Tang, and P.P. Niiler, 1991: Humidity profiles over the ocean. *J. Climate*, **4**, 1023-1034.
- Madden, R.A., and P.R. Julian, 1972: Description of global-scale circulation cells in the tropics with a 40-50 day period. *J. Atmos. Sci.*, **29**, 1109-1123.
- Manabe, S., and R.T. Wetherald, 1967: Thermal equilibrium of the atmosphere with a given distribution of relative humidity, *J. Atmos. Sci.*, **24**, 241-259.
- Mapes, B.E., 1993: Gregarious tropical convection. *J. Atmos. Sci.*, **50**, 2026-2037.

- Mapes, B.E., and R.A. Houze, Jr., 1993: Cloud clusters and superclusters over the oceanic warm pool. *Mon. Wea. Rev.*, **121**, 1398-1415.
- Miller, E., 1993: TOGA COARE ISS data report - volume I surface and sounding data, NCAR Technical Report, Boulder, CO, 41 pp.
- Neiburger, M., D.S. Johnson, and C.W. Chein, 1961: Studies of the structure of the atmosphere over the eastern Pacific Ocean in summer, I. The inversion over the eastern north Pacific Ocean. *Univ. Calif. Publ. Meteor.*, **1**, 94 pp.
- Nicholls, M.E., R.A. Pielke, and W.R. Cotton, 1991: Thermally forced gravity waves in an atmosphere at rest. *J. Atmos. Sci.*, , 1869-1884.
- Oort, A.H., 1983: Global atmospheric circulation statistics, 1958-1973. NOAA Prof. Paper 14, Rockville, MD, NOAA, U.S. Department of Commerce, 180 pp.
- Paluch, I.R., 1979, The entrainment mechanism in Colorado cumuli, *J. Atmos. Sci.*, **36**, 2467-2478.
- Panofsky, H.A., and G.W. Brier, 1968: *Some Applications of Statistics to Meteorology*. Penn State University, 224 pp.
- Parsons, D., W. Dabberdt, H. Cole, T. Hock, C. Martin, A.L. Barrett, E. Miller, M. Spowart, M. Howard, W. Ecklund, D. Carter, K. Gage, and J. Wilson, 1994: The Integrated Sounding System: Description and preliminary observations from TOGA COARE. *Bull. Amer. Meteor. Soc.*, **75**, submitted for publication.
- Raymond, D.J., and H. Jiang, 1990: A theory for long-lived mesoscale convective systems. *J. Atmos. Sci.*, **47**, 3067-3077.
- Reed, R.J., and E.E. Recker, 1971: Structure and properties of synoptic-scale wave disturbances in the equatorial western Pacific. *J. Atmos. Sci.*, **28**, 1117-1133.

- Riehl, H., 1979: *Climate and Weather in the Tropics*. Academic Press, 611 pp.
- Riehl, H., T.C. Yeh, J.S. Malkus, and N.E. LaSeur, 1951: The northeast trade of the Pacific Ocean. *Quart. J. Roy. Meteor. Soc.*, **77**, 598-626.
- Thompson, R.M., Jr., S.W. Payne, E.E. Recker, and R.J. Reed, 1979: Structure and properties of synoptic-scale disturbances in the intertropical convergence zone of the eastern Atlantic. *J. Atmos. Sci.*, **36**, 53-72.
- TOGA COARE International Project Office, 1992: TOGA COARE Operations Plan, September 1992. TOGA COARE Int'l Project Office, UCAR, Boulder, CO.
- TOGA COARE International Project Office, 1993: TOGA COARE Intensive Observing Period Operations Summary, June 1993. TOGA COARE Int'l Project Office, UCAR, Boulder, CO.
- Webster, P.J., and R. Lukas, 1992: TOGA COARE: The Coupled Ocean Atmosphere Response Experiment. *Bull. Amer. Meteor. Soc.*, **73**, 1377-1417.
- Wexler, A., 1976: Vapor pressure formulation for water in range 0 to 100°C. A revision. *J. Res. Nat. Bur. Stand.*, **80A**, 775-785.
- Williams, C.R., K.S. Gage, and W.R. Ecklund, 1994: Applications of 915-MHz wind profilers to the classification of tropical precipitating cloud systems observed during TOGA COARE. *Preprints, 6th Conference on Climate Variations*, Nashville, Tennessee, Amer. Meteor. Soc., J68-J71.
- World Meteorological Organization, 1987: Manual on Codes, Volume II - Regional Codes and National Coding Practices. Geneva, Switzerland.
- Yanai, M., S. Esbensen, and J.H. Chu, 1973: Determination of bulk properties of tropical cloud clusters from large-scale heat and moisture budgets. *J. Atmos. Sci.*, **30**, 611-627.

Zipser, E.J., 1977: Mesoscale and convective-scale downdrafts as distinct components of squall-line structure. *Mon. Wea. Rev.*, **105**, 1568-1589.